Influence of Initial Thermomechanical Treatment on High Temperature Properties of Laves Phase Strengthened Ferritic Steels

Michal Talík

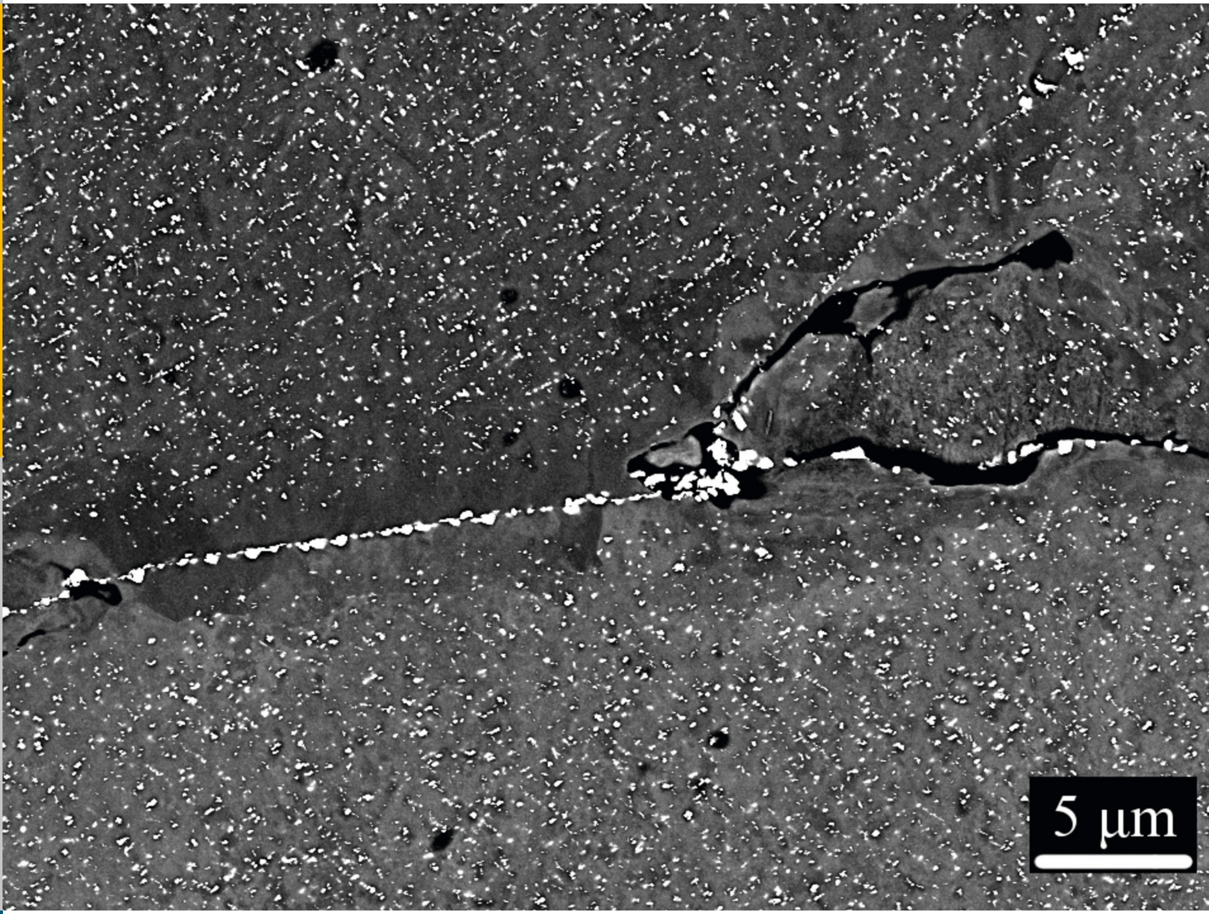

Energie & Umwelt /
Energy & Environment
Band / Volume 338
ISBN 978-3-95806-175-0

JÜLICH
FORSCHUNGSZENTRUM

Schriften des Forschungszentrums Jülich
Reihe Energie & Umwelt / Energy & Environment Band / Volume 338

Forschungszentrum Jülich GmbH
Institute of Energy and Climate Research (IEK)
Microstructure and Properties of Materials (IEK-2)

Influence of Initial Thermomechanical Treatment on High Temperature Properties of Laves Phase Strengthened Ferritic Steels

Michal Talík

Schriften des Forschungszentrums Jülich
Reihe Energie & Umwelt / Energy & Environment Band / Volume 338

ISSN 1866-1793 ISBN 978-3-95806-175-0

Bibliographic information published by the Deutsche Nationalbibliothek.
The Deutsche Nationalbibliothek lists this publication in the Deutsche
Nationalbibliografie; detailed bibliographic data are available in the
Internet at http://dnb.d-nb.de.

Publisher and Distributor: Forschungszentrum Jülich GmbH
Zentralbibliothek
52425 Jülich
Tel: +49 2461 61-5368
Fax: +49 2461 61-6103
Email: zb-publikation@fz-juelich.de
www.fz-juelich.de/zb

Cover Design: Grafische Medien, Forschungszentrum Jülich GmbH

Printer: Grafische Medien, Forschungszentrum Jülich GmbH

Schriften des Forschungszentrums Jülich
Reihe Energie & Umwelt / Energy & Environment, Band / Volume 338

D 82 (Diss. RWTH Aachen University, 2016)

ISSN 1866-1793
ISBN 978-3-95806-175-0

Contents

List of Figures

List of Tables

Abstract

The aim of this work was to design 17 wt%Cr Laves phase strengthened HiperFer (**Hi**gh **per**fomrance **Fer**rite) steels and evaluate their properties. This class of steel is supposed to be used in Advanced Ultra Super Critical power plants. Such cycles exhibit higher efficiency and are environmentally friendly, but improved materials with high resistance to fireside/steam oxidation and sufficient creep strength are required. The work focused on the characterization of creep properties of 17Cr2.5W0.5Nb0.25Si heat resistant steel. Small batches of steels with nominal compositions of 17Cr3W0.5Nb0.25Si and 17Cr3W0.9Nb0.25Si were used to analyze the influence of chemical composition on the precipitation behaviour in comparison to 17Cr2.5W0.5Nb0.25Si steel.
Creep strength of HiperFer steels is ensured by fine dispersion of thermodynamically stable Laves phase particles, while maintaining high corrosion resistance by a relatively high chromium content. Design of HiperFer steels was accomplished by thermodynamic modeling (Thermocalc) with the main tasks of elimination of the unwelcome brittle (Fe,Cr)-σ phase and maximization of the content of the strengthening C14 Fe_2Nb type Laves phase particles. Long term annealing experiments of all HiperFer steels were performed at 650 °C in order to evaluate the role of chemical composition and initial thermo-mechanical treatment state on precipitation behaviour. Laves phase particles formed quickly after few hours and the size of precipitates did not change significantly within 1,000 hours. The observed development of Laves phase particles was compared with thermodynamical calculations (TC-Prisma).
The creep properties of 17Cr2.5W0.5Nb0.25Si steel in different initial thermo-mechanical treatment states were tested at 650 °C. The influence of different cold rolling procedures, and heat treatments was investigated. Increased cold rolling deformation had a positive effect resulting not only from work hardening, but from the acceleration of Laves phase particle precipitation. The recrystallization annealed material exhibited significantly shorter creep life in comparison to the rolled material. Two promising heat treatments restoring the creep strength up to the level of rolled material were identified. Tempering at 540 °C accelerates the formation and reduces the size of strengthening Laves phase precipitates. Short term tempering at 800 °C causes dense precipitation of Laves phase particles at grain boundaries without detrimental influence on the morphology of Laves phase particles in the grain interiors. Dense precipitation of coarse Laves phase particles causes a retardation of grain boundary sliding in the later periods of creep exposure.

Überblick

Ziel der vorliegenden Arbeit war die Entwicklung und die Bewertung der mechanischen Eigenschaften von ferritischen HiperFer (**Hi**gh **per**fomrance **Fer**ite) Hochleistungsstählen mit einem Chromgehalt von 17 Gew%, deren Verfestigung durch Ausscheidung intermetallischer Laves-Phasenpartikel erreicht wird. Diese sollen in zukünftigen, ultrasuperkritischen Kraftwerksprozessen mit verbesserten Wirkungsgraden eingesetzt werden. Hierzu sind erheblich verbesserte Materialien mit hoher Beständigkeit gegen Heißgas- und Dampfoxidation sowie ausreichender Kriech- und Zeitstandfestigkeit erforderlich. Die Arbeit konzentrierte sich auf die Charakterisierung der Kriecheigenschaften eines 17Cr2.5W0.5Nb0.25Si Versuchsstahls. Zusätzlich wurden Kleinstschmelzen (17Cr3W0.5Nb0.25Si und 17Cr3W0.9Nb0.25Si), um den Einfluß geänderter chemischer Zusammensetzungen auf das Ausscheidungsverhalten zu analysieren.

Die Kriechfestigkeit von HiperFer Stählen wird durch eine möglichst homogene Verteilung feiner, thermodynamisch stabiler Laves-Phasenpartikel erreicht, während hohe Korrosionsbeständigkeit durch den vergleichsweise hohen Chromgehalt gewährleistet wird. Die Versuchsstähle wurden auf der Basis thermodynamischer Modellierung (Thermocalc) hinsichtlich Vermeidung der spröden (Fe,Cr)-σ Phase und Maximierung des Gehalts der verfestigenden C14 Laves-Phase vom Fe_2Nb –Typ optimiert. Alle Versuchsstähle wurden bei 650 °C ausgelagert, um die Rolle der chemischen Zusammensetzung und des thermomechanischen Behandlungszustandes auf das Ausscheidungsverhalten bewerten zu können. Die Ausscheidung der Laves-Phase erfolgt schnell (im Bereich einiger Minuten bis hin zu maximal 2 Stunden), ihre Größe nimmt innerhalb von 1,000 Stunden nicht nennenswert zu. Die experimentell beobachtete Entwicklung der Teilchengröße wurde mit thermodynamischen Modellrechnungen (TC-Prisma) vergleichen.

Die Kriecheigenschaften des 17Cr2.5W0.5Nb0.25Si Versuchsstahls in unterschiedlichen thermomechanischen Behandlungszuständen (unterschiedlicher Walzverfahren und Wärmebehandlungen) wurden bei 650 °C geprüft. Vergrößerte Umformgrade wirkten sich positiv aus, was nicht nur auf Warm-Kalt-Verfestigung, sondern auch auf die Beschleunigung der Laves-Phasenausscheidung zurückzuführen ist. Rekristallisationsgeglühtes Material zeigte dagegen deutlich geringere Zeitstandfestigkeit. Um dem entgegenzuwirken, wurden zwei vielversprechende Wärmebehandlungen zur Wiederherstellung der Zeitstandfestigkeit (bis auf das Niveau des gewalzten Materials) identifiziert. Tempern bei 540 °C beschleunigt die Bildung der Laves-Phase und reduziert deren Größe. Kurzzeitige Wärmehandlung bei 800 °C bewirkt eine dichte Belegung der Korngrenzen mit Laves-Phasenteilchen, ohne nachteiligen Einfluss auf die Morphologie der bei

Betriebstemperatur im Korninneren ausgeschiedenen Partikel. Die dichte Belegung der Korngrenzen bewirkt eine Verzögerung des Korngrenzengleitens, somit eine Verlängerung der Tertiärkriechphase und auf dieser Grundlage verbesserte Zeitstandfestigkeit.

Acknowledgements

I would like to thank to Dr. Ing. Bernd Kuhn for the possibility to work on Laves phase strengthened creep resistant steels. Successful completion of this work would not be possible without his enthusiasm and guidance. Furthermore, I am very grateful to Prof. Beck as well as Prof. Singheiser for their valuable help they gave me during my work in the Forschungszentrum Jülich and their constructive suggestions and comments. I hereby express my gratitude to all my colleagues who carried out all the mechanical tests and microstructural observations.

Chapter 1

Introduction

Modern societies are significantly dependent on sustainable and reliable supply of energy. The total primary energy consumtion of the world more than doubled between 1971 and 2010 and it is expected that this trend will continue, irrespective from predictive scenario [1] (Figure 1.1) The most significant sources of energy are oil, mainly used in transportation, and electricity. Production of electricity is mainly covered by fossil fuels [2], (Figure 1.2).

1.1 Requirements for modern steels used in power industry

An important aspect that influences design & development of materials for power industry is the demand for increased efficiency and electricity generation, because the efficiency of a thermal power plant is mainly influenced by temperature and pressure of life steam. The efficiency of steam power plants increased from 10% in 1910 up to 45% in 2010 (Figure 1.3a). In the same time, construction materials of superheaters changed from carbon steels used in the 1910's to austenitic steels used in the 2010's [3] (Figure 1.3b). The materials used in the construction of power plants should provide sufficient:

- creep resistance,
- firesede and/or steam corrosion resistance,
- temperature capability and heat resistance,
- low cycle fatigue resistance.
- resistance against thermo-mechanical fatigue

Other requirements can be resistance to type IV cracking in tube systems (waterwalls, superheaters, reheaters), and erosion resistance (turbine blades, vanes, and valves) [25].
Increased efficiency is not the only trend influencing R&D of steam power plants and materials. Another important trend is the so called *Energiewende*. The German Energiewende means

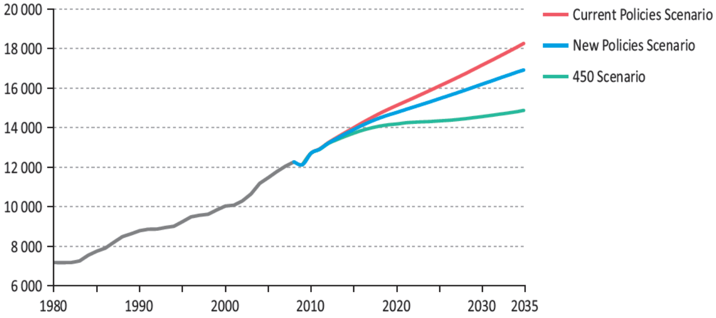

Figure 1.1: Predicition of the world primary energy demand by different scenarios [1]

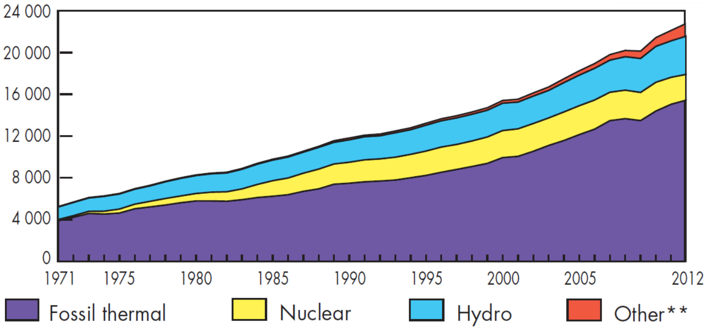

Figure 1.2: World electricity generation from 1971 to 2012 by fuel (TWh) [2]

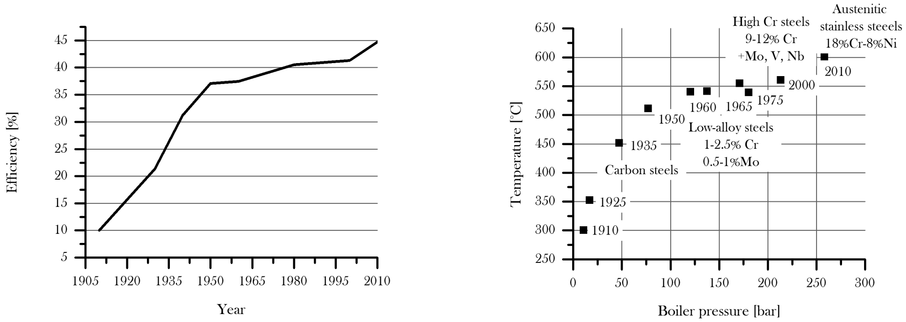

(a) Increase of power plant efficiency during the last century [% GCV]

(b) Application of materials for construction of a superheater

Figure 1.3: Change of efficiency of thermal power plants and materials used for their construction [3]

- mitigation of nuclear energy as a source of electricity,
- increase of renewables up to 50% in the next 30 years,
- load flexibility with frequent start-up and shut-down cycles of steam power plants,
- in combination with longer and more frequent downtimes.

From these requirements, it can be concluded that resistance against low cycle fatigue, thermo-mechanical fatigue, and interaction of those phenomena with creep, and corrosion will become more important in future.

1.2 Objective

Development of a new material for power plant industry is a process lasting for years or even decades. The critical aspect of the development is long term thermal stability of microstructure and ensuring required mechanical strength. Standard design lifetime of a steam power plant is in the range of $10^5 - 2 \cdot 10^5$ h. The minimum duration of a creep test of a material used for construction of a power plant should be at least one third of the design lifetime according to the recommendation of the European Creep Collaborative Committee (ECCC) [26]. Other selected tasks that are conected with development of a creep resistant steel are [11] :

- systematic investigations of the influence of heat treatment on creep behaviour;

- examination of the microstructure in the virgin condition and after long-term thermal and creep loading;
- systematic investigation of the influence of alloying elements;
- computer-aided alloy design methods (e.g. Thermocalc, DICTRA); and
- modelling of creep processes.

The presented thesis focuses on the initial development stage of a heat resistant fully ferritic 17wt% Cr steel. High performance ferritic - HiperFer - steel exhibts superior corrosion resistance ensured by high Cr content and microstructural stability ensured by fine precipitation of intermetallic Laves phase particles. The work continues and builds on the development of Crofer 22 H steel. Crofer 22 H is used for interconnect applications in solide oxide fuel cells. Experimental steels, developed in course of the Crofer 22H project, exhibit superior resistance against corrosion and thermo-mechanical fatigue, compared to standard 9-12 wt% Cr ferritic-martensitic steels, and satisfactory creep resistance [27, 28].
The experimental work includes analysis of short- and mid-term mechanical properties, like tensile, and creep strength tests; microstructural development at 650 °C with respect to the initial thermo-mechanical treatment state, and evaluation of the role of the initial thermo-mechanical state on creep properties. Precipiate evolution is accompanied by thermodynamic calculations using TC-Prisma software.

1.3 Outline

In Chapter 2, the strengthening mechanisms of creep resistant steels and complex requirements of them will be reviewed, basic information about precipitation processes in solid state matter will be provided. Brief introduction into stochastic creep modeling will be offered.
Chapter 3 will present the fabrication of investigated steel, used experimental equipment and characterization techniques.
In Chapter 4, the results will be represented. There will be presented alloying philosophy of HiperFer steels, results of recrystallization annealing, precipitation study, tensile experiments, creep experiments, and results of precipitate evolution modeling performed by TC Prisma software..
Chapter 5 will give a discussion about the influence of initial state a HiperFer steel on precipitation, and creep properties. Tensile creep experiments were there evaluated by a constitutive equation, results of time-temperature precipitation experiments are compared with results given by modeling software TC Prisma.
Lastly, chapter 6 will summarize the executed experiments and give conclusions.

Chapter 2

Literature review

2.1 Transformation in solid-state metals

Recrystallization [1] and precipitation of a secondary phase are common solid-state transformation processes in metals. Phase transformation of the matrix, like $\alpha \rightarrow \gamma$ transformation of iron, or martensitic transformation, is another common type of transformation process of metals. HiperFer steels do not exhibit any phase transformation of the matrix, because such steels possess an α iron matrix from solidification down to ambient temperatures. For this reason, only *recrystallization*, and *precipitation* are discussed in the following section.

2.1.1 Recrystallization and coarsening

Recrystallization

Deformed grains with a relatively high density of defects are replaced by new grains with lower defect density during recrystallization [29]. New crystals start to grow from areas with high stored energy, like e.g. twin intersections, slip-lane intersections, or grain boundary triple junctions [4].

The rate of recrystallization is influenced by two main aspects - *temperature* of recrystallization, and the amount of *deformation* energy stored in the material. Kinetics of recrystallization is commonly measured under isothermal condition and results of such experiments are depicted in Figure 2.1. The overall kinetics of recrystallization can be described by the common Avrami equation [29]:

$$X_V = 1 - \exp\left(-K\tau^n\right) \tag{2.1}$$

---

[1] Recovery as a process is sometimes counted together with recrystallization as *softening*, or *annealing* processes, but these two processes differ. Dislocation density is reduced during *recovery*, but new grains form and/or coarsen during *recrystallization* [4, 29]

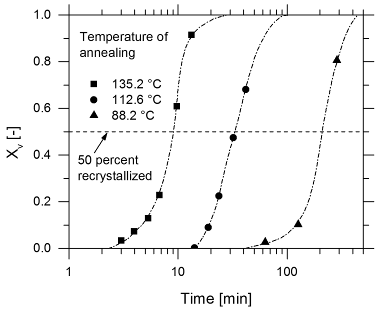

Figure 2.1: Isothermal recrystallization curves for pure copper cold rolled 98 % [4]

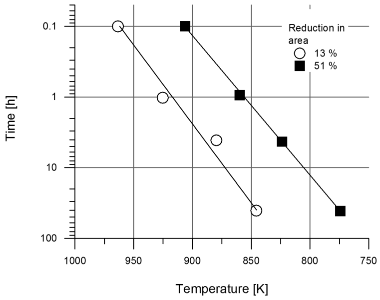

Figure 2.2: Temperature-time relationships for recrystallization of zirconium corresponding to two different degrees of prior cold work [4]

where	X_V	is the proportion of recrystallized area,
	τ	is the time of annealing,
	K	is a kinetic coefficient,
	n	is a kinetic exponent.

As mentioned in the preceding part of this section, the second aspect influencing the rate of recrystallization is the amount of prior deformation. Influence of deformation of zirconium on the time required to complete recrystallization is shown in Figure 2.2 [4]. The results show that higher cold deformation prior to recrystallization has a positive effect on kinetics.

Coarsening

The surface energy stored in the grain boundaries is a thermodynamic driving force for the coarsening of grains [4, 29]. Kinetics of recrystallization can be expressed by the formula:

$$D^2 - D_0^2 = K \cdot \tau \cdot \exp\left(\frac{-Q}{RT}\right) \tag{2.2}$$

where	D	is the average diameter of grains in time τ,
	D_0	is the average diameter of grains at the beginning of coarsening,
	K	is a time independent, but temperature dependent constant,
	τ	is the time of annealing,
	Q	is the activation energy of recrystallization.

Results of coarsening experiments are presented on α brass as an example. The influence of time and temperature on grain size of α brass is depicted in Figure 2.3.

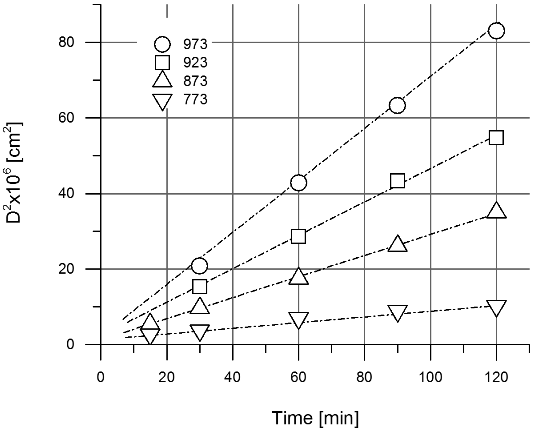

Figure 2.3: Grain-growth isotherms for αbrass [4]

2.1.2 Solid State Precipitation

Solid state precipitation is a phenomenon where relatively small particles of a new phase from an oversaturated solid solution are formed because of decrease of temperature, and/or exposure at sufficient temperature for a sufficient time. The following chapter closely follows monographs of Kozeschnik [5] and Porter [7].
The precipitation process consists of following phases (Figure 2.4):

- incubation,
- nucleation,
- growth,
- transition region, and
- coarsening.

Specific changes in size of particles (Figure 2.4b), the chemical composition of the matrix (Figure 2.4a), as well as development of phase fraction, and volumetric density can be attributed to a particular phase of precipitation [5, 6]. The particular stages will be briefly described in the following section.

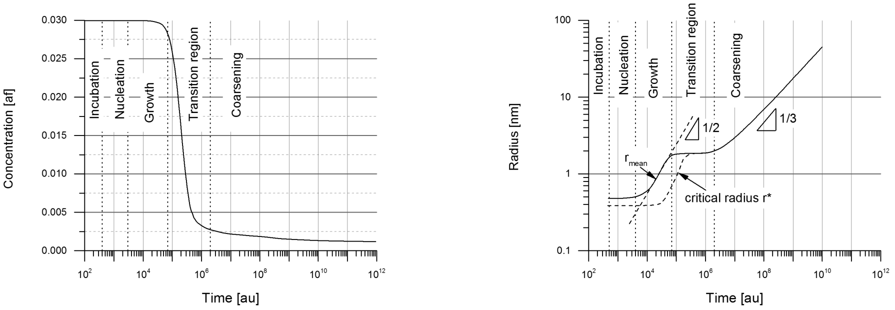

(a) (b)

Figure 2.4: Evolution of matrix B-content (a), and (b) mean/critical radius during precipitation [5, 6]

Incubation and nucleation of precipitates

Formation of a nucleus, irrespective if the transformation is ***vapor→liquid***, ***liquid→solid***, or ***solid→solid***, is given as the difference between the change of ΔG_{surf} (free energy required to create unit an area of the precipitate/matrix interface) and ΔG_{vol} (specific volume free energy change on nucleus formation). ΔG_{surf} is a function of interfacial energy γ and surface of a nucleus. Assuming a globular nucleus, the change of free enthalpy during precipitation can be expressed as

$$\Delta G = -V\Delta G_{vol} + \Delta G_{surf} = -\frac{4}{3}\pi r^3 \Delta G_{vol} + 4\pi r^2 \gamma \tag{2.3}$$

The extremal values of Equation 2.3 gives the radius of a critical nucleus as

$$r^* = -\frac{2\gamma}{\Delta G_{vol} - \Delta G_{surf}} \tag{2.4}$$

A schematic course of change of free enthalpy is shown in Figure 2.6; all the nuclei smaller than r^* are not stable and will dissolve spontaneously. The time that is necessary to form supercritical nuclei is commonly denoted as the ***incubation period*** or the ***incubtaion time*** τ.

Soisson and Martin [6] presented results of numerical simulations of precipitation starting from two states; the first one was fully random solid solution and the second one represented simulated annealing just above the solubility limit. Modeled results of nucleation kinetics are presented in Figure 2.7. When the precipitation started from a random solution state (●), a clear shift of the steady growth of supercritical clusters is visible; it means that an incubation period prior to nucleation period was present. In contrary, if the precipitation started from the annealed state (○), the amount of supercritical clusters increases almost instantaneously.

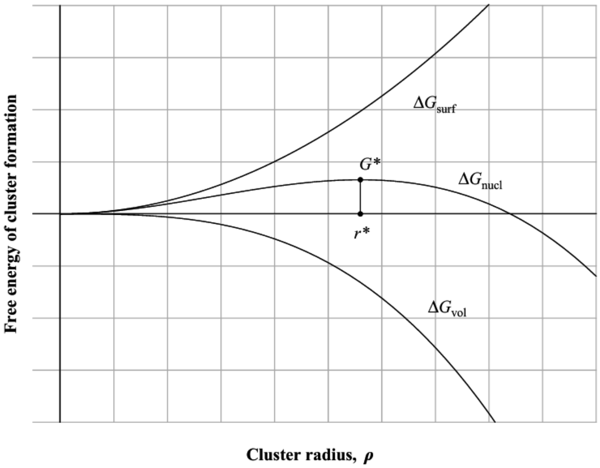

Figure 2.5: Schematic course of a function of the thermodynamic barier [5]

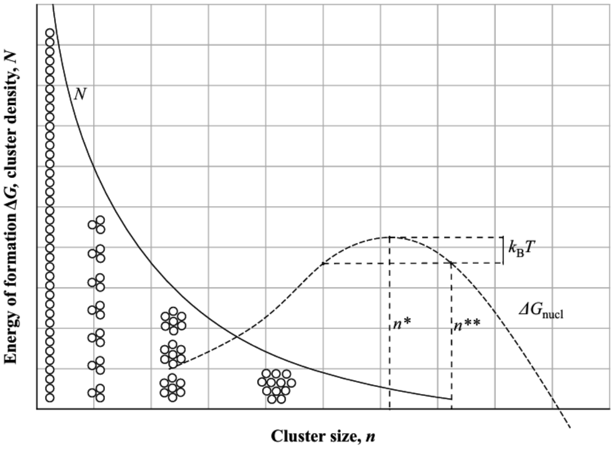

Figure 2.6: Equilibrium cluster distribution (solid line) and free energy of nucleus formation (dashed line) at the beginning of precipitation [5]

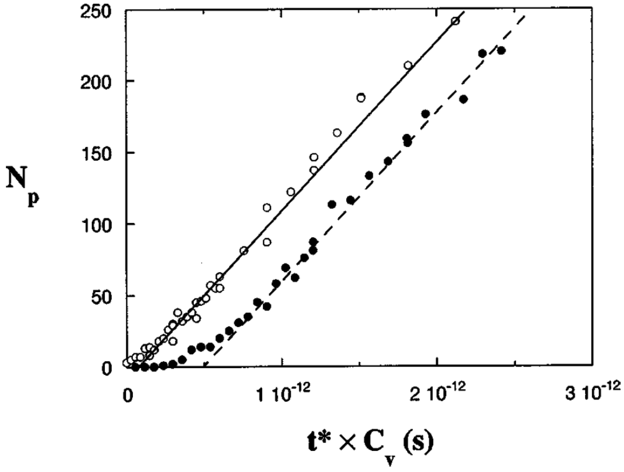

Figure 2.7: Analysis of solid-state nucleation kinetics—evolution of the number of supercritical clusters N_p at the beginning of the precipitation process [6]

There are two types of nucleation - ***homogeneous***, and ***heterogeneous***. Homogeneous nucleation takes place within a perfect homogeneous crystal structure and is a result of a random fluctuation of chemical composition of a macroscopically homogeneous solid solution [5]. It does not require the presence of crystallographic defects, e.g. vacancies, dislocations, or grain boundaries. But it is less probable compared to heterogeneous nucleation because it requires a higher activation energy to overcome the nucleation barrier [29].
Nucleation in solids is almost always heterogeneous [7]. Suitable nucleation sites are:

- zero-dimensional lattice defects like vacancies, divacanies, and foreign atoms (Figure 2.8 a),
- one-dimensional lattice defects like edge dislocations (Figure 2.8 b),
- two-dimensional lattice defects like high-angle grain boundaries (Figure 2.8 c),
- three-dimensional lattice defects like incoherent inclusions (Figure 2.8 d).

The rate of nucleation can be ordered from the slowest to the fastest roughly [7]

1. homogeneous sites,
2. vacancies,

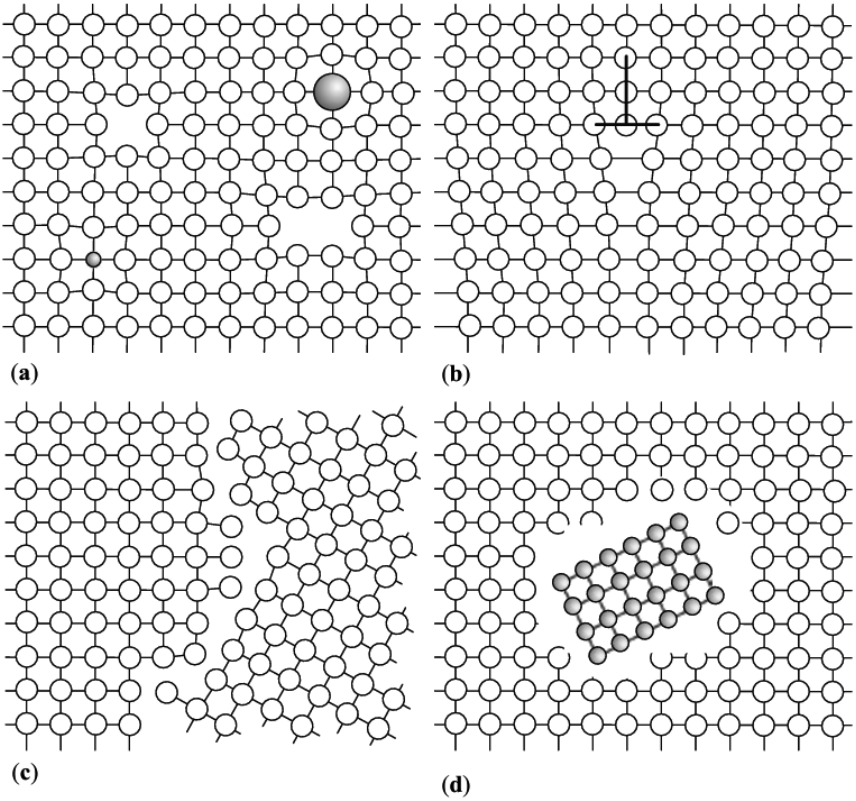

Figure 2.8: Lattice defects acting in heterogeneous precipitation; (a) a mono- and a divacancy, larger and smaller atoms, (b) edge dislocation, (c) high angle grain boundary, and (d) incoherent inclusion [5]

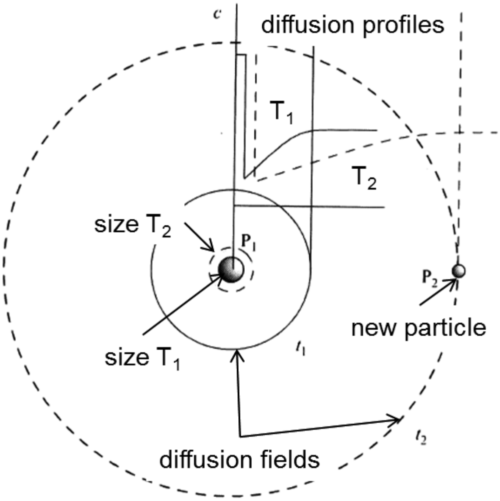

Figure 2.9: Formation of a new nucleus P_2 in the presence of an existing particle P_1 [5]

3. dislocations,
4. stacking faults,
5. grain boundaries and interface boundaries,
6. free surfaces.

The formation of new nuclei is also influenced by already existing precipitates. Nucleation of a new particle in the presence of an already existing precipitate is depicted in Figure 2.9. The existing particle P_1 grew to a particular size within t_1 (in the center of the Figure). The diffusion field, enveloping the particle P_1, with lower concentration of particle forming elements is represented by the solid circle. The presence of the particle P_1 has no influence on precipitation of the particle P_2 if its nucleation starts in time t_1. Within time t_2, the primary particle P_1 grew further and the diffusion field around the particle has reached to further distance (represented by the big dashed circle). The probability of nucleation of a new particle within the depleted area (big dashed circle) decreases rapidly and becomes rather unlikely [5]

Diffusion-controlled growth of precipitates

The first two stages of precipitation, *initiation* and *nucleation*, are stochastic processes. The growth of a precipitate in a supersaturated solution requires long-range transport of solute

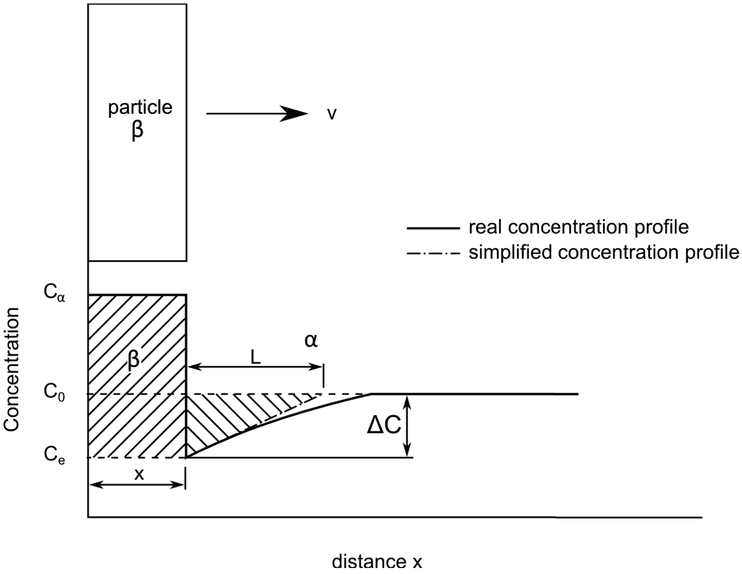

Figure 2.10: Diffusion-controlled growth of the precipitate β from supersaturated solution α

elements to the growing particle. ***Diffusion*** processes are deterministic in nature and can be described by appropriate evolution equations [5].

A schematic situation depicting diffusion-controlled growth of a precipitate β from a supersaturated solution α is shown in Figure 2.10. Because the concentration of solute in the precipitate C_β is higher than in the matrix C_α, a depleted area around the growing particle will be present. Concentration of the solute at the interface is assumed to be equal to the equilibrium value C_e because growth of the particle is diffusion-controlled and local equilibrium at the interface can be assumed.

The growth rate will depend on the concentration gradient $C_\beta - C_e$ at the interface and the interdiffusion coefficient D

$$v = \frac{dx}{dt} = \frac{D}{C_\beta - C_e} \cdot \frac{dC}{dx} \tag{2.5}$$

According to Zener's analysis of precipitate growth [5, 7], the width of the diffusion zone L is determined by area unity of the two shaded areas in Figure 2.10 [7], i. e.

$$(C_\beta - C_0)x = \frac{L\Delta C_0}{2}$$

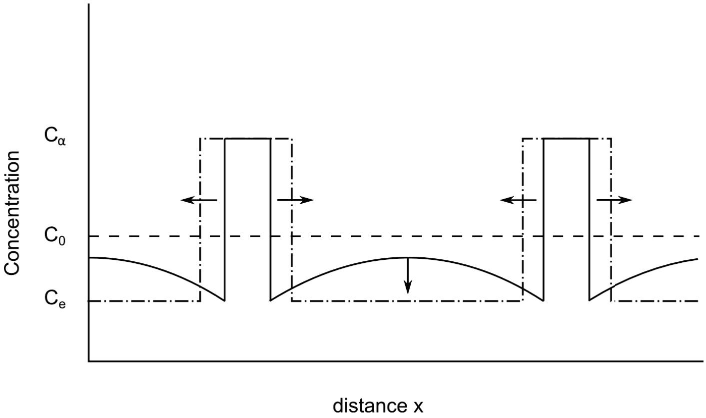

Figure 2.11: Interference of overlapping diffusion fields of simultaneously growing precipitates (full line), and after the end of particles growth (broken line)

where x is the thickness of the slab. The growth rate than becomes

$$v = \frac{D(\Delta C_0)^2}{2(C_\beta - C_e)(C_\beta - C_0)x} \tag{2.6}$$

When the diffusion fields of parallelly growing particles start to overlap (Figure 2.11), Equation 2.6 will not be valid any more and the rate of particle growth will decrease more rapidly and, finally, growth will stop (dashed line in Figure 2.11).

The growth rate of a precipitate is significantly influenced by temperature and oversaturation of the solid solution (Figure 2.12). The influence of the concentration of an element on the limit of solubility is depicted in the left figure schematically. At temperatures slightly below the solubility, the diffusion rate is high, but oversaturation is low resulting into a low rate of particle growth. At low temperatures, oversaturation is high but diffusion rate is low, again resulting in a low growth rate. The maximum growth rate of precipitates is observed at intermediate temperatures. The position of the growth rate maximum is not only depending on temperature, but also on composition of the matrix. The maximum rate is observed at higher temperatures when the content of the element B (solid V line in the left part of Figure 2.12) compared to lower concentration (broken line).

2.1.3 Precipitate Coarsening

Coarsening of precipitates, or Ostwald ripening, is the last stage of the precipitation process, when smaller precipitates in the vicinity of bigger precipitates dissolve and the dissolved solutes

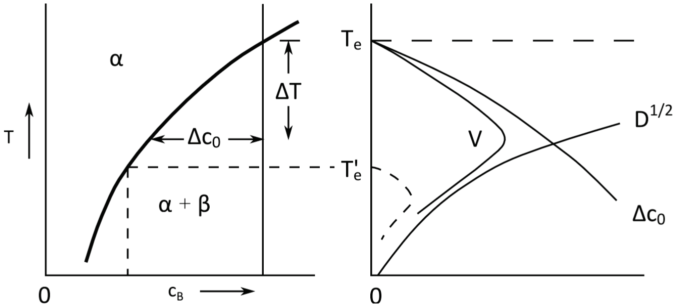

Figure 2.12: Influence of temperature T and oversaturation Δc_0 on the position and growth rate of a precipitate [7]

redeposit on the surfaces of bigger precipitates. The thermodynamic driving force for this phenomenon is the minimization of total interfacial area; because bigger particles have a smaller surface to volume ratio. The flux of solutes from smaller to bigger precipitates is controlled by diffusion.

The Lifschitz-Slyozof-Wagner (LSW) theory, that is being used for the description of the coarsening phenomenon [5, 30], explains the development of the mean particles radius $\bar{r}$ of the precipitates and their size distribution, and the evolution of volumetric density N_V. In summary [5], the evolution of the mean radius and number desity are given by the relations:

$$r^*(t) = r_0^* \left[1 + \frac{t}{\tau_D}\right]^{\frac{1}{3}} \tag{2.7}$$

$$N_V(t) = m_0 \left[1 + \frac{t}{\tau_D}\right]^{-1} \tag{2.8}$$

The time constant τ_D in the previous equations is defined as [5]

$$\tau_D = \gamma_D \frac{\left(c_B^\beta - c_B^\alpha\right) RT}{2\gamma D_B^\alpha c_B^\alpha v^\beta} \left(r_0^*\right)^3 \tag{2.9}$$

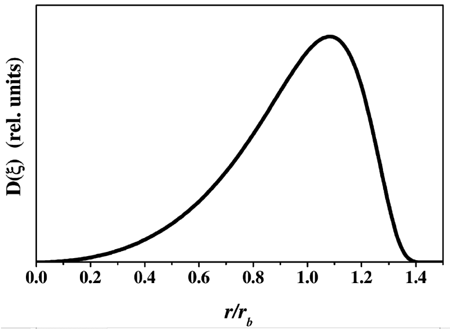

Figure 2.13: Predicted stationary size distribution for diffusion controlled coarsening according to the classical LSW theory [8]

where γ_D is the specific interfacial energy of the particle-matrix interface,
c_B^β is the solute concentration in the particle D
c_B^α is the solute concentration in the matrix,
D_B^α is the diffusivity of the solute in the solid solution,
v^β is the molar volume of the precipitate,
r_0^* is the critical radius,
r^* is the mean radius.

The size distribution of radii of the particles at any given time has the following form [8]

$$D(\xi) = \kappa\xi^2\left(\frac{3}{3+\xi}\right)^{\frac{7}{3}}\left(\frac{1.5}{1.5-\xi}\right)^{\frac{11}{3}}\exp\left(\frac{-\xi}{1.5-\xi}\right) \tag{2.10}$$

where ξ is the ratio of a particle radius over the mean radius and
κ is a time dependent value by the relation $\kappa = \kappa_c/(1+t/\tau_D)^{4/3}$.

The course of the Equation 2.10 is plotted in Figure 2.13. Such distribution is constant during the whole coarsening. The maximum radius of a precipitate according to the LSW theory is just about a factor of 1.5 bigger than the mean radius of all the particles.

Influence of the initial thermo-mechanical treatment state on precipitation

The aim of the previous section is not to give a complete overview of thermodynamical and mathematical descriptions of precipitation, as undertaken in monographies like Kozeschnik [5], Porter [7], or Martin [30]. In the same manner, heat treatment and thermomechanical treatment

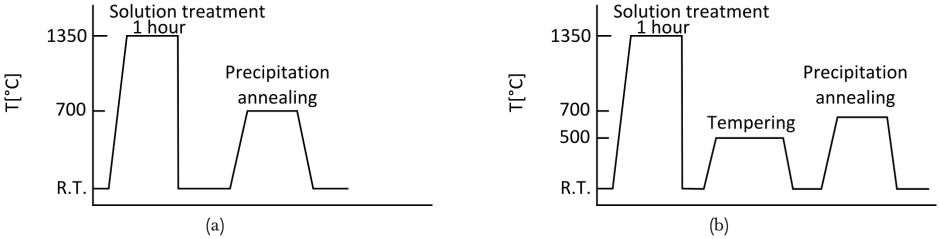

Figure 2.14: Schematic sketch of heat treatment procedures; (a) one step precipitation annealing, (b) two step annealing

of technical materials is a broad discipline and there will be presented just two cases in this section, namely the influence of *low temperature tempering*, and *rolling* on precipitation of C14 Fe_2Nb type Laves phase particles.

Wert at all [9] studied the influence of combined heat treatment on the elimination of **P**article **F**ree **Z**ones (PFZ) in a Fe_2Nb Laves phase strengthened Fe-rich, carbon free ferritic steel. The initial heat treatment prior to precipitation annealing at 700 °C for 1 h was solution treatment at 1350 °C for 1 h in one case (Figure 2.14a), and solution treatment at 1350 °C for 1 h followed by tempering at 500 °C in the second case (Figure 2.14b).

The efficiency of low temperature tempering prior to precipitation annealing on the elimination of PFZ alongside grain boundaries is illustrated in Figure 2.15. The specimen without tempering exhibited about 5 μm wide PFZs (Figure 2.15a), whereas the grain boundaries are hardly visible in the sample with two step heat treatment (Figure 2.15b). The overall size of the particles in the sample with 2 step heat treatment (tempering + precipitation annealing) is smaller (Figure 2.16b) compared to the sample with one step tempering (Figure 2.16a).

Wert [9] explained this phenomenon by an analogy to age hardenable AlCu material assuming the precipitation sequence *solid solution* → *Guinier Preston Zone* (GPZ) → *Laves phase precipitate*, whereas the GPZs are able to form in Nb depleted zones around grain boundaries. Such explanation does not sound credible if it is compared with up to date information about precipitation of C14 Laves phase particles from the ferritic matrix. Galimberty at al. [10] studied precipitation of Fe_2W C14 Laves phase in an Fe20Co18W alloy by HRTEM. Direct precipitation of Laves phase particles from the solid solution was observed by high resolution transmission electron microscopy and the observation was supported by crystallography based explanation. Possible transformation of BCC to C14 crystal structure is presented in Figure 2.17.

The second example of thermomechanical treatment of C14 Laves phase forming materials discusses the influence of rolling parameters on precipitation. Trotter at al. [31] compared precipitation behaviour of a high alloyed alumina forming austenitic (AFA) steel with 20 wt% Cr and 30 wt% Ni forming Fe_2Nb Laves phase particles at 700, and 800 °C. The studied samples were

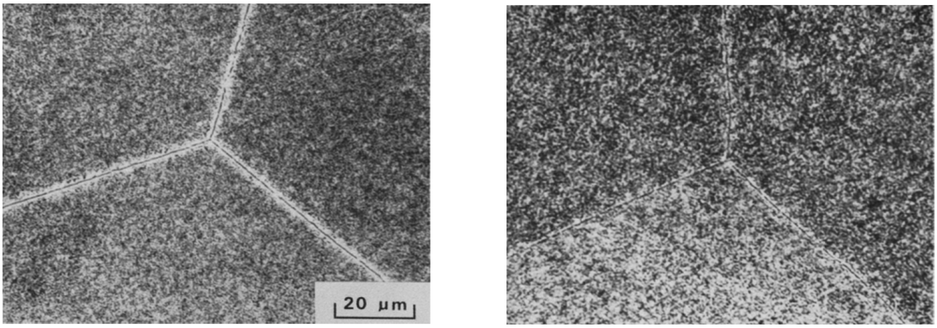

(a)

(b)

Figure 2.15: Macrostructure of the precipitation treated samples without (a) and with (b) tempering [9]

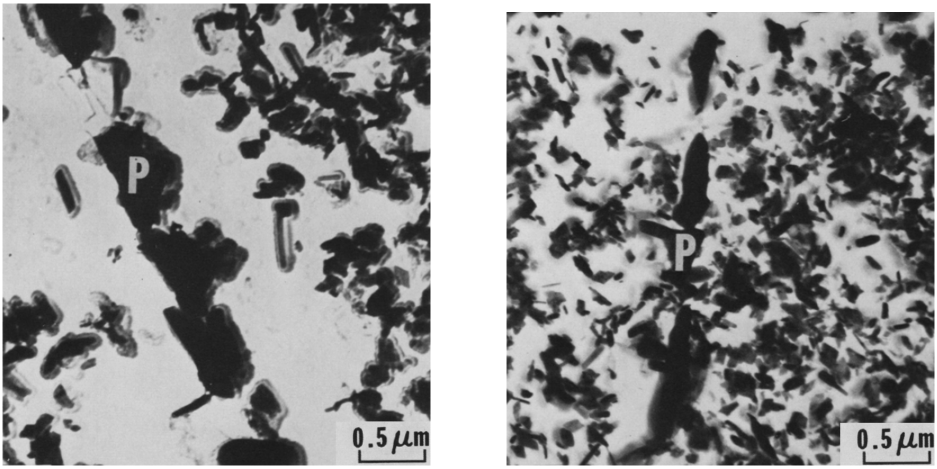

(a)

(b)

Figure 2.16: TEM image of an extraction replicas taken from a grain boundary of material without (a) and with (b) tempering prior to precipitation annealing [9]

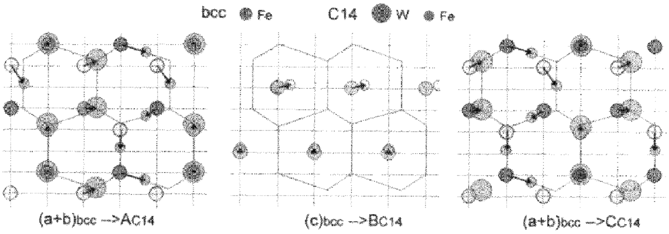

Figure 2.17: Diagrams presenting possible atomic displacements from bcc to C14 lattice. a, b, and c relate to the atomic planes along <111> in the bcc lattice and A, B, C to the (11-20) planes in the C14 lattice [10]

without cold work, with 50 %, and 90 % thickens reduction performed during cold working.
The results of annealing at 700 °C for 240 h are presented in Figure 2.18. No precipitates were observed in the sample without cold work (Figure 2.18a), some in the sample with 50% cold work (Figure 2.18a) with an average particle size 137 ± 70 nm, and more in the sample with 90% cold work with an average particle size 127 ± 71 nm.
The results of annealing at 800 °C for 240 h are presented in Figure 2.19. The biggest amount of particles with the smallest average diameter of 252 ± 167 nm was observed in the sample without cold work (Figure 2.19a) prior to the precipitation annealing. Significantly elongated Laves phase particles were observed in the sample with 50% of cold work prior to annealing. Their average particle size was 284 ± 140 nm. Globular particles with an average diameter of 301 ± 201 nm were found in the sample with 90 % of cold work.
It is clear from the previous discussion that enhanced dislocation density emerging from increased cold working can have a positive effect on precipitation at lower temperatures (compare the micrographs in Figure 2.18), but it can significantly accelerate coarsening at higher temperatures (see the micrographs in Figure 2.19). Dark particles in Figure 2.18 and Figure 2.19 are NiAl precipitates.

2.2 Creep

Creep of metals (and alloys) is defined as the time dependent plastic deformation under constant applied load, or stress at temperatures roughly above $0.4 \cdot T_m$, where T_m is the melting temperature in Kelvin [16]. For experimental convenience and closer approximation to technical reality, creep tests are mostly conducted under constant load [11]. A creep curve has commonly three stages like depicted in Figure 2.20a. After the intrinsic deformation ϵ_0, the creep rate $\dot{\epsilon} = \frac{d\epsilon}{dt}$ decreases up to time t_1, then the creep rate $\dot{\epsilon}$ is constant up to time t_2, and on the end, the creep rate increases up to fracture (Figure 2.20b).
In Stage I, the creep rate decreases because of work hardening, decrease of free, and/or mo-

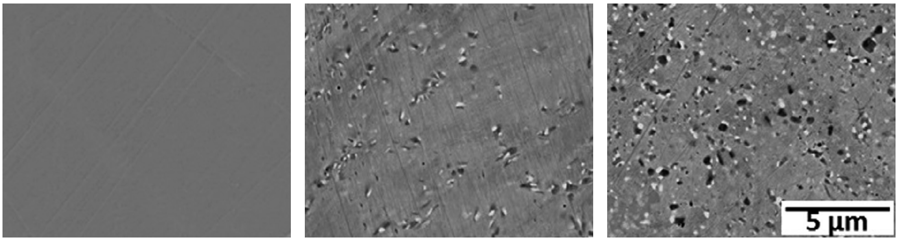

(a) (b) (c)

Figure 2.18: Backscattered electron images of AFA steel aged at 700 °C and 240 h; (a) without cold working; (b) after 50% of cold work; and (c) after 90 % of cold work

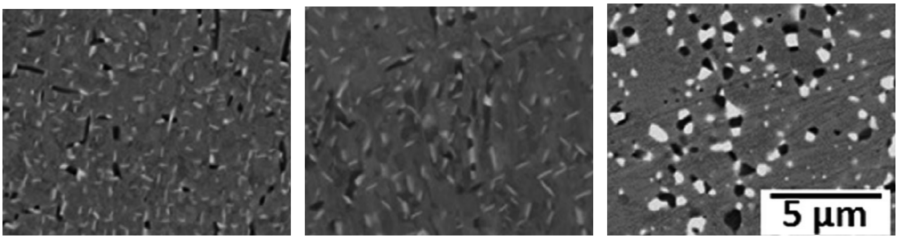

(a) (b) (c)

Figure 2.19: Backscattered electron images of AFA steel aged at 800 °C and 240 h; (a) without cold working; (b) after 50% of cold work; and (c) after 90 % of cold work

bile dislocations. In Stage II, when the creep rate remains constant, hardening processes (e.g. generation of new dislocations) and softening processes (e.g. annihilation of dislocations) are in a dynamic balance. Softening processes and formation of cavities become dominant in Stage III [16, 32].

With increasing temperature or applied stress, Stage II of creep shortens until it is reduced to an inflection point of the creep curve (Figure 2.21a). In this case, no steady state creep rate, but a minimum creep rate $\dot{\epsilon}_{min}$ occurs (Figure 2.21b).

In some cases, an inverse primary Stage I is observed, during which the creep rate increases up to a particular deformation and then starts to decrease, as it is common for Stage I of creep. This behavior is called ***sigmoidal creep*** (Figure 2.22). Such phenomenon was observed in a broad range of materials e.g. in Cu-Al alloys (Figure 2.22a) [33], oxide dispersion-strengthened steels [34], or nickel based monocrystalline alloy (Figure 2.22b) [35]. Explanations of this phenomenon are varying [32, 33, 35, 36]. Evans and Wilshire suppose that sigmoidal creep of 70-30 α brass

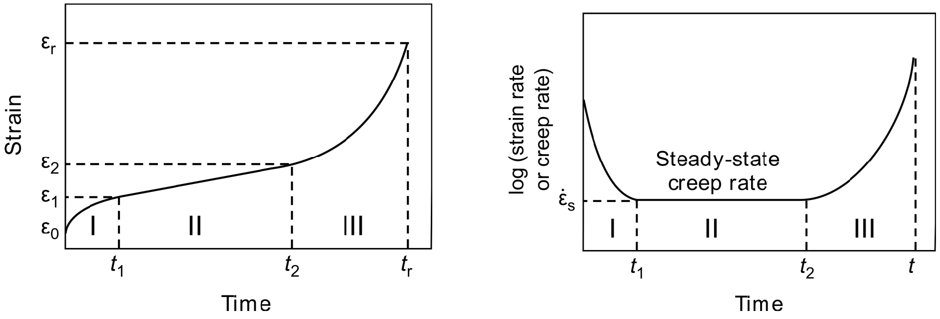

(a) Creep deformation curve

(b) Creep rate curve

Figure 2.20: Typical creep deformation (a) and creep rate (b) curves showing the typical three stages [11]

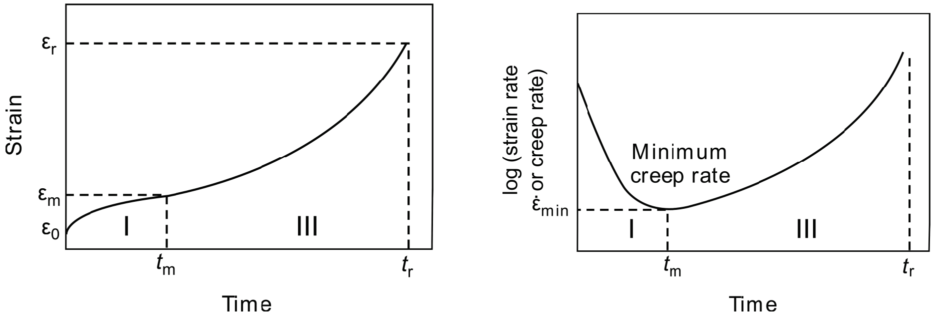

(a) Creep deformation curve

(b) Creep rate curve

Figure 2.21: Creep deformation (a) and creep rate (b) curves without the secondary stage [11]

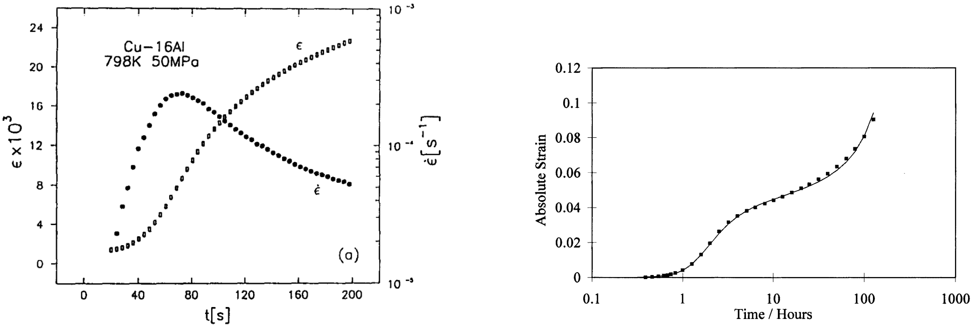

(a) Sigmoidal creep deformation and creep rate curves of a Cu-16Al solid solution alloy [33]

(b) Sigmoidal creep curve of CMSX-4 at 1023K and 820MPa [35]

Figure 2.22: Sigmoidal creep behavior in a solid solution alloy (a), and in a nickel based superalloy (b)

is caused by the destruction in short-range order in α brass [32], dynamic strain-aging is a suggested mechanism in Zr [32]. But the formation of dislocation substructures is prevailingly proposed as the responsible mechanism of sigmoidal creep in a wide range of materials [32, 33, 35, 36].

A deformation mechanism map is a graphical representation of the dominant deformation mechanism in a material exposed to particular loading (T, σ) conditions. Deformation mechanisms effective during steady-state creep (StageII) are plotted in such a map [11, 12]. An example of a map for pure nickel is depicted in Figure 2.23. The creep rate $\dot{\epsilon}$ is plotted as a function of homologous temperature T/T_m over stress normalized by shear modulus σ_s/μ[2]. The deformation mechanisms are divided into four groups:

1. *Plasticity* - dislocation glide is the dominant mechanism.
2. *Power-law creep* - thermally activated glide and/or climb of dislocations are the dominant mechanisms.
3. *Coble creep* - limited by grain boundary diffusion.
4. *Nabarro-Herring creep* - limited by lattice diffusion.

---

[2] Sheer modulus is being denoted as μ or G

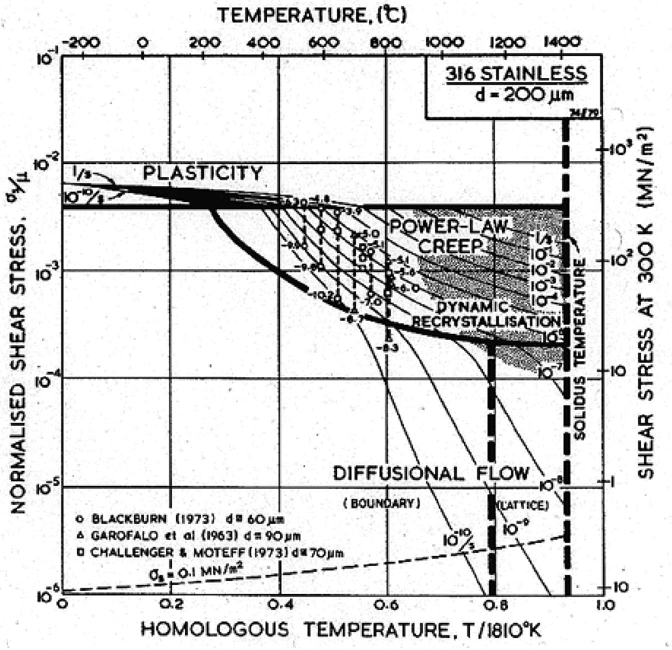

Figure 2.23: Creep deformation map of 316 stainless steel [12]

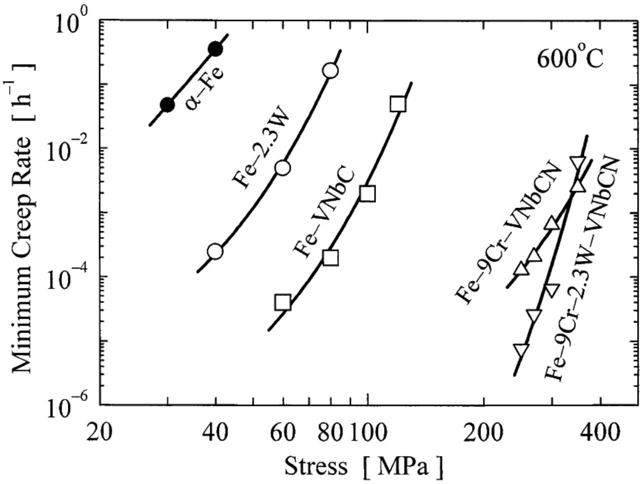

Figure 2.24: Minimum creep rates of ferritic steels at 600 °C [13]

2.2.1 Strengthening mechanisms of creep resistant steels

There is a broad range of strengthening mechanisms of creep resistant steels [11–13, 37]. The basic mechanisms can be roughly divided into *solid solution* hardening, *precipitation* hardening, and *grain boundary* strengthening.

Solid solution strengthening

Substitution atoms in a matrix cause distortion of the lattice, which reacts elastically with the generation of a stress field around a dislocation [29]. Solid solution strengthening can be expressed analytically [38] by:

$$\sigma_{SS} = K_i \cdot C_i \tag{2.11}$$

where σ_{SS} is the strengthening attributed to solid solution, K_i the strengthening coefficient for 1 at% of alloying element i, and C_i is the atomic percentage of the alloying element i in the solution. The most common elements used for solid solution strengthening in creep resistant steels are Cr, W, Mo, and Co. The decrease of creep rate of α-Fe by the addition of 2.3 wt% W is depicted in Figure 2.24 [13].

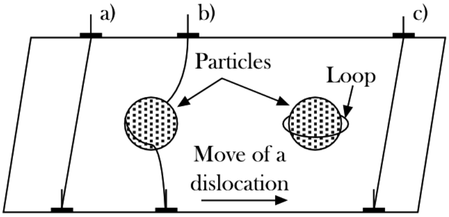

Figure 2.25: Orowan bowing over a particle [14]

Particle strengthening

Particles represent obstacles to the free movement of dislocations. Their properties and thermal stability during creep are one of a key issues in the design of creep resistant steels. At room temperature, for a diameter up to 3 nm the dislocations cut precipitates (***Friedel cutting***). Above this diameter the ***Orowan looping*** mechanism is preferred [39]. The Orowan stress σ_{or} is given by [37]:

$$\sigma_{or} = 0.8 \cdot \frac{M \cdot G \cdot b}{\lambda} \tag{2.12}$$

where ***M*** is the Taylor factor ($\simeq 1.7$ [12]), ***G*** is the shear modulus, ***b*** is the magnitude of the Burgers vector, and λ is the mean interparticle spacing.

The Orowan mechanism of interaction between a particle and a dislocation is shown in Figure 2.25. A particle, which is big enough, represents an invincible obstacle for the free movement of the dislocation. A free dislocation moving towards the particle (a) starts to bow (b). If the shear stress in the slip plane is big enough, the dislocation creates a loop around the particle and moves further on (c) [14].

At higher temperature, when diffusion processes are effective enough, and at stresses lower than σ_{or}, dislocations can bypass particles by local or general climb. The mechanisms of general and local climb are depicted in Figure 2.26. The additional length of a dislocation for the general climb mechanism is smaller than for the local climb mechanism, on the other hand it requires transport of more material. Blum and Repich suggested in [15], that the stresses required for climb are:

$\sigma_{lc} = 0.2 \cdot \sigma_{or}$ in case of the local climb and
$\sigma_{lc} = 0.004 - 0.02 \cdot \sigma_{or}$ in case of the general climb.

The effect of particle strengthening on the minimum creep rate is shown in Figure 2.24; the minimum creep rate of α-Fe decreases about more than three orders of magnitude with the addition of V, Nb, and C, which form (V, Nb)- carbides.

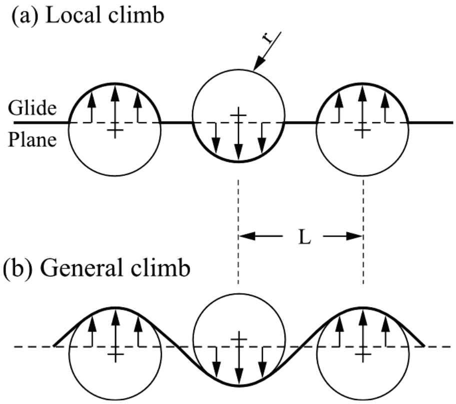

Figure 2.26: (a) Local, and (b) general climb over particles [15]

Grain boundary strengthening

Grain boundaries act as impenetrable barriers for the movement of dislocations. The smaller the grains are, the higher the density of grain boundaries per volume of material is and the more effective this type of strengthening becomes. Fine grain austenitic steel TP347HFG is a typical example of the positive influence of grain refinement on creep strength. Creep strength curves of standard, coarse grain TP347H, and the novel, fine grain TP347HFG steel are depicted in Figure 2.27[3]. Enhanced creep properties are caused by the different heat treatment which is employed to form finer grains - ASTM grain size 8 in case of TP347HFG, and 4-5 in case of TP347H. Fine dispersion of NbC particles is formed during modified heat treatment in the novel TP347HFG.

Finer grain structure may have a negative effects on the other hand: grain boundary sliding may control deformation at high temperatures, if the grains are not effectively covered by precipitates [16]. Also, grain boundaries represent paths for increased diffusion. Diffusion controlled creep that is sensitive on grain size is called Coble creep Figure 2.23. The rate of steady state creep during Coble creep decreases with reduction in grain boundary length, ie. with increasing grain size [16].

Dislocation controlled creep strengthening

Dislocations are linear defects in the crystal lattice. The motion of dislocations produces elasto-plastic deformation [40]. The free movement of dislocations can be restricted by other dis-

---

[3] The creep rupture data were taken from [14] and evaluated by the author using creep time to rupture Sovietl model

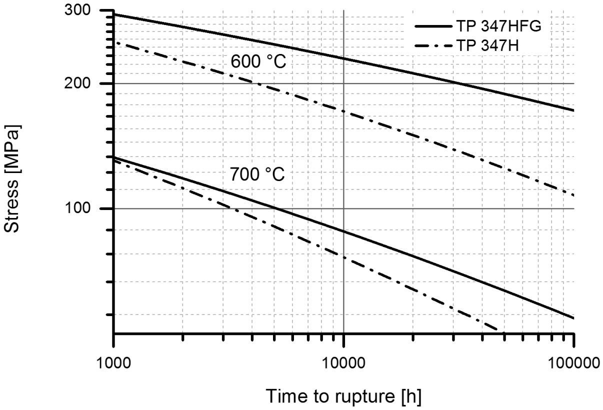

Figure 2.27: Creep rupture strength of austenitic steels TP347H, and TP347HFG [14]

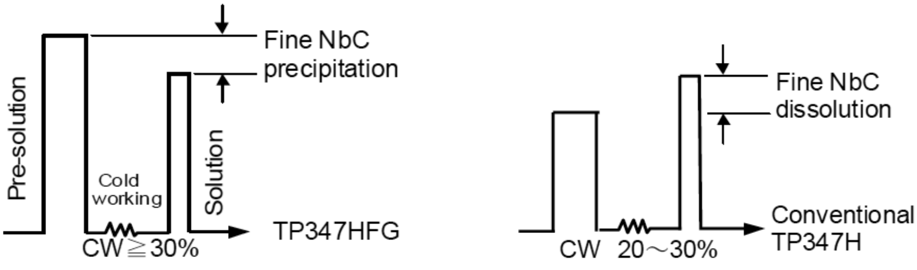

(a)

(b)

Figure 2.28: Thermomechanical treatment of an 18Cr-12Ni-Nb steel, (a) the novel TP347HFG, and (b) the standard TP347H [14]

locations. Such phenomenon is called *dislocation hardening*. Dislocations can originate from phase transformations like in ferritic-martensitic steels, cold or hot working resulting e.g. from rolling of the material, or work hardening resulting from deformation of the material during creep [11, 13, 37]. Dislocation hardening is most pronounced during short term creep, but its influence diminishes at prolonged time [37]. On the other hand, an excess of dislocations accelerates precipitation of particles within the matrix [7, 40].

The effect of enhanced dislocation strengthening caused by phase transformation on the decrease of the minimum creep rate is depicted in Figure 2.24. The creep rate of tempered martensitic steel (labeled Fe-9Cr-VNbCN) decreases drastically compared to a steel strengthened just by MX particles (Fe-VNbC).

The Fe-9Cr-2.3W-VNbCN steel , where all the three strengthening mechanisms—*solid solution*, *particle*, and *dislocation* strengthening—exhibits the lowest minimum creep rate of the five presented materials (Figure 2.24).

2.2.2 Development of dislocation structures in particle strengthened materials

Dislocation controlled creep of metallic materials can be divided into two groups. The stress exponent n is equal to about three for the so called Class A materials, and approximately equal to five for the Class M materials [41]. A- and M-class behavior do not just represent a difference in the values of the stress exponent n, but in the development of dislocation structure during creep. The discussion of microstructure development of particle strengthened materials closely follows the work of Blum and Repich [15], and Raj [42].

Primary creep

M class development

The dislocation structure evolution of materials with a relatively low initial density of dislocations during primary creep can be divided into three subsequent steps: the first is the increase in free dislocation density ρ_i immediately after applying the mechanical load. In metal class materials with a high fraction of free, mobile dislocations, the movement of dislocation is controlled by solid solution strengthening and leads to more or less viscous motion of the free dislocations. In the second step, the dislocations form heterogeneous structures called cell structure. The subgrain structure starts to form at grain boundaries and continues untill the whole grain interior is divided into subgrains. During the formation of substructures, the total density of dislocations $\rho_i + \rho_b$, where ρ_b represents dislocations stored in subgrain boundaries, increases slightly, while ρ_i decreases slightly in class M materials. The subgrain boundaries act as obstacles to the glide of dislocations in the M class materials.

A class development

The tendency to form subgrains during creep is low, or even non-existent in A class creep [16]. Dislocations are usually homogeneously arranged in a matrix and pinned to particles. The Ni-

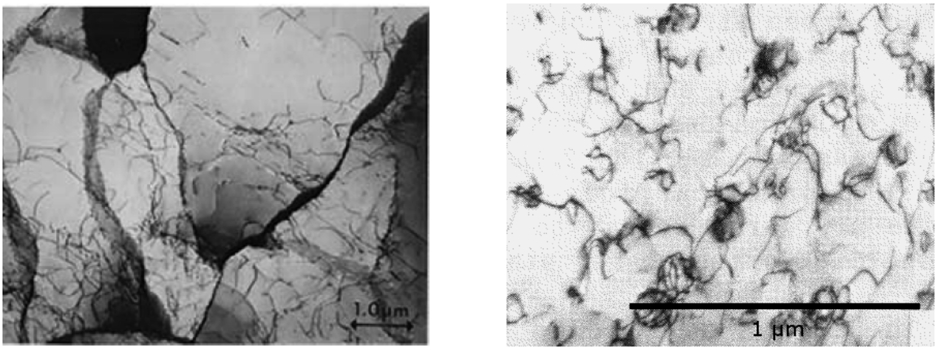

(a) Subgrains in AISI 304 stainless steel torsionally deformed at 865 °C at $\dot{\epsilon} = 3.2 \times 10^{-5} s^{-1}$ to a strain of 0.38 [32]

(b) homogeneously distributed dislocations bypassing γ' particles in Nimonic PE 16 [15]

Figure 2.29: TEM micrographs of the evolved microstructure during Class M (a), and Class A (b)

base alloy PE-16 is a typical example. The alloy is strengthened by homogeneously dispersed γ' particles and it has a negligible tendency to form subgrains during creep, whereas dislocations are homogeneously distributed in the alloy.

A fully developed subgrain microstructure, formed in the course of M-class creep, is shown in Figure 2.29a. An example of a homogeneous distribution of dislocations, formed during A-class creep, is depicted in Figure 2.29b.

Secondary creep

In the secondary creep regime softening (e.g. recovery of the dislocations structure, degradation of particle strengthening, and damage accumulation) and hardening (e.g. work hardening and/or precipitation of new particles) are in balance. A power law, describing a particle strengthened material, is given by the equation:

$$\dot{\epsilon}_S = A \cdot (\sigma - \sigma_p)^{n_o}, \tag{2.13}$$

where $\dot{\epsilon}_S$represents the steady state creep rate, σ the applied stress, σ_p describes particle strengthening, and n_o denotes the power law exponent.

The value of the power law exponent is not a constant for all the testing conditions, it may vary significantly with the applied stress. In Al-3.3 at.%Mg and Al-5.6 at.%Mg alloys variation of the stress exponent from 3 (class A behaviour) to 4.6 (class M behaviour) was observed [43]. Transition between different types of creep behavior is depicted in Figure 2.30.

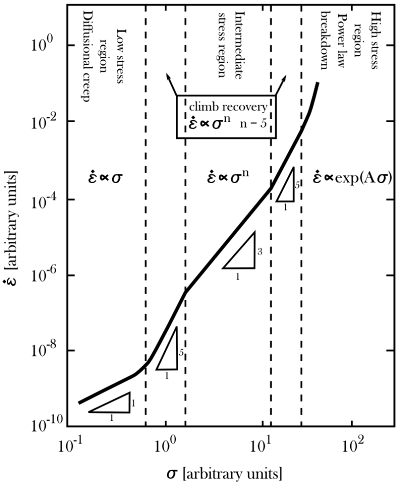

Figure 2.30: Schematic representation of stress dependence of creep rate showing Class M → Class A → Class M transition [16]

The average spacing of free dislocations seems to depend on the value of $\sigma - \sigma_{or}$. A γ' hardened stainless steel, which exhibits A class behaviour due to its weak tendency of cell formation, shows that dislocation density ρ is indirectly proportional to the value of the Orowan stress σ_{or}. The applied stress is balanced by the internal stress that is a sum of stress governed by dislocation strengthening σ_ρ and precipitation - Orowan strengthening σ_{or}. The relation between the dislocation density and stress can be express as

$$\rho_i^{-0.5} = \frac{k_\rho \cdot G \cdot B}{\sigma - \sigma_{or}}, \tag{2.14}$$

where k_ρ is a constant that weakly depends on the material and is equal about 1.

Particle strengthened materials exhibiting M class creep behaviour usually have small subgrain sizes of about 1 μm [15]. Dependence of the size of subgrains on different applied stress levels is depicted in Figure 2.32. There are compared subgrain size values λ of particle strengthened AlCu5NiCo alloy, and single phase AlZn11 and Al99.99 materials. In the double logarithmic plot a clear linear dependence of subgrain size λ on normalized stress $\frac{\sigma}{G}$ is visible. The relation is equal to

$$\lambda = k_\lambda \cdot b \cdot \frac{G}{\sigma} \tag{2.15}$$

where the value of k_λ depends on the material. It was reported to be 28 for AlZn, and 14 for Incoloy 800H [15].

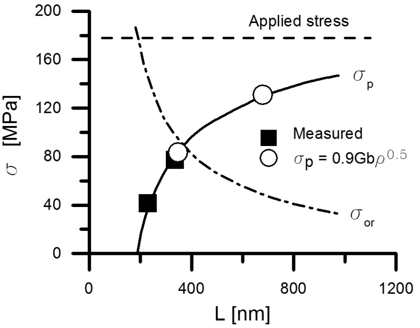

Figure 2.31: The sum of the Orowan stress in the γ'-strengthened stainless steel A-286 and the stress σ_{or} available for dislocation generation equals to the applied stress and varies with interparticle distance L

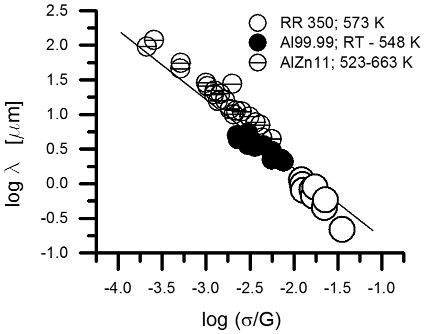

Figure 2.32: Stress dependence of the steady state subgrain size λ of Θ'-strengthened AlCu5NiCo (RR350), and of single phase AlZn and pure Al

2.2.3 Coarsening of subgrains

State of the art 9-12 wt% Cr steels that are used in the tempered martensitic state exhibit intense subgrain coarsening. Those subgrains are not formed during creep exposure as discussed hereinabove, but have their origin in the original lath martensitic structure. The original structure of tempered martensite, having high dislocation density (Figure 2.33a), recovers to relatively coarse subgrain structures (Figure 2.33b) during isothermal annealing at 650 °C. The recovery process accelerates with the increase of temperature (Figure 2.34). Three different mechanisms acting in recovery of subgrains were identified: namely pure static recovery, strain induced recovery, and strain-assisted static recovery (Figure 2.35) [17].

2.2.4 Influence of precipitation on creep

Theoretically, the precipitation after thermomechanical treatment of a material should be stable and should not alter during a creep exposure. This pre-requesite is not fulfilled commonly, because precipitation during creep, overprecipitation and/or coarsening of precipitates is observed in technical materials.

Microstructural development of P91 steel is used as an example of the influence of microstructural development, formation and coarsening of Laves phase particles, and carbides overprecipitation on creep rupture strength as given in Figure 2.36.

Precipitation reactions during creep exposure can have both, positive and negative effects. An example of negative overprecipitation effect during creep is transformation of finely distributed MX nitrides to coarse Z-phase particles in 12 wt. % Cr steels as is observed in P122, NF12

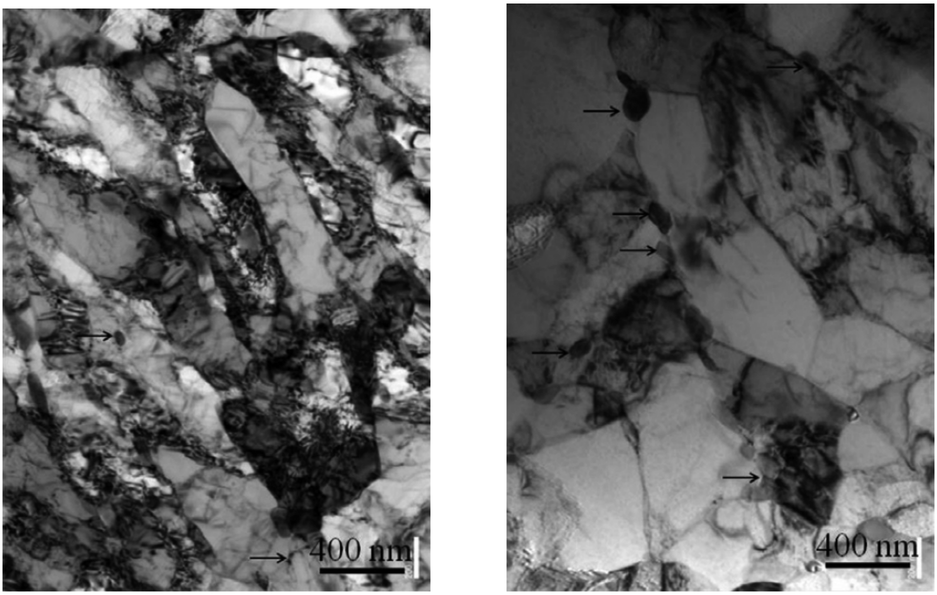

(a)

(b)

Figure 2.33: Typical TEM images of Gr. 91A steel aged at 650 °C for (a) 41, and (b) 23,000h. Arrows indicate precipitates [17]

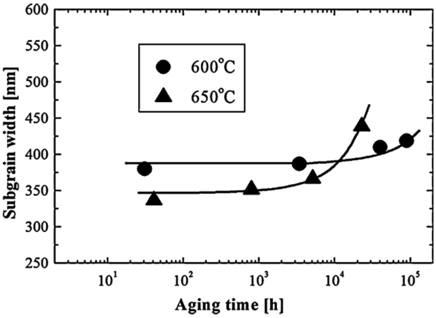

Figure 2.34: Coarsening of subgrains during aging at 600, and 650 °C [18]

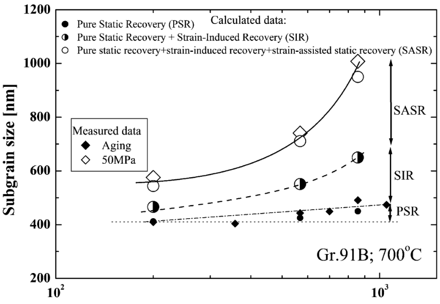

Figure 2.35: Subgrain coarsening of Gr. 91 steel due to three types of recovery mechanisms during long-term creep at 700 °C and 50 MPa [17]

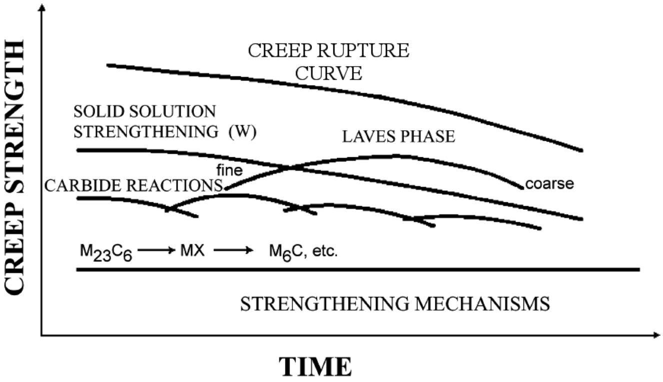

Figure 2.36: Microstructure development during creep exposure of P91 steel and its influence on creep strength [19]

steels [20, 44]. The overprecipitation reaction is depicted in Figure 2.38 schematically. NF12 steel exhibits significantly higher creep strength compared to P92 steel at 650 °C and high stress level; there is steep decrease of creep strength after circa 3,000 h and creep strength of NF12 after 10,000 h at 650 °C is already below P92 steel Figure 2.37.
Abe [21] studied the influence of tungsten addition to 9 wt. % Cr steels on their creep properties. Significant increase of creep strength by addition of 4 wt. % W was observed (Figure 2.39). W addition provoked formation of fine Fe_2W Laves phase particles. The Laves phase particles were not present in the experimental material from the beginning of creep testing but they precipitated during creep exposure. The precipitation of fine Fe_2W Laves phase particles caused nonlinearity in creep rate curves during primary stage and the effect increased with increased W alloying (Figure 2.40).

2.2.5 Creep modeling

Creep modeling can be roughly divided into ***physical*** and ***statistical*** based modeling. The ***physical based models*** express influence of material characteristics and features, like density of dislocation, grain orientation, stacking fault energy, grain and subgrain size etc., on creep properties [32]. Such modeling, on the other side, requires detailed understanding of physical mechanisms acting during creep process. Thus, physical based models can be successfully used mostly for pure metals and simple alloys only but ***statistical based models*** are mostly used for description of technical relevant materials. Statistical based modeling requires significant amount of experiments but, in contrary to physical based modeling, proper understanding of all the active mechanisms that influence creep processes is not necessary. Statistical based modeling is commonly used for finite element modeling as well [11].
Bina at all [45] developed a relatively simple creep deformation model. The model was developed for description of low alloyed creep resistant steels and is given as

$$\epsilon_i(t) = \epsilon_{inst} \cdot \left[\frac{\epsilon_{rup}}{\epsilon_{inst}} \right]^{h(x_t)} \tag{2.16}$$

where $\epsilon_i(t)$ is total deformation in time t_i,
ϵ_{inst} is instantaneous deformation after loading,
ϵ_{rup} is rupture deformation,
$h(x_t)$ is a degradation function.

The degradation function $h(x_t)$ describes complex creep behaviour of hardening and softening processes. The degradation function of the original model [45] is given as a product of two functions:

$$h(x_t) = x^{a_1} \cdot \left[\frac{1 + exp(-2 \cdot x_t^{a_2})}{1 + exp(-2)} \right]^{a_3} \tag{2.17}$$

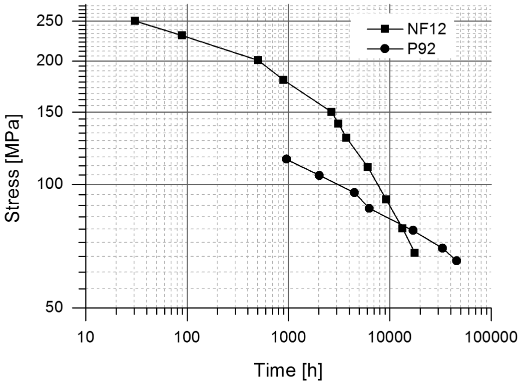

Figure 2.37: Creep strength of P92 and NF12 steel at 650 °C [20]

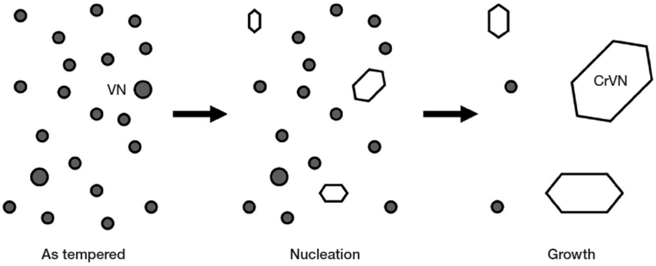

Figure 2.38: Transformation of finely distributed VN to coarse Z phase particles [20]

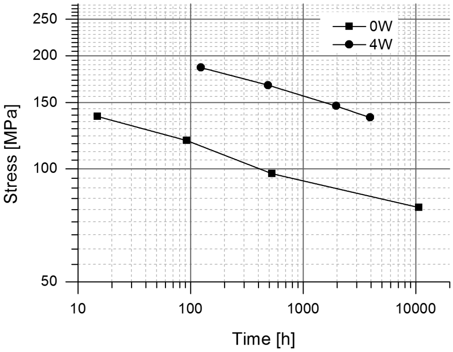

Figure 2.39: Influence of W addition on creep strength of 9 wt. % Cr steel [21]

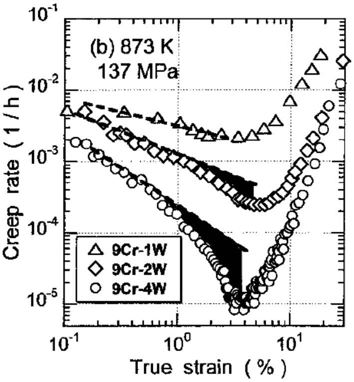

Figure 2.40: Influence of W addition on creep rate curves of 9 wt. % Cr steel [21]

$$x_t = \frac{t_i}{t_r} \tag{2.18}$$

where a_1 ... a_3 are regression coefficients,
t_r is time to rupture.

A hardening function x^{a_1} is effective mainly in the primary and partially in the secondary stage of creep. A softening function $\left[\frac{1+exp(-2\cdot x_t^{a_2})}{1+exp(-2)}\right]^{a_3}$ is effective in secondary and tertiary stage of creep where the secondary stage of creep is controlled by the constant a_3 and the regression coefficient a_2 controls the tertiary stage of creep.

The Equation 2.17 after double logarithmization is possible to write as

$$ln\left(ln\frac{\epsilon_{i(t)}}{\epsilon_{inst}}\right) - ln\left(ln\frac{\epsilon_{rup}}{\epsilon_{inst}}\right) = a_1 \cdot ln(x_t) + a_3 \cdot \left[\frac{1+exp(-2\cdot x_t^{a_2})}{1+exp(-2)}\right] \tag{2.19}$$

The left side of Equation 2.19 represent a normalized deformation, and x_t a normalized time. An example of Equation 2.19 application on creep deformation data of low alloyed 1Cr08Mo025V steel is given in Figure 2.41.

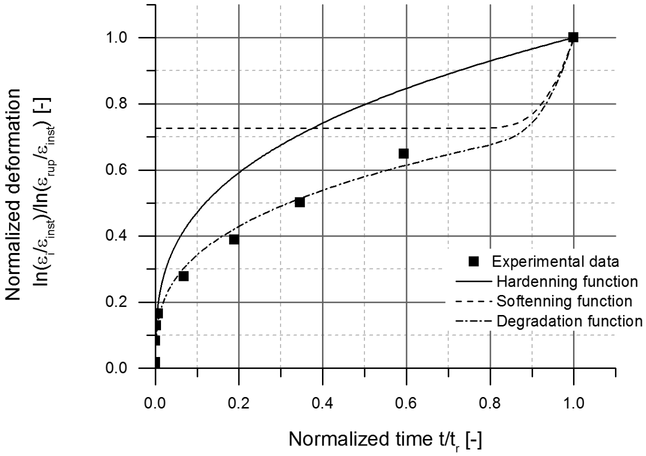

Figure 2.41: Normalized creep deformation data of 1Cr05Mo025V steel tested at 500 °C and 177 MPa

2.3 Creep testing

Creep testing includes variety of techniques. A comprehensive overview can be found in [46]. From the broad variety of techniques, ***uniaxial creep testing*** in continuous and discontinuous form will be discussed.

2.3.1 Uniaxial creep testing

The most common way how to determine creep properties of metals and alloys is based on ***uniaxial creep testing***. A sketch of such machine is given in Figure 2.42, but there can be found many modifications, e.g., using double or no lever loading system, top or bottom loading and so on. The testing procedure of the constant load creep test is specified in an European standard EN ISO 204:2009 [47].

Commonly, deformation during the constant load creep test is measured by extensometers where rods are directly attached to specimen [46]. Interrupted measurement is used mostly in multi-specimen machines. Such machines are practically the same as is depicted in Figure 2.42, just specimens are there in chain, and furnace is longer adequately. Deformation during interrupted type of creep testing is measured on a sample at room temperature. Such method is able to produce lot of experimental data, although the quality of temperature control because of the longer furnace, and quality of the obtained creep strain curve can be slightly worse compared to continuous test.

Influence of interrupted testing was studied by Granacher at all [48]. They have shown that the influence of interruptions is negligible and within a scatter band.

Examples of creep curves were shown in the section 2.2, and examples of stochastical modeling of time to rupture and creep deformation have been shown in the subsection 2.2.5.

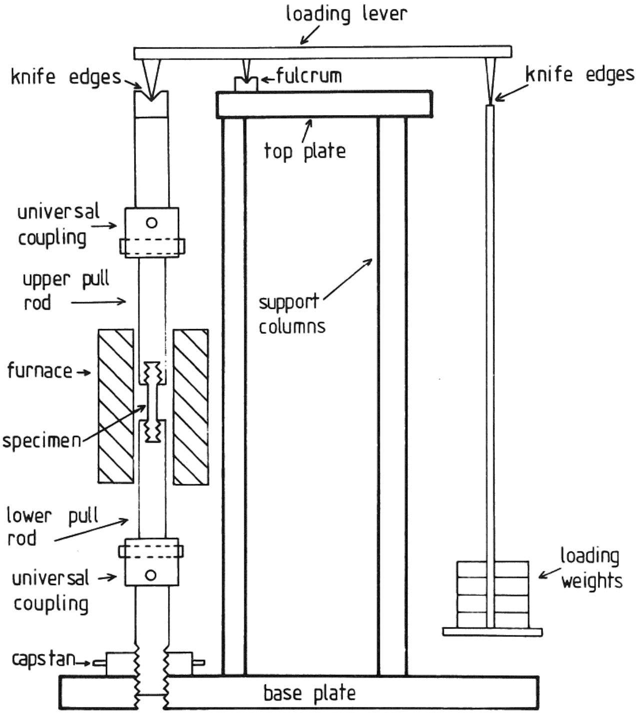

Figure 2.42: Sketch of a uniaxial top-lever creep machine [22]

Chapter 3

Experimental methods

3.1 Material

The chemical composition of an experimetal alloy batch 2.5W05Nb0Ti, prepared in course of the development of Crofer®22H [27], was used as the starting point for further alloy optimization. The amount of Cr was reduced from 23 wt% down to 17.5 wt% in order to reduce formation of the undesirable σ phase in the application temperature range 600–650 °C. The impact of rolling parameters on resistance against creep, and precipitate evolution was studied using batch 17Cr1.

Batches 17Cr2, and 17Cr3 represent further development steps toward more creep resistant steel for application at 600–650 °C. The amount of W was increased from 2.5 up to 3 wt% in batch 17Cr2, while the content of W and Nb was increased in batch 17Cr3 (Table 3.1).

The 16 kg melt of the 17Cr1 batch was prepared and rolled at the Institute of Ferrous Metallurgy, RWTH Aachen. The casted block was divided into 3 parts, forged and finally rolled. In order to evaluate the influence of initial rolling state on the mechanical properties, the three blocks were rolled using different parameters.

The 17Cr2, and 17Cr3 batches were arc-melted and drop-casted at the Oak Ridge National Laboratory. The 750 g ingots were rolled from thickness of 25 mm down to 7.6 mm. The rolling

Table 3.1: Chemical compositions of the experimental alloys (in wt%)

Code	C	S	N	Cr	Mn	Si	Nb	W	O	Fe
2.5W05Nb0Ti	0.0040	0.0027	0.008	22.95	0.46	0.2	0.57	2.50	0.006	R
17Cr1	0.0021	<0.001	<0.001	17.4	0.475	0.24	0.57	2.41	0.03	R
17Cr2	0.002	0.0028	0.0076	16.97	0.46	0.22	0.5	2.97		R
17Cr3	0.002	0.0026	0.0112	16.99	0.46	0.31	0.91	2.93		R

Table 3.2: Interpass annealing temperature and deformation of the last rolling step

Code	Deformation [%]	Teperature [°C]
17Cr1_1	7	1,000
17Cr1_2	10	920
17Cr1_3	25	875
17Cr2	15+11	1,100
17Cr3	15+11	1,100

parameters of a last step are given in the Table 3.2.

3.2 Annealing experiments

Cubes of 4–5 mm lateral length were machined from sheets for annealing experiments. Those specimens that were annealed above 1,000 °C were encapsulated in silica glass capsules to prevent oxidation. The samples were annealed in horizontal muffle furnaces. Hot rolled specimens were observed perpendicular to the rolling direction. The annealing temperature was controlled by type S thermocouples.

3.3 Metallography analysis

Polished specimens were mounted in epoxy resin, grinded and polished by a standard metallographic way of preparation. The final polishing step was polishing in a Vibromet for 5 hours.

3.3.1 Optical microscopy

Grain structures were observed using a Zeiss metallographic microscope. Polished specimens were electrrolytically etched in a 5vol% water solution of H_2SO_4 using a voltage of 1.5 V.

3.3.2 Scanning electron microscopy

Size and distribution of Laves phase particles were studied using a Zeiss Merlin and Zeiss Supra 500 VP scanning electron microscope. To enhance the laves phase particles - matrix contrast, polished specimens were electrolytically etched in a 5vol% water solution of H_2SO_4 using a voltage of 1.5 V for 3 to 5 seconds.

3.3.3 Image analysis

Image analysis of the obtained micrographs was performed in a commercial software analySIS®pro ver. 5. Size distributions of Laves phase particles were evaluated by the Weibull distribution.

3.4 Mechanical testing

3.4.1 Tensile testing

All the tensile tests were performed according to the standard ISO 6892:2011 [49]. Displacement was recorded by a pair of electronic extensometers. A standard muffle oven was used for experiments at elevated temperatures. Specimens were heated for 1 hour at elevated temperature prior to a tensile test. Standard tensile specimens with a gauge diameter of 6.4 mm and gauge length of 30 mm were used (Figure 3.1).

3.4.2 Tensile creep experiments

Tensile creep tests in air and under constant load were carried out at the 17Cr1 batch. Experiments with expexted lifetime below 5,000 h were executed in single specimen creep machines. Experiments with expected lifetimes exceeding 5,000 h were initialy tested in single specimen machines and after reaching of regime, when increase of creep deformation was very slow, were transfered to multispecimen test rigs.

The development of creep deformation was measured continuously by a pair of electronic extensometers. Specimen tested in multispecimen creep machines were tested in so called ***interupted testing*** (cf. subsection 2.3.1). Creep deformation was measured opticaly during interuptions at ambient temperature.

Temperature was controlled by three type S thermocouples placed on the gauge sections of the specimen in case of testing in the single specimen machines. 5 zone furnaces were used for multispecimen testing with a type S thermocouples located in the middle of each zone in close vicinity of the specimens. Cylindrical specimens with gauge diameters of 6.4 mm and gauge length of 30 mm were used (Figure 3.1). Specimens were taken perpendicular to the rolling direction.

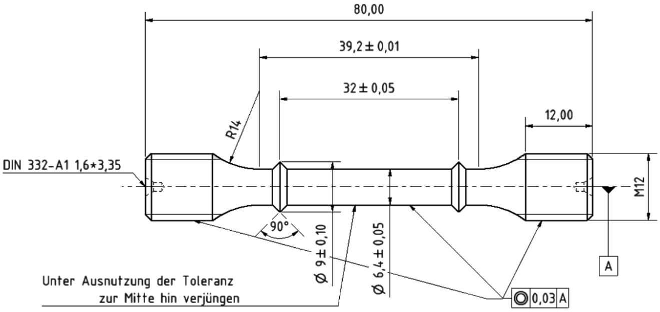

Figure 3.1: Sketch of a tensile specimen

Chapter 4

Results

4.1 Alloy design

The design of the Laves phase strengthened fully ferritic steels is based on the experience from the development of Crofer®22H [27]. ThermoCalc calculations were carried out for a reference steel featuring a chemical composition of (in wt%) 17 Cr, 2.5 W, 0.5 Mn, 0.5 Nb, 0.2Si to evaluate the influence of W, Nb, and Si on formation of Laves, and Sigma phase. The main task of the modeling was to suggest a composition, in which:

1. the (Fe,Cr) σ - phase is restricted to temperatures below 600 °C,
2. the Laves phase is restricted to temperatures below 1,100 °C, and
3. the Laves phase content will have its maximum at 650 °C

4.1.1 Influence of W, Nb, and Si on microstructure

Influence of W content

W is commonly used in the design of creep resistant steel as a solid solution strengthener. W is also reported as a strong Laves phase forming element, enhancing stability of precipitates by decreasing the self-diffusion rate in the iron matrix. Figure 4.1 displays the phase fields of the reference composition as a function of W content. Increasing W content slightly shifts the stability of the $(Fe,Cr,Si)_2(W,Nb)$ Laves phase (marked as Laves#1 in the diagram) to sligthly higher temperatures slightly. The same is also valid about the influence of the W on the stability of the (Fe,Cr) σ-phase. The phase field of the $(Fe, Cr,Si)_2(Nb,W)$ Laves phase (marked as Laves#2 in the diagram) increases steadily up to 1.7 wt % W with the predicted stability up to 720 °C. By further increase of the W content the Laves phase region decreases to lower molar content.

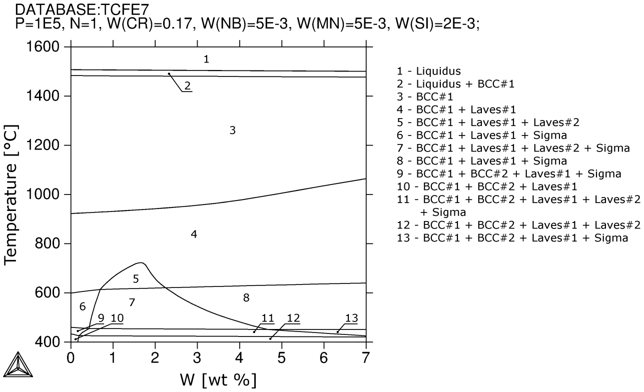

Figure 4.1: Phase fields as a function of W, nominal composition in wt% 17Cr, 0.5Nb, 0.5Mn, 0.2Si, XW (ThermoCalc calculations utilizing TCFE7)

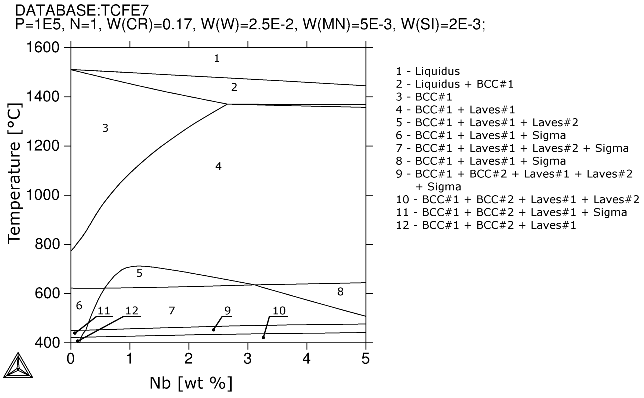

Figure 4.2: Phase fields as a function of Nb, nominal composition in wt% 17Cr, 2.5W, 0.5Mn, 0.2Si, XNb (ThermoCalc calculations utilizing TCFE7)

Influence of Nb content

The role of Nb in a Laves phase strengthened ferritic steel is to enhance solid solution strengthening [50] and to stimulate precipitation of Laves phase particles [27]. Nb has a positive effect on the stability of the $(Fe,Cr,Si)_2(W,Nb)$ Laves phase. ThermoCalc calculations (utilizing the TCFE7 database) predict a uniform increase of dissolution temperature up to 2.65 wt% (Figure 4.2). The influence of Nb on the stability of the $(Fe,Cr,Si)_2(Nb,W)$ Laves phase is comparable to W. The highest predicted temperature is at 731 °C and 1 wt%. There is almost no influence of Nb on the stability of the (Fe, Cr) σ - phase.

Influence of Si content

Si is used in most steels as a desoxidation agent [51]. Increased Si content stabilizes the (Fe, Cr) σ-phase, and the $(Fe,Cr,Si)_2(W,Nb)$ Laves phase at higher temperatures slightly, but it boosts the formation of the $(Fe,Cr,Si)_2(Nb,W)$ Laves phase. The dissolution temperature of the $(Fe,Cr,Si)_2(Nb,W)$ Laves phase increases steeply from 400 °C at 0.015 wt% up to 810 °C at 0.6 wt%. The dissolution temperature of Laves#2 continuously increases with further increased Si content above 0.6 wt%.

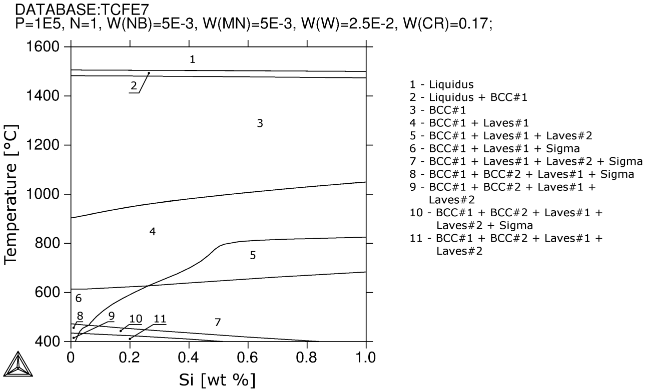

Figure 4.3: Phase fields as a function of Si, nominal composition in wt% 17Cr, 2.5W, 0.5Nb, 0.5Mn, XSi (ThermoCalc calculations utilizing TCFE7)

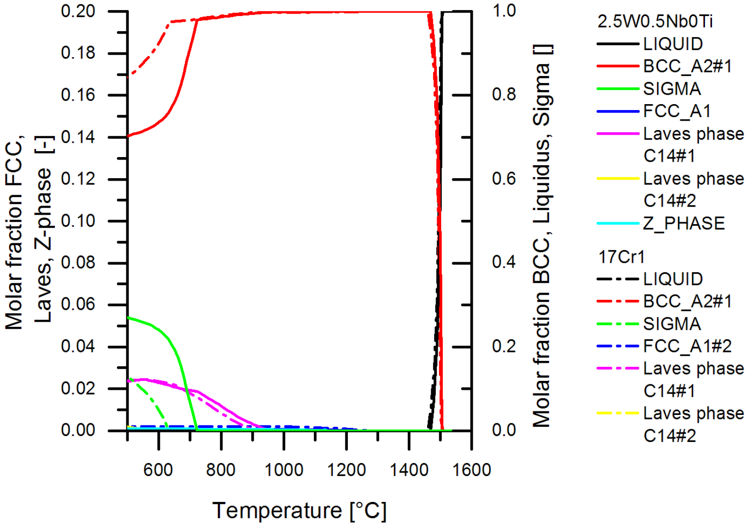

Figure 4.4: Phase diagram of the 2.5W0.57Nb0Ti, and 17Cr1 steel (ThermoCalc calculations utilizing TCFE7)

4.1.2 Design of the experimental steels

Alloy 17Cr1

The primary goals of the 17Cr1 material were to confirm the absence of the (Fe, Cr) σ-phase, and to optimize the rolling parameters for favourable precipitation kinetics. ThermoCalc calculations (utilizing TCFE7 database) are depicted in Figure 4.4. The chemical composition applied in the calculations is given in Table 4.1.

The positive influence of reduced Cr content in high chromium steels strengthened by Laves phase particles was reported in [27]. The predicted (Fe, Cr) σ - phase solution temperature shifts from 720 °C in 2.5W057Nb0Ti steel down to 632 °C in 17Cr1 steel (green curves in Figure 4.4) because of the reduction in chromium content from 23 to 17.5 wt%. The molar fraction of the high temperature (Fe,Cr,Si)$_2$(Nb,W) Laves phase is almost identical in both steels (magenta curves in the Figure 4.4).

Table 4.1: Chemical compositions of the experimental alloys (in wt%)

Name	C	S	N	Cr	Mn	Si	Nb	W	O	Fe
2.5W0.57Nb0Ti	0.0040		0.008	22.95	0.46	0.2	0.57	2.50		R
17Cr1	0.0021	<0.001	<0.001	17.4	0.475	0.24	0.57	2.41	0.03	R
17Cr2	0.002	0.0028	0.0076	16.97	0.46	0.22	0.5	2.97	-	R
17Cr3	0.002	0.0026	0.0112	16.99	0.46	0.31	0.91	2.93	-	R

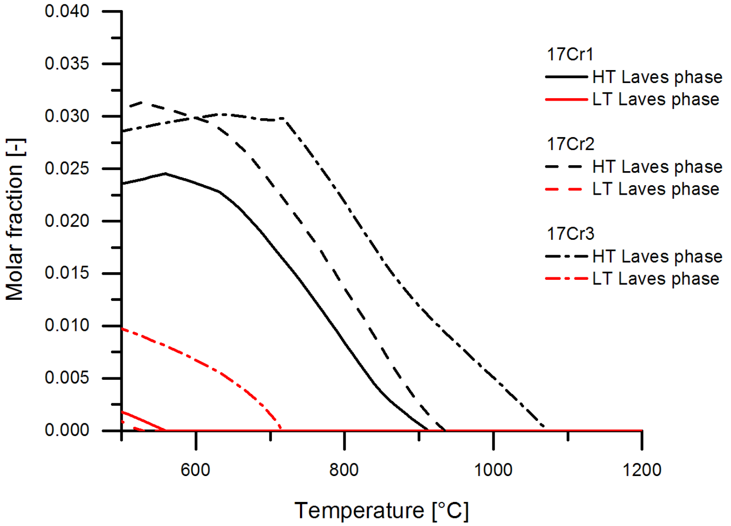

Figure 4.5: Stability regions of the High Temperature $(Fe,Cr,Si)_2(Nb,W)$, and Low Temperature $(Fe,Cr,Si)_2(Nb,W)$ Laves phase (ThermoCalc calculations utilizing TCFE7)

Alloy 17Cr2 and 17Cr3

The 17Cr2 and 17Cr3 steels were used to evaluate the influence of W and Nb on precipitation. The influence of particular elements on precipitation of the LT, and HT Laves phase was discussed in section 4.1.1. The calculated contents of the HT Laves phase in the 17Cr_1 steel is 2.35 and 2.2 mol% at 600 and 650 °C, respectively; (c.f. section 4.5).

Increasing the W from 2.4 to 3 wt% in steel 17Cr2 causes an increase in the content of the HT phase from 2.35 up to 3 mol% at 600 °C, and from 2.2 up to 2.8 % at 650 °C. An additional increase in Nb content from 0.5 up to 0.9 wt% in 17Cr3 steel, increases the stability of the HT region to higher temperatures. The predicted content of the HT Laves phase is more or less constant from 570 up to 715 °C at 3 mol%. The dissolution temperatures vary with chemical composition, too. The HT Laves phase is predicted to be stable up to 912 °C in the 17Cr_1 steel. Increasing the W content (17Cr2) steel has almost no influence on the stability of the HT Laves phase. It is supposed to dissolve at around 930 °C. In 17Cr3 steel, increasing in Nb content causes a significant shift of the dissolution temperature up to 1066 °C.

The increase in Nb content does not only cause a shift of the HT Laves phase but of the LT Laves phase to higher temperatures, too. The LT Laves phase of the 17Cr1, and 17Cr2 materials is predicted to be stable up to less 600 °C, but an increase in Nb from 0.5 up to 0.9 wt% causes a shift of the dissolution temperature of the LT Laves phase to temperatures around 700 °C.

4.2 Initial microstructure and properties

Light micrographs of the initial macrostructure of 17Cr1 steel in all the 3 rolling variants (rolling conditions are given in Table 3.2), and 17Cr2 and 17Cr3 steels are depicted in Figure 5.7. SEM micrographs of all the experimental materials in as recieved state are depicted in Figure 4.8. The grain structure of the 17Cr1_1 sample (Figure 4.6a) is significantly coarser than that of the 17Cr1_2 variant (Figure 4.6b) with equiaxial grain structure and without pronouned deformation in the rolling direction. Coarse, highly deformed grains were observed in the 17Cr1_3 sample (Figure 4.6c). The dark etch pits in the micrographs of the 17Cr1 materials are (Cr, Mn) oxide clusters resulting from contamination of the melt by oxygen during vacuum melting. Grain structure of rolled 17Cr1 specimens in all the three rolling directions is presented in Figure 4.7. There was observed no significant anisotropy of grain structure in 17Cr1_1 and 17Cr1_2 specimens but severe elongation of grains in rolling direction in 17Cr1_3 sample was presented. No significant deformation of grains and their refinement compared to 17Cr1_2 sample was observed in 17Cr2 and 17Cr3 samples (Figure 4.6d and Figure 4.6e, respectively).

The subgrain structure is well defined in all 17Cr1 variants (Figure 4.8). The grain boundaries of the 17Cr1_1 material are decorated by Laves phase particles (Figure 4.8a). Only a few precipitates were observed at the grain boundaries of the 17Cr1_2 material (Figure 4.8b), and none in the 17Cr1_3 material (Figure 4.8c). These primary particles are likely to be formed during the last rolling step. Rolling temperatures of the 17Cr1_1 material was 1,000 °C, the 17Cr1_2 920 °C, and the last interpass annealing of the 17Cr1_3 material was 870 °C. Few coarse primary particles

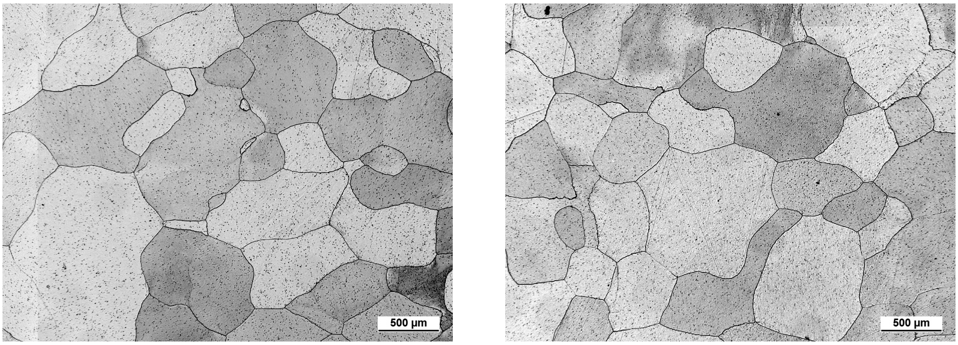

(a) 17Cr1_1 (b) 17Cr1_2

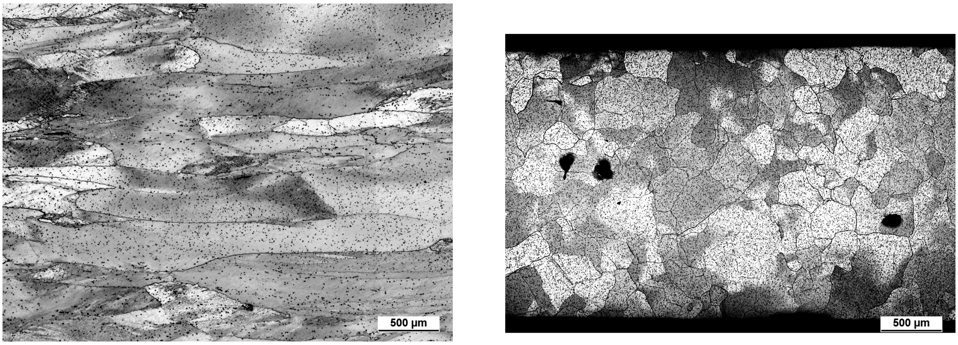

(c) 17Cr1_3 (d) 17Cr2

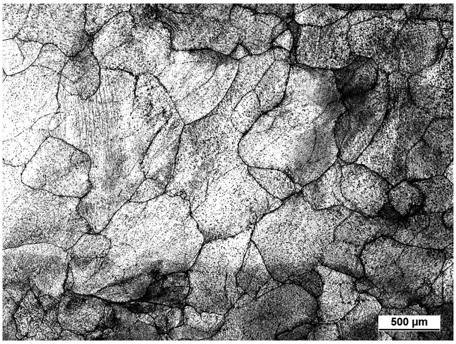

(e) 17Cr3

Figure 4.6: Light optical micrographs of rolled 17Cr1, 17Cr2, and 17Cr3 steels

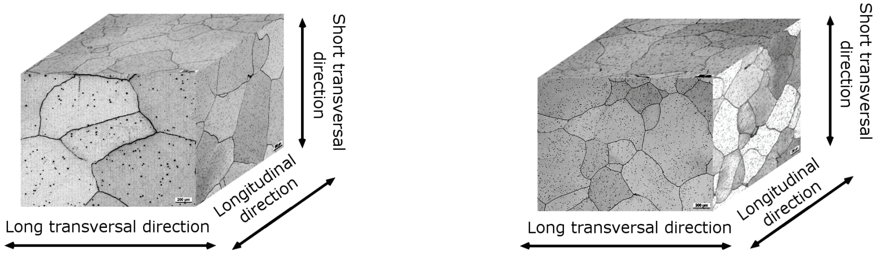

(a) 17Cr1_1

(b) 17Cr1_2

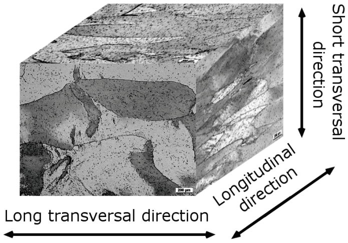

(c) 17Cr1_3

Figure 4.7: Grain structure of rolled 17Cr1 steel in different rolling directions

were observed in the 17Cr_2 sample (Figure 4.8d). In contrary, Laves phase particles were observed not only on the grain boundaries like in the previous cases, but on subgrain boundaries and in the subgrains in the 17Cr3 material (Figure 4.8e).

Tensile test curves of the 17Cr1 materials are presented in Figure 4.9 and the overview results in Figure 4.10. The tests were performed at room temperature, 550, and 650 °C, in case of the 17Cr1_1 and 17Cr1_2 materials. The 17Cr1_3 variant was tested at 600 °C only. At room temperature and 650 °C , the 17Cr1_2 material exhibited a slightly higher strength and plasticity compared to the 17Cr1_1 variant. Tensile curves of the 17Cr1_1 and 17Cr1_2 materials were almost identical at 550 °C. At tested temperatures, the 17Cr1_1 material exhibited the highest elasticity (Figure 4.10c) and plasticity (Figure 4.10d) .

The 17Cr1_3 material exhibited tensile deformation behaviour with low ductility even at 600 °C. Such property was caused by overpronounced deformation in the last rolling step was (25 %) and comparably low rolling temperature (870 °C). As mentioned, the only tensile test of 17Cr1_3 material there was performed at 600 °C. The measured deformation at Rm ϵ_p was 2 % (Figure 4.10d) and the total ductility δ was bellow 5 % Figure 4.9.

4.3 Recrystallization annealing

A series of recrystallization annealing experiments was performed to evaluate the influence of stored dislocation energy (induced by cold rolling) on the recrystallization properties of 17Cr1 steel. The experiments were performed from 1,025 °C up to 1,100 °C and holding times from 5 minutes at 1,100 °C up to 1 hour at 1025 °C. The testing matrix is given in Table 4.2.

Table 4.2: Testing matrix of recrystallization annealing experiments

Temperature [°C]	Time [h]						
	00:05	00:10	00:15	00:20	00:30	00:45	01:00
1025					X	X	X
1050			X		X	X	X
1075		X	X	X	X		
1100	X	X	X	X			

The results of the recrystallization annealing experiments of 17Cr1 steel are given in Figure 4.13 (in terms of variation of ASTM grain size number G, [52]). A comparably coarse grain structure was observed in the 17Cr1_1 and 17Cr_2 materials after 30 minutes of annealing at 1025 °C (Figure 4.11a and Figure 4.11c). The grain structure of the 17Cr_3 variant after annealing at 1025 °C for 30 minutes was finer than in the other two variants (Figure 4.11e). A bimodal grain structure was observed in the 17Cr1_1 and 17Cr_2 materials after annealing at 1050 °C for 15 minutes (Figure 4.11b and Figure 4.11d, respectively), while the 17Cr1_3 material was fully recrystallized (Figure 4.11b).

Coarsening of the fully recrystallized grain structure was observed in all the materials during

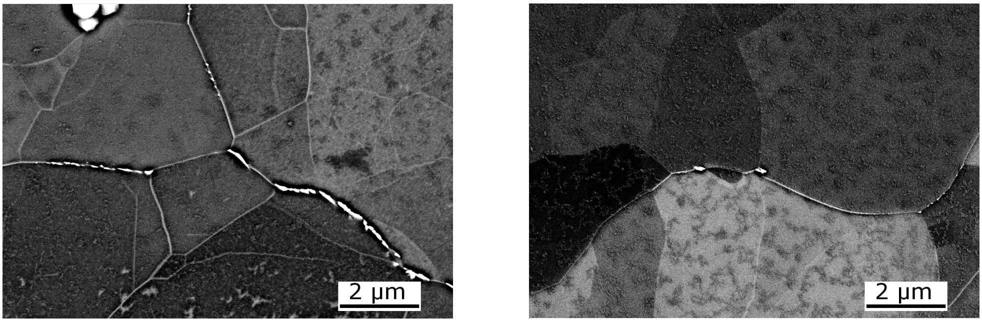

(a) 17Cr1_1　(b) 17Cr1_2

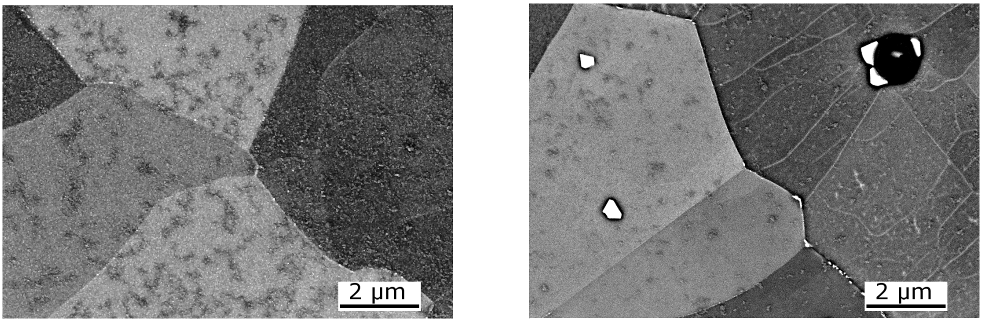

(c) 17Cr1_1　(d) 17Cr1_2

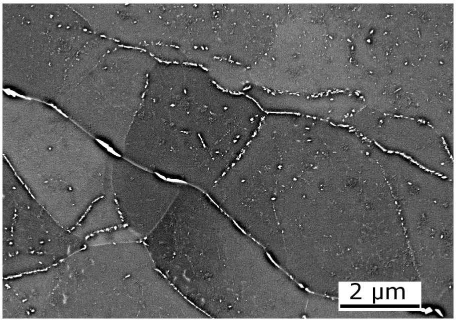

(e) 17Cr1_3

Figure 4.8: SEM micrographs of the 17Cr1 materials in different rolling variants, and 17Cr2 and 17Cr3 materials in as recieved state

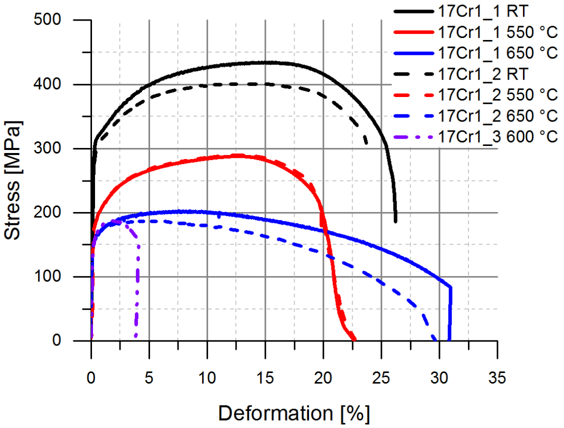

Figure 4.9: Tensile stress-strain curves of 17Cr1 steels at temperatures between ambient temperature and 650 °C

annealing at 1075 and 1100 °C (Figure 4.12, Figure 4.14). Diameter of a grain D is calculated from the corresponding grain size number according to methodic of ASTM as given in [52]

4.4 Influence of thermo-mechanical treatment on precipitation behaviour

Long term annealing experiments of HiperFer steels were performed in different initial thermo-mechanical states. The main goal of these experiments was to evaluate the influence of chemical composition, stored dislocation energy, and already existing precipitate structure on the kinetics of precipitation, size of precipitates and precipitate stability.

4.4.1 Microstructure development during isothermal annealing of samples starting from the as rolled state

Samples were annealed in as rolled state (Table 3.2) at 650 °C for 3, 10, 30, 100, 300, and 1,000 h.

17Cr_1 steel

Representative microstructures of the 17Cr1_1 and 17Cr1_2 materials are displayed in Figure 4.15. The microstructures of the 17Cr1_3 material are presented in Figure 4.16. Enhanced dislocation

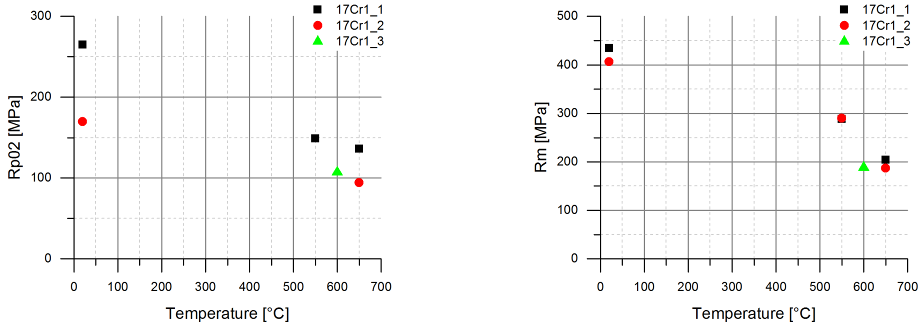

(a) Stress at limit of elasticity

(b) Maximal strength

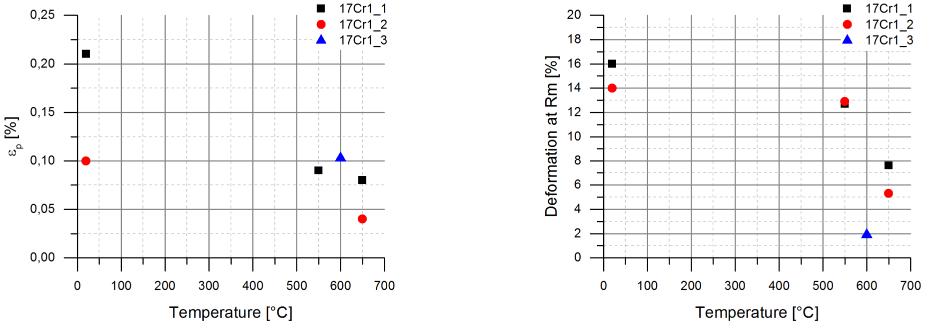

(c) Deformation at limit of elasticity

(d) Deformation at maximal strength

Figure 4.10: Tensile properties of 17Cr1 materials

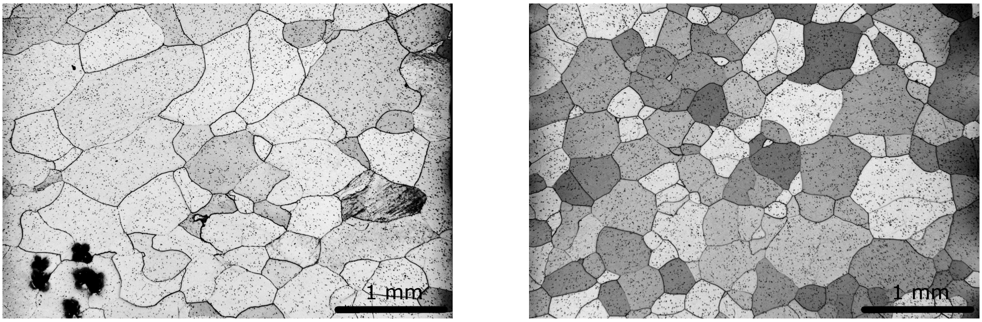

(a) 17Cr1_1, 1025 °C/30 min (b) 17Cr1_1, 1050 °C/30 min

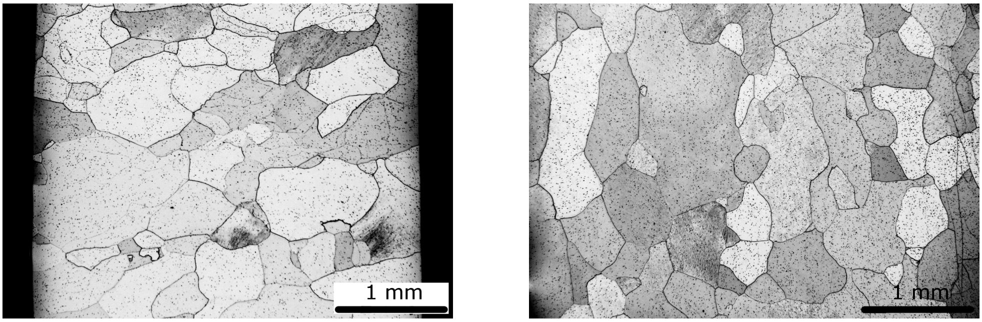

(c) 17Cr1_2, 1025 °C/30 min (d) 17Cr1_2, 1050 °C/30 min

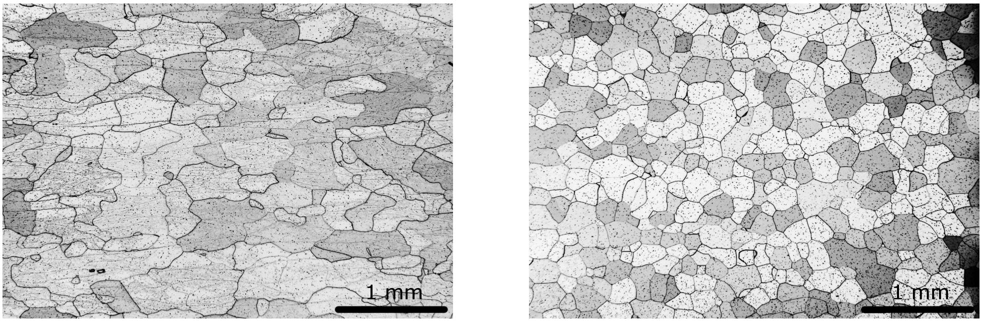

(e) 17Cr1_3, 1025 °C/30 min (f) 17Cr1_3, 1050 °C/30 min

Figure 4.11: Results of recrystallization experiments of the 17Cr1 samples at 1025 °C/30 min and 1050 °C/15 min

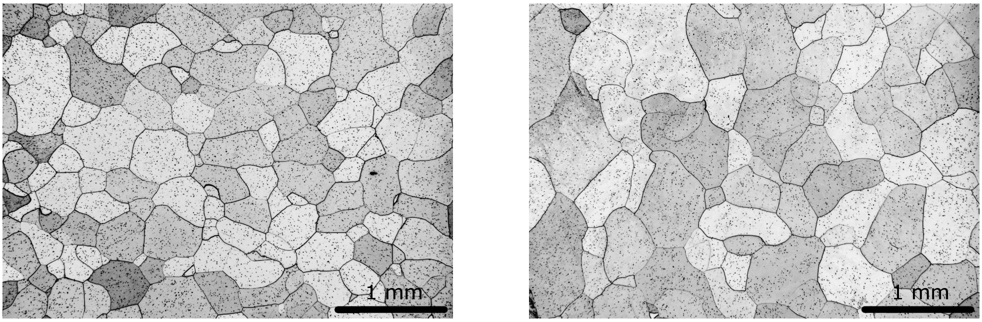

(a) 17Cr1_1, 1075 °C/10 min

(b) 17Cr1_1, 1100 °C/5 min

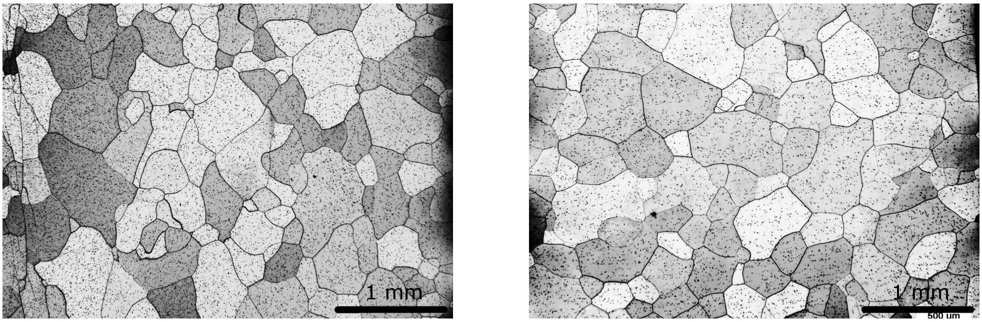

(c) 17Cr1_2, 1075 °C/10 min

(d) 17Cr1_2, 1100 °C/5 min

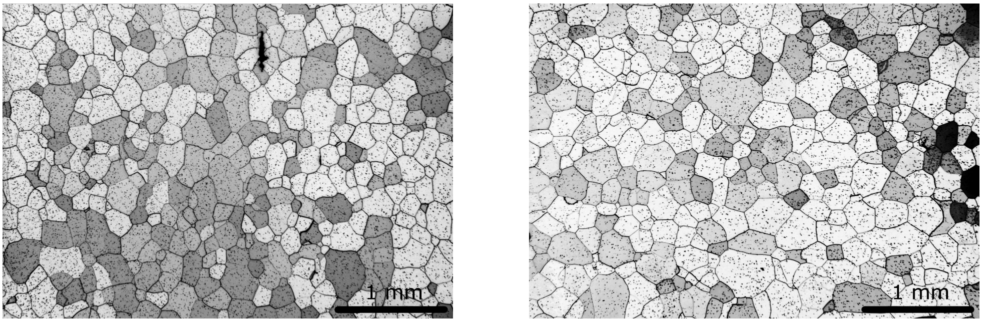

(e) 17Cr1_3, 1075 °C/10 min

(f) 17Cr1_3, 1100 °C/5 min

Figure 4.12: Results of recrystallization experiments of the 17Cr1 samples at 1075 °C/10 min and 1100 °C/5 min

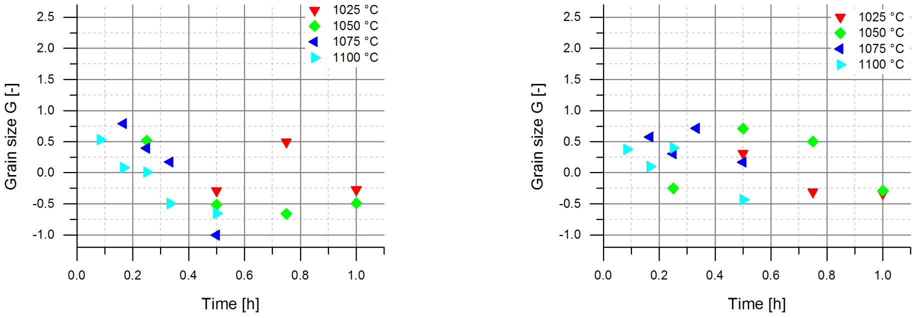

(a) 17Cr1_1

(b) 17Cr1_2

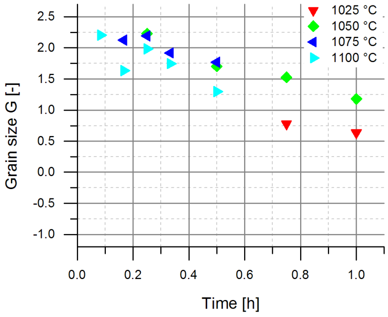

(c) 17Cr1_3

Figure 4.13: Grain size development of 17Cr1 steel during annealing at temperatures 1,025-1,100 °C

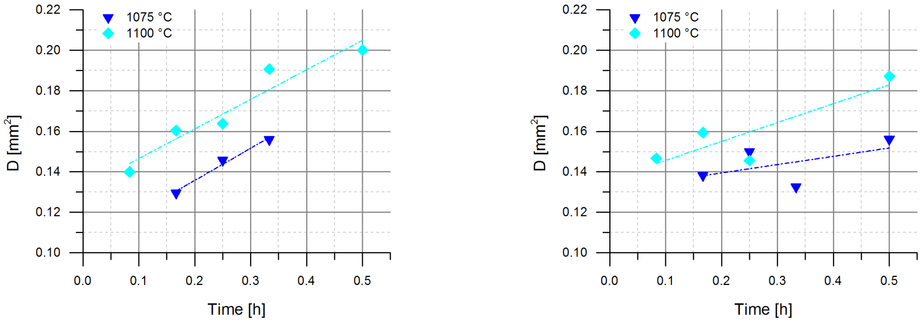

(a) 17Cr1_1 (b) 17Cr1_2

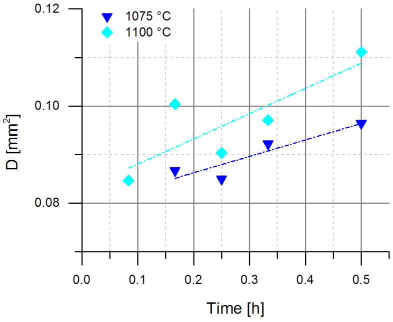

(c) 17Cr1_3

Figure 4.14: Coarsening of grains of 17Cr1 steels at 1075 and 1100 °C

density, resulting from higher deformation during rolling, has a positive influence on the kinetics of Laves phase precipitation (cf. Figure 4.15a, 4.15b, and 4.16a). Laves phase particles start to precipitate on subgrain boundaries. The original subgrain boundary structure is still visible in the 17Cr1_1 and 17Cr1_2 samples after 1,000 h of annealing (Figure 4.15e and 4.15f). In contrary, subgrain structure was hardly observable in the 17Cr1_3 sample after 1,000 h of annealing (Figure 4.16c). No significant coarsening of the Laves phase particles in the 17Cr1_3 material was observed after annealing for 1,000 h at 650 °C (cf.Figure 4.15e, 4.15f, and 4.16c).

No influence of rolling was observed concerning the Equivalent Circular Diameter (ECD) of particles (Figure 4.17). The measured values are quite scattered and mostly fall into the size interval from 50 to 80 nm (the error bars represent the values of ± standard deviation). Furthermore the influence of rolling parameters on the areal fraction of particles was observed (Figure 4.18). The particles areal fraction in the 17Cr1_3 material was between 8 and 10 pct. over 1,000 h of annealing, and growing homogeneously from 4 to 7.5 pct. in case of the 17Cr1_2 material. No systematic influence of time of annealing on areal fraction was observed in case of the 17Cr1_1 samples.

17Cr_2 and 17Cr_3 steels

The microstructural development of the 17Cr2 and 17Cr3 steel is depicted in Figure 4.19. the subgrain structure is decorated by fine Laves phase precipitates after 3 hours of annealing in both the 17Cr2 (Figure 4.19a) and 17Cr3 (Figure 4.19b) materials. High densities of fine particles were observed in the subgrain interiors, and no Particle Free Zones (PFZ) surrounding coarse, primary particles were observed. The subgrain structure was still observed in the 17Cr2 material after annealing for 30 hours (Figure 4.19c), but only its remains were present after 1,000 hours annealing. In the 17Cr3 material, the subgrain structure was not detected after 30 hours of annealing anymore.

In the 17Cr2 and 17Cr3 materials, fine particles with ECD of 36.6±1.6 nm and 37.44±1.5 nm after 3 h of annealing coarsened up to appr. 55 nm after 1,000 h of annealing (Figure 4.20). The areal fraction increased from 4 pct in early stages of precipitation up to 8-10 pct after 1,000 hours of annealing. No influence of enhanced Nb content (17Cr3) on ECD and areal fraction was detected.

4.4.2 Microstructure development during isothermal annealing starting from the recrystallized state

The 17Cr1, 17Cr2, and 17Cr3 materials were annealed after recrystallization (1200 °C for 20 minutes). Annealing samples were encapsulated in vacuum to minimize chemical changes due to surface oxidation during solution annealing. 17Cr1 samples were analyzed by SEM after 3, 10, 100, and 1,000 hours. Samples of 17Cr2 and 17Cr3 steels were analyzed after 30 and 300 hours additionally.

Microstructure development of 17Cr1 and 17Cr2 steels during isothermal annealing at 600 °C is presented in Figure 4.22. Microstructure images of 17Cr3 specimens after 3, 30, and 1,000 hours

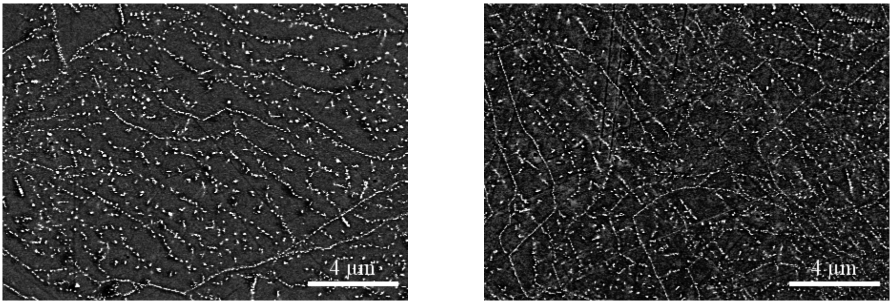

(a) 17Cr1_1, 650 °C/3 h (b) 17Cr1_2, 650 °C/3 h

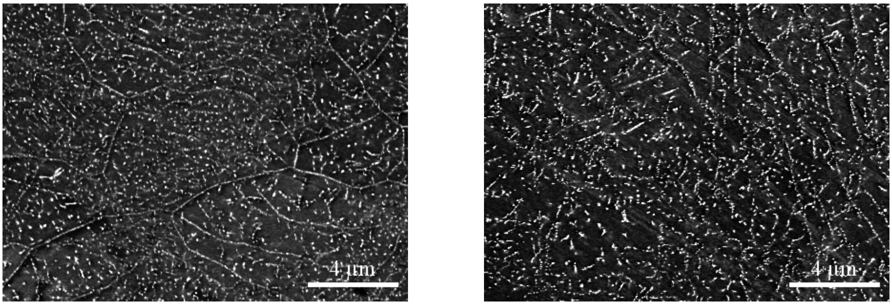

(c) 17Cr1_1, 650 °C/30 h (d) 17Cr1_2, 650 °C/30 h

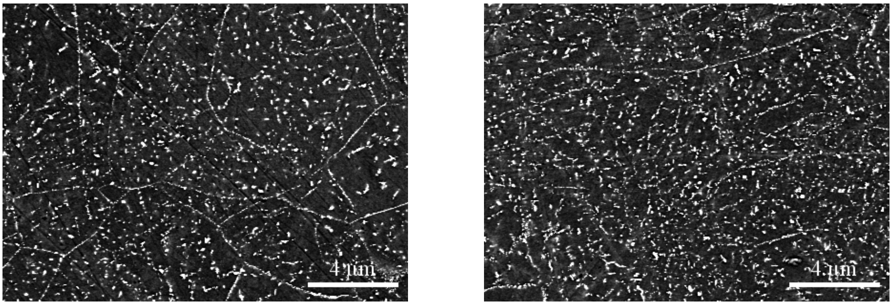

(e) 17Cr1_1, 650 °C/1,000 h (f) 17Cr1_2, 650 °C/1,000 h

Figure 4.15: Microstructure development of the 17Cr1_1 and 17Cr1_2 variant during annealing at 650 °C

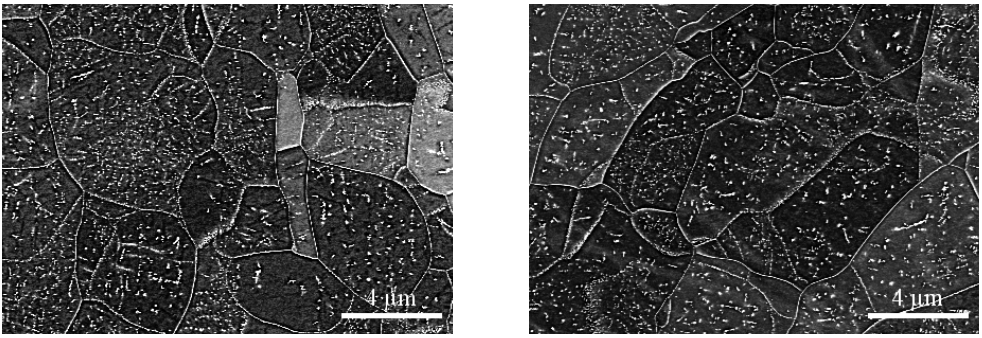

(a) 650 °C/3 h

(b) 650 °C/30 h

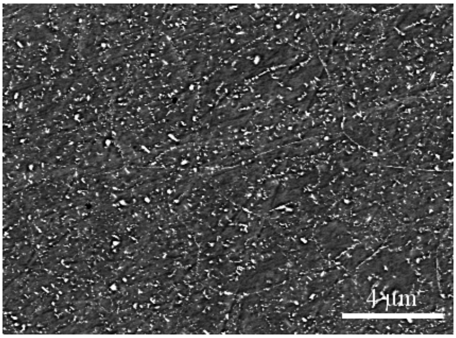

(c) 650 °C/1,000 h

Figure 4.16: Microstructure development of the 17Cr1_3 variant during annealing at 650 °C

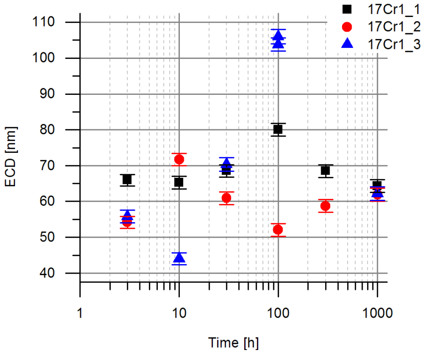

Figure 4.17: Equivalent circular diameter development of rolled 17Cr1 samples during isothermal annealing at 650 °C

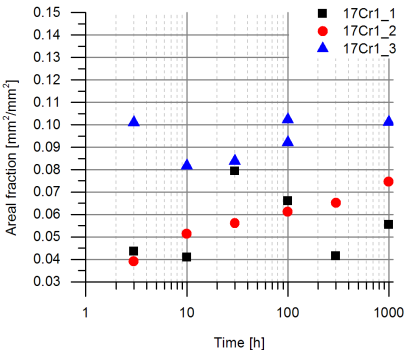

Figure 4.18: Areal fraction development of rolled 17Cr1 samples during isothermal annealing at 650 °C

of annealing are displayed in Figure 4.23. Detailed microstructures of the 17Cr1, 17Cr2, and 17Cr3 specimens after 1,000h are given in Figure 4.26. The majority of particles in 17Cr3 steel (Figure 4.28c) has size in tens of nanometers, but coarse particles were observed, too. This suggests that the 17Cr3 material was either in the coarsening stage already, or that overlapping precipitation appeared.

The increased content of tungsten in 17Cr2 steel compared to 17Cr1 steel had hardly any influence on the size of particles (Figure 4.24), but refinement of particles was observed in 17Cr3 steel, probably resulting from increased niobium content. The development of the particles areal fraction was almost identical for all three steels, increasing from 4-6 pct after 3 hours of annealing up to 8-12 pct after 1,000 hours of annealing (Figure 4.25).

4.4.3 Influence of low temperature tempering on microstructural development at 650 °C

The influence of increased dislocation density induced by cold deformation on microstructure development (presented in the section 2.1.3 by Trotter at all [31]) was demonstrated for the trial steel in subsection 4.4.1. Short term tempering at relatively low temperatures was the second method mentioned in section 2.1.3 how to influence precipitates development. To evaluate the influence of low temperature tempering on precipitation, annealing experiments on fully recrystallized 17Cr1 samples, which were tempered at three different temperatures, were performed. The tempering temperatures were 475 °C (Temp1), 510 °C (Temp2), and 540 °C (Temp3). All samples were tempered for 5 hours. Temp1, Temp2, and Temp3 samples were than annealed at 650 °C for times up to 1,000 hours subsequently.

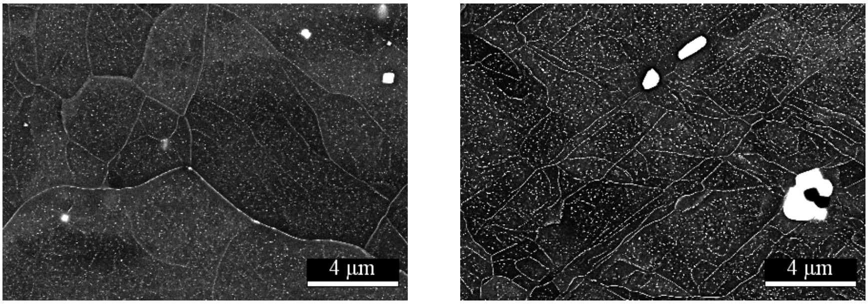

(a) 17Cr2, 650 °C/3 h

(b) 17Cr3, 650 °C/3 h

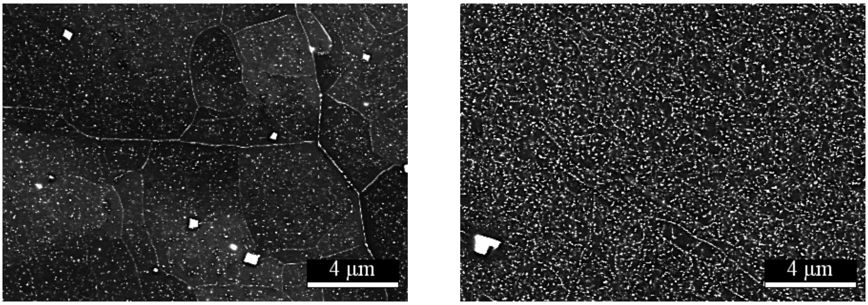

(c) 17Cr2, 650 °C/30 h

(d) 17Cr3, 650 °C/30 h

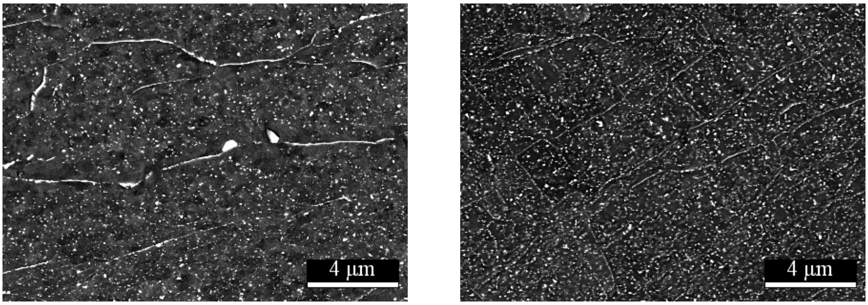

(e) 17Cr2, 650 °C/1,000 h

(f) 17Cr3, 650 °C/1,000 h

Figure 4.19: Microstructure development of 17Cr2and 17Cr3 materials during annealing at 650 °C

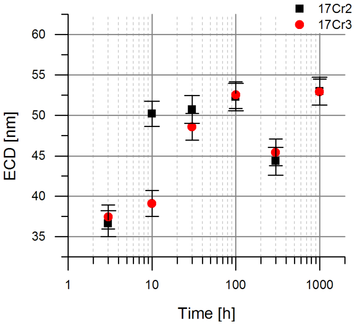

Figure 4.20: Laves phase particles equivalent circular diameter development of rolled 17Cr2 and 17Cr3 samples during isothermal annealing at 650 °C

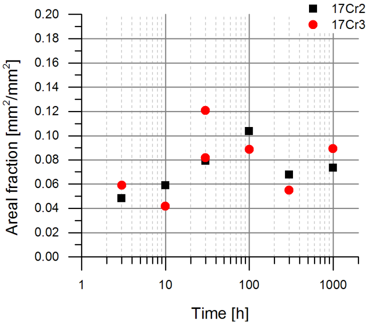

Figure 4.21: Laves phase particles areal fraction development of rolled 17Cr2 and 17Cr3 samples during isothermal annealing at 650 °C

The development of microstructure of the Temp1 and Temp2 specimens during isothermal annealing at 650 °C is presented in Figure 4.27, microstructure development of the Temp3 specimens is depicted in Figure 4.28. Precipitates are homogeneously distributed throughout the grain interior in all the specimens and similar to the 17Cr1 specimens after anneling started from the recrystallized state (cf. Figure 4.22). The evaluated ECD values are quite scattered in case of the Temp3 specimens, nevertheless a systematic trend to slightly coarser particles in the Temp1 specimens in comparison to the Temp2 samples can be observed. On the other hand, particles were usually finer in the Temp3 specimens in comparison to the Temp2 samples (Figure 4.29). Different tempering temperatures have no significant influence on Laves phase areal fraction values (Figure 4.30).

4.4.4 The influence of high temperature tempering on microstructural development at 650 °C

Two sets of experiments were performed to evaluate the influence of the presence of already existing coarse particles on the grain boundaries and in the grain interiors on microstructural development at 650 °C and its effect on the creep performance. The first set of experiments was intended to analyze the role of temperature and time on Laves phase particle formation kinetics at grain boundaries and in the grain interiors. The second set of experiments evaluated the influence of presented Laves phase particles on the precipitation behavior at 650 °C (application temperature).

Short term annealing experiments were performed at recrystallized samples of the 17Cr1 material. The recrystallization annealing was done at 1200 °C for 20 minutes. The short term annealing

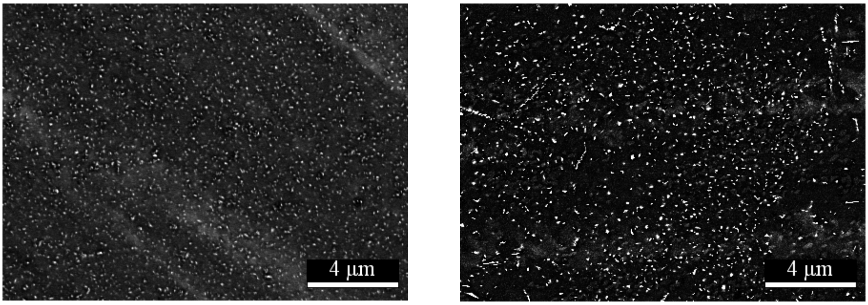

(a) 17Cr1, 650 °C/3 h

(b) 17Cr2, 650 °C/3 h

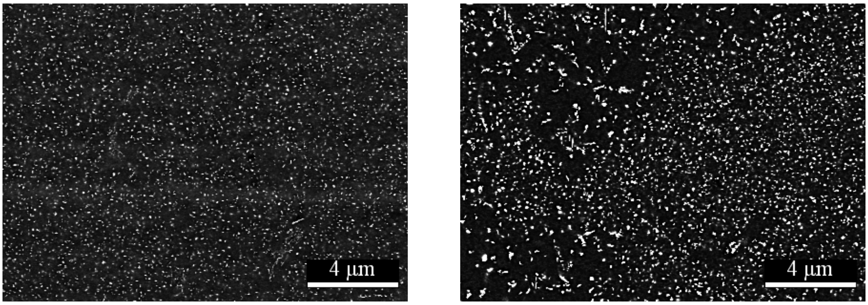

(c) 17Cr1, 650 °C/100 h

(d) 17Cr2, 650 °C/30 h

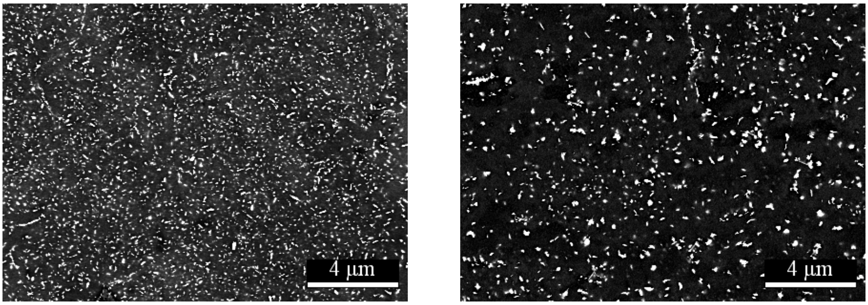

(e) 17Cr1, 650 °C/1,000 h

(f) 17Cr2, 650 °C/1,000 h

Figure 4.22: Microstructure development of recrystallization annealed 17Cr1 and 17Cr2 samples during annealing at 650 °C

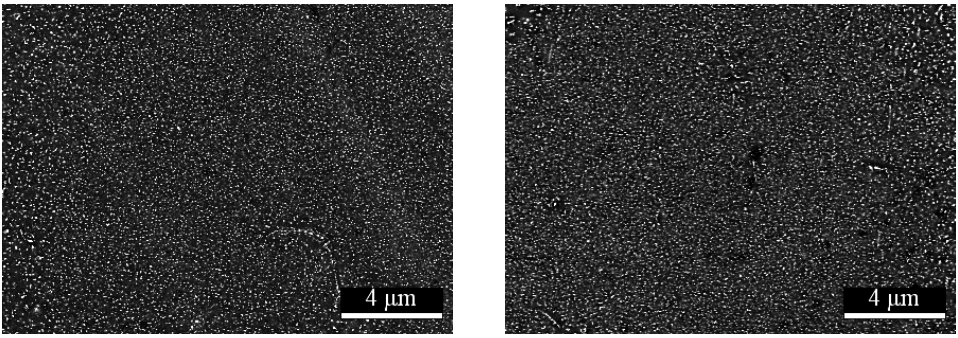

(a) 650 °C/3 h

(b) 650 °C/30 h

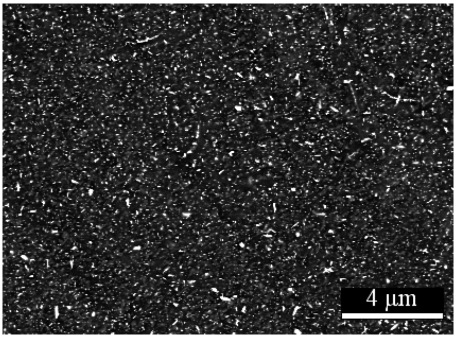

(c) 650 °C/1,000 h

Figure 4.23: Microstructure development of recrystallization annealed 17Cr3 samples during annealing at 650 °C

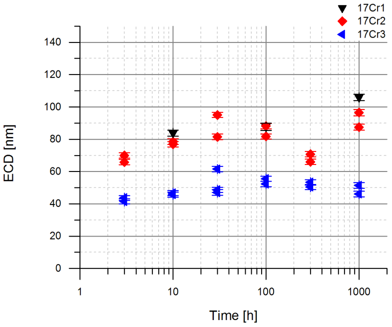

Figure 4.24: Equivalent circular diameter development of recrystallization annealed 17Cr1, 17Cr2, and 17Cr3 samples during isothermal annealing at 650 °C

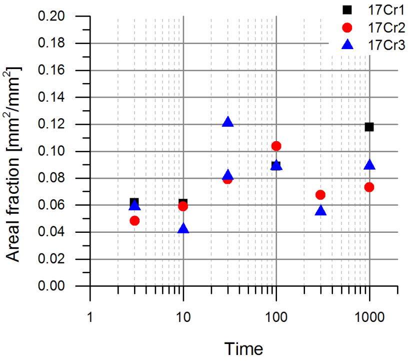

Figure 4.25: Areal fraction development of recrystallization annealed 17Cr1, 17Cr2, and 17Cr3 samples during isothermal annealing at 650 °C

experiments were performed at temperatures from 700 up to 900 C with 50 °C steps and annealing times of 15 and 30 minutes. SEM micrographs, depicting grain boundaries and grain interior, are given in Figure 4.31 and Figure 4.32. Laves phase particles were almost exclusively observed at the grain boundaries of the samples annealed at 700 °C (Figure 4.31a and Figure 4.31b).

Precipitation at grain boundaries and in the grain interiors was observed in the samples annealed at 750 °C and higher. The size of particles as well as their density in the grain interiors did not alter significantly with longer annealing in the samples annealed at 800, 850, and 900 °C. Longer annealing time caused coarsening of precipitates at grain boundaries (Figure 4.31a and Figure 4.31b).

As mentioned in the preceding part, annealing experiments evaluating the effect of existing precipitates which were formed during previous short term high temperature tempering on the morphology of Laves phase particles after annealing at 650 °C were performed. The combined heat treatment consisted of 30 minutes tempering at 700, 750, 800, 850, and 900 °C and subsequent annealing at 650 °C for 100 hours. Microstructures of grain boundaries and grain interiors after the combined annealing are depicted in Figure 4.33.

A fine dispersion of Laves phase particles in the grain interiors was observed in the samples tempered at 700 and 750 °C. Particle Free Grain Boundary Zone (PFGBZ) observed in the sample tempered at 700 °C is smaller compared to the sample tempered at 750 °C. Grain boundaries are fully decorated in both of the samples (Figure 4.33a and Figure 4.33b).

Coarse particles in the grain interiors were observed in all the samples tempered at 800 °C and

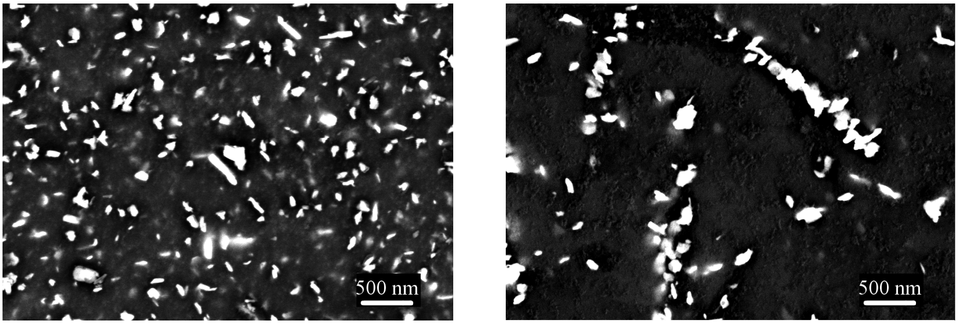

(a) 17Cr1 (b) 17Cr2

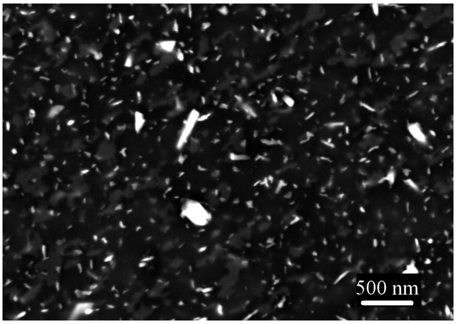

(c) 17Cr3

Figure 4.26: Detail of microstrucutre of 17Cr1 (a), 17Cr2(b), and 17Cr3(c) specimens after 1,000 hours of annealinf at 650 °C (25,000 magnificaiton)

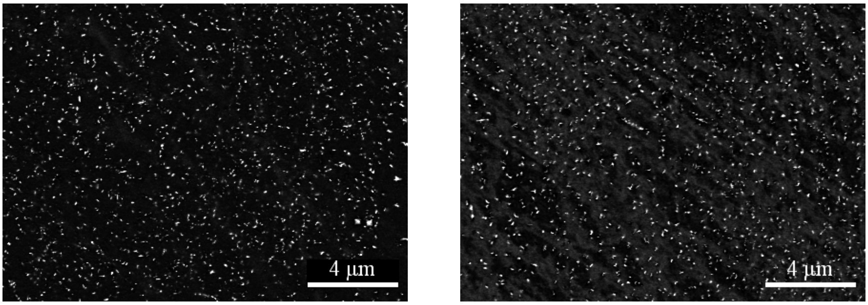

(a) Temp1, 650 °C/3 h

(b) 1Temp2, 650 °C/3 h

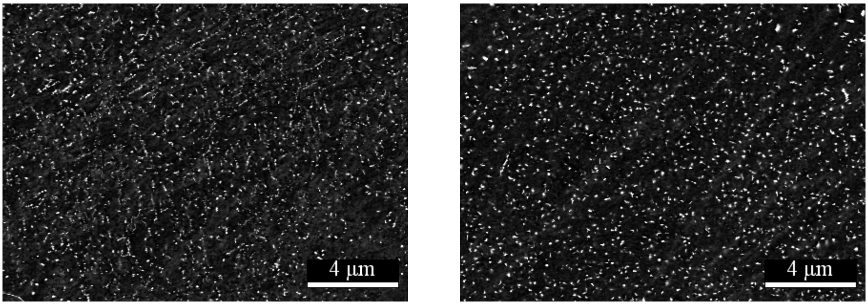

(c) Temp1, 650 °C/100 h

(d) Temp2, 650 °C/30 h

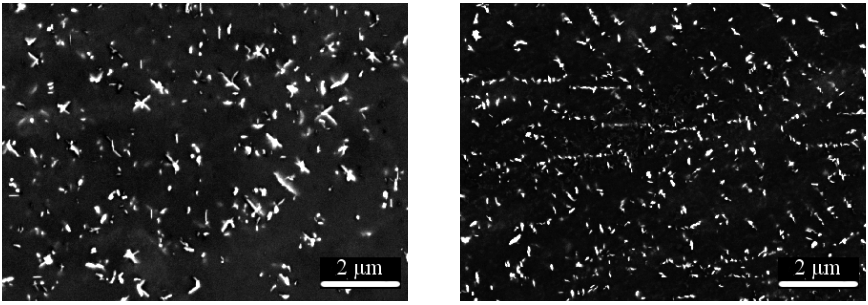

(e) Temp1, 650 °C/1,000 h

(f) Temp2, 650 °C/1,000 h

Figure 4.27: Microstructure development of the tempered specimens "Temp1" and "Temp2" during annealing at 650 °C

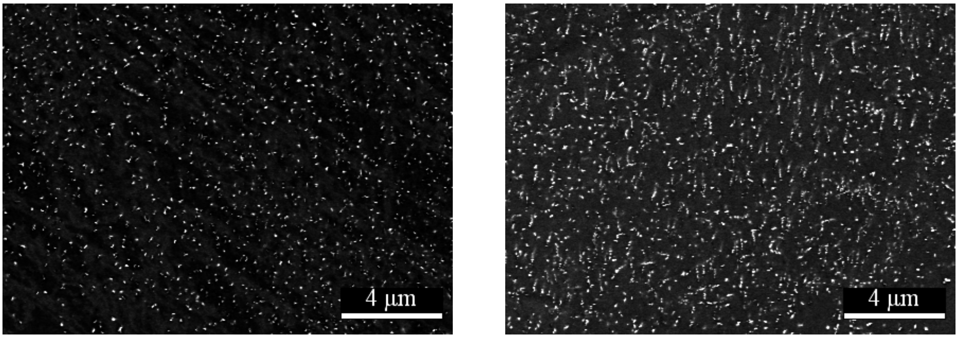

(a) Temp3, 650 °C/3 hours (b) Temp3, 650 °C/30 hours

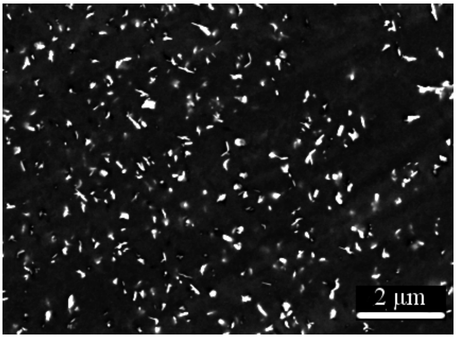

(c) Temp3, 650 °C/1,000 hours

Figure 4.28: Microstructure development of the tempered specimens "Temp3" during annealing at 650 °C

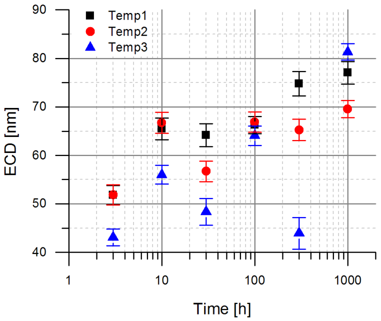

Figure 4.29: Laves phase particles equivalent circular diameter development of the tempered 17Cr1 samples during isothermal annealing at 650 °C

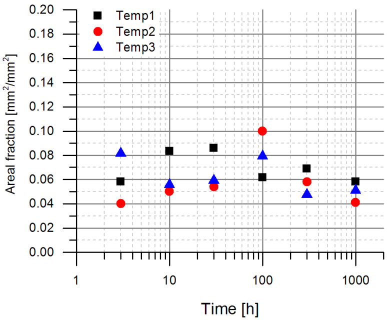

Figure 4.30: Precipitates areal fraction development of the tempered 17Cr1 samples during isothermal annealing at 650 °C

higher. The size of particles after combined annealing increased with increasing tempering temperature. A fine, continous dispersion of Laves phase particles at grain boundaries was observed in the sample tempered at 800 °C (Figure 4.33c) In samples tempered at 850 and 900 °C (Figure 4.33d and Figure 4.33e, respectively), the were grain boundaries were covered continuously, but mixture of fine and coarse particles was encountered.

4.5 Creep properties of 17Cr1 HiperFer steel in different thermomechanical treatment states

The 17Cr2 and 17Cr3 HiperFer steels were small ingot melts prepared by drop casting and were exclusively used for the evaluation of influence of chemical compositions on Laves phase formation. For this, the creep properties of 17Cr1 steel in different thermomechanical treatment states will be discussed in the following sections. All creep deformation and creep rate data are described by a self developed model. Detail description of the model is given in the subsection 4.6.1.

4.5.1 Rolled 17Cr1

The rolling parameters of 17Cr1 HiperFer steel in the last rolling step are given in Table 4.3. The positive influence of increased dislocation density, caused by increased rolling deformation on the Laves phase particle morphology, was presented subsection 4.4.1.

The 17Cr1_1 and 17Cr1_2 samples were tested at 120, 110, 100 MPa, the 17Cr1_3 specimens at 120

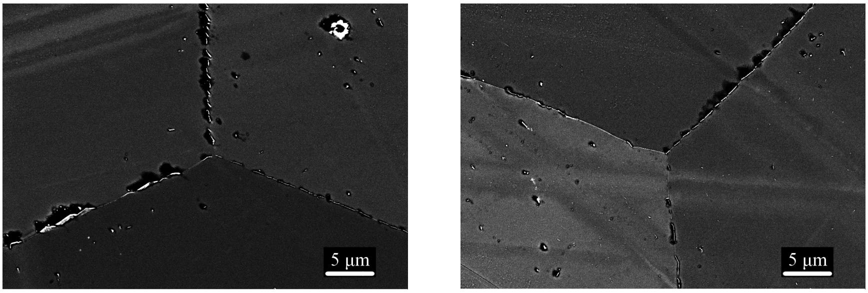

(a) 700 °C/15 min (b) 700 °C/30 min

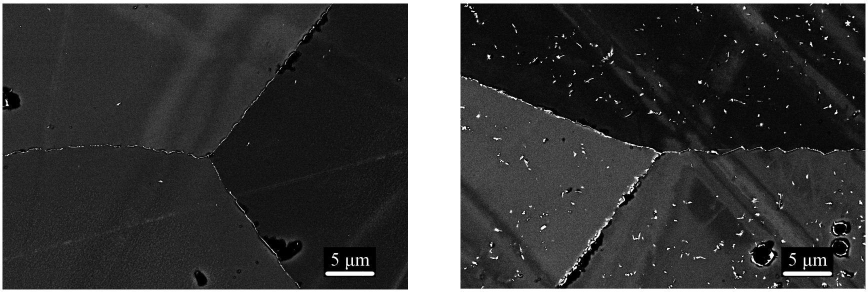

(c) 750 °C/15 min (d) 750 °C/30 min

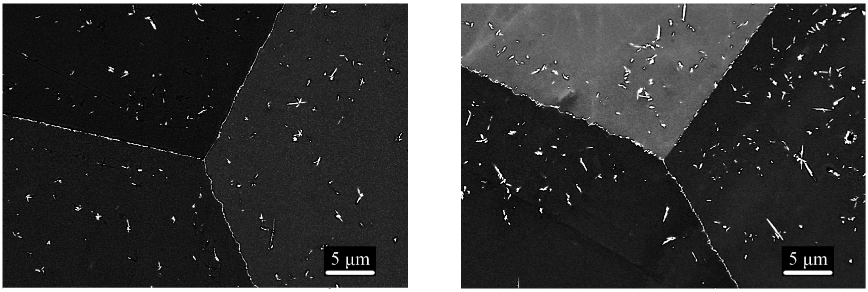

(e) 800 °C/15 min (f) 800 °C/30 min

Figure 4.31: Formation of Laves phase particles at grain boundaries and grain interiors during short term annealing at temperatures from 700 up to 800 °C

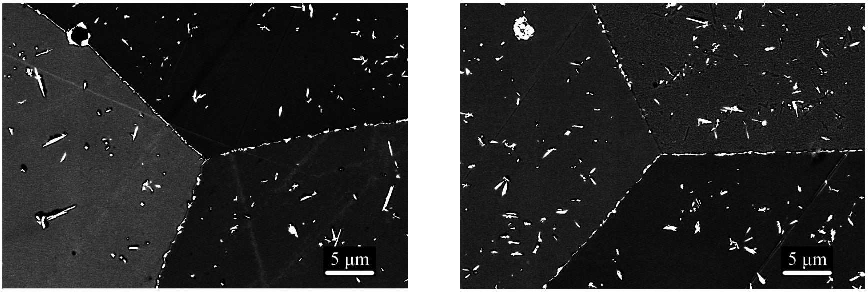

(a) 850 °C/15 min

(b) 850 °C/30 min

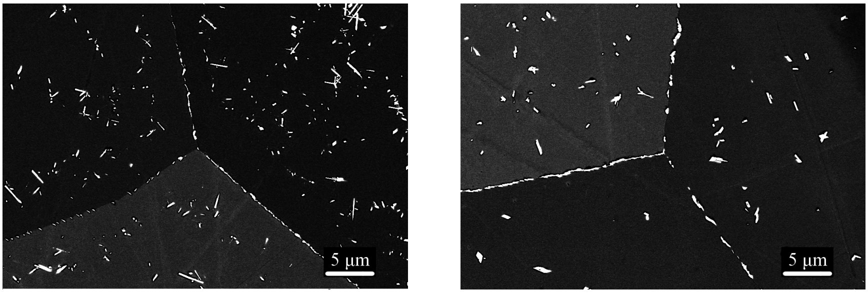

(c) 900 °C/15 min

(d) 900 °C/30 min

Figure 4.32: Formation of Laves phase particles at grain boundaries and grain interiors during short term annealing at temperatures from 850 and 900 °C

Table 4.3: Temperature and deformation ot 17Cr1 HiperFer steel during the last rolling step

Material	Deformation [%]	Teperature [°C]
17Cr1_1	7	1000
17Cr1_2	10	920
17Cr1_3	25	875

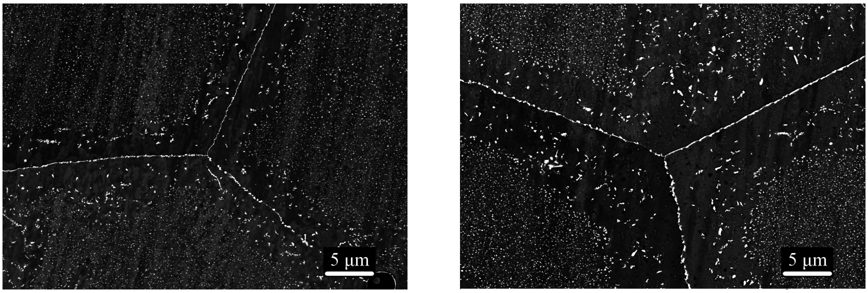

(a) 700 °C/30 min + 650 °C/100 hours

(b) 750 °C/30 min + 650 °C/100 hours

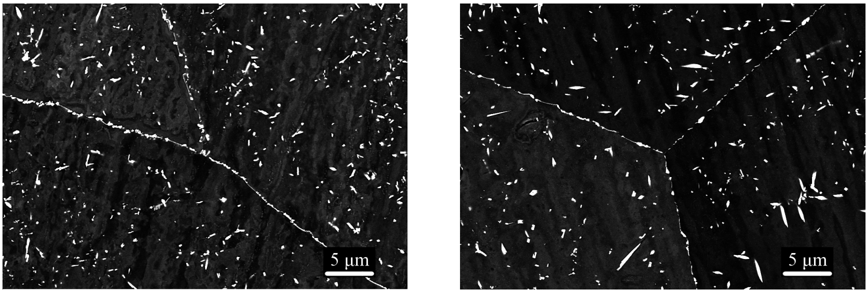

(c) 800 °C/30 min + 650 °C/100 hours

(d) 850 °C/30 min + 650 °C/100 hours

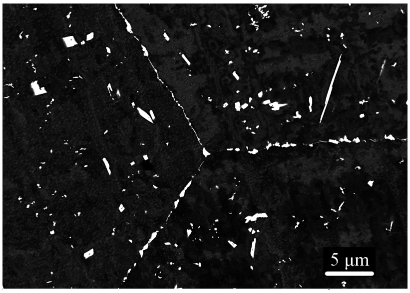

(e) 900 °C/30 min + 650 °C/100 hours

Figure 4.33: Microstructure of samples after combined high temperature + 650 °C annealing

and 100 MPa. Furthermore, all the three rolling variants are tested at 70 MPa (the experiments are still in progress, August 2016). An overview of the creep experiments and their results is given in Table 4.4. Time to rupture data of completed and running experiments is shown in Figure 4.34. The time to rupture data of P91 and P92 feritic-martensitic steels [53, 54] are included for comparison.

The time to rupture of the 17Cr1_1 and 17Cr1_2 specimens at 120 MPa are shorter in comparison to P91 steel, but at 110 MPa P91 steel exhibited shorter creep life compared to the 17Cr_1 and 17Cr_2 specimens. At 100 MPa, the 17Cr1_1 and 17Cr1_2 specimens exhibited notably longer life than P91 steel, but shorter than P92. The creep life of the 17Cr1_3 specimens was comparable to the lifetime of P92 at stress levels of 120 and 100 MPa. From creep test results conducted at stresses above 70 MPa it can be expected, that the time to rupture of creep tests at 70 MPa for all the three rolling variants will be close to, or even longer than the time to rupture of P92 steel.

The total creep rupture deformation of all rolling variants of 17Cr1 HiperFer steel is presented in Figure 4.35. The results of TP91 [54] and TP92 [53] as published by the National Institute for Material Science, Japan are given for comparison. A continuous decrease of creep rupture elongation was observed in case of the 17Cr1_1 and 17Cr1_2 rolling variants. The maximum creep rupture deformation was 25 pct. in case of the 17Cr1_2 sample tested at 120 MPa, the minimum measured deformation was 13 pct. in case of the 17Cr1_2 sample tested at 100 MPa. The creep rupture deformation of the 17Cr1_3 samples did not vary significantly with creep life and was about 10 pct. The creep rupture deformation of all the rolling variants was approx. two times smaller than in case of TP91 steel. Creep rupture deformation of TP92 steel was about 20 pct. bigger compared to the 17Cr1_1 and 17Cr1_2 samples for all the lifetimes.

The microstructure of HiperFer steel varies significantly during creep life; the initial microstructure is almost free of Laves phase precipitates (cf. section 4.2). Within short time a fine dispersion of Laves phase particles develops (cf. section 4.3). For this reason, HiperFer steel may be classified as an age hardenable creep resistant steel.

The creep properties of rolled 17Cr1 specimens will be exemplary discussed for the 17Cr1_1 set. Development of total deformation over time during creep experiments is shown in Figure 4.36, the change of creep rate during time is depicted in Figure 4.37. Several distinct regions can be identified in the creep curves. Almost no deformation was observed in the first part (region A), followed by a rapid increase of deformation (region B). Standard primary creep was observed in region C. A short secondary creep stage was observed in case of all the three experiments, which was followed by rapid increase of deformation in the tertiary stage (region D).

No significant difference of microstructure was observed in the head and gauge sections of ruptured creep specimens. Remains of the original subgrain structures were observed in the head section of the 17Cr1_1 (650 °C/100 MPa/1,594 h) specimens only (Figure 4.38). They were visible in the head and gauge sections of the 17Cr1_2 (650 °C/100 MPa/2,092 h) and the 17Cr1_3 (650 °C/120 MPa/767 h) specimens (Figure 4.39 andFigure 4.40).

Metallographic pictures taken from the gauge and head sections of the ruptured creep specimens were evaluated. The Equivalent Circular Diameters (ECD) of particles in the gauge and head

Table 4.4: Results of 17Cr1_1, 17Cr_2, and 17Cr_3 materials

Material	Stress [MPa]	Teperature [°C]	Time to rupture [h]	Rupture deformation [%]	Status
17Cr1_1	120	650	58	25	ruptured
	110	650	166	24	ruptured
	100	650	1,594	was not measured	ruptured
	70	650	2,603	-	running
17Cr1_2	120	650	30	29	ruptured
	110	650	263	27	ruptured
	100	650	2,092	16	ruptured
	70	650	3,032	-	running
17Cr1_3	120	650	767	13	ruptured
	100	650	4,387	11	ruptured
	70	650	2,008	-	running

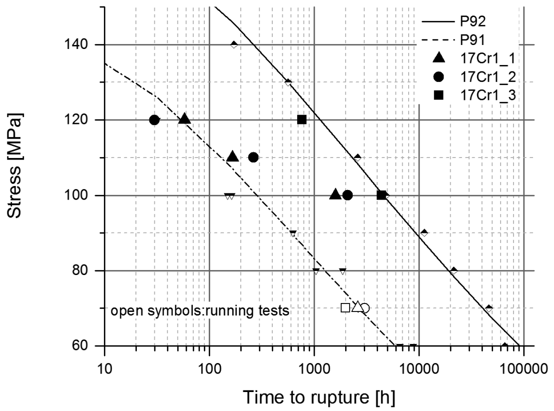

Figure 4.34: Time to rupture of rolled 17Cr1_1, 17Cr_2, and 17Cr1_3 HiperFer steel at 650 °C

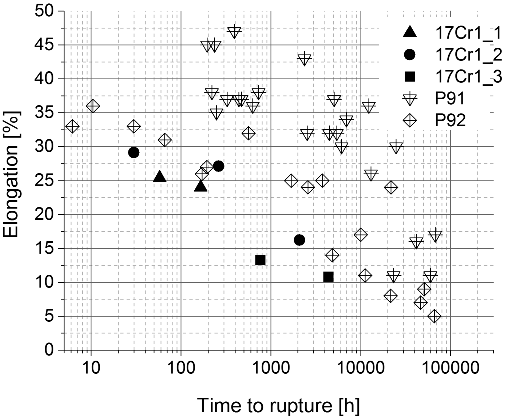

Figure 4.35: Time to rupture of rolled 17Cr1_1, 17Cr_2, and 17Cr1_3 HiperFer steel at 650 °C

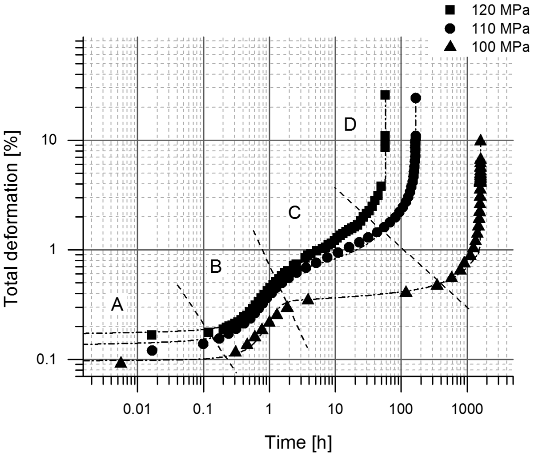

Figure 4.36: Creep deformation curves of 17Cr1_1 specimens at 650 °C

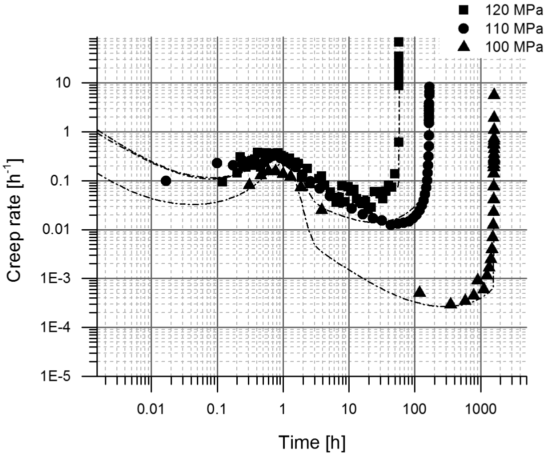

Figure 4.37: Creep rate curves of 17Cr1_1 specimens at 650 °C

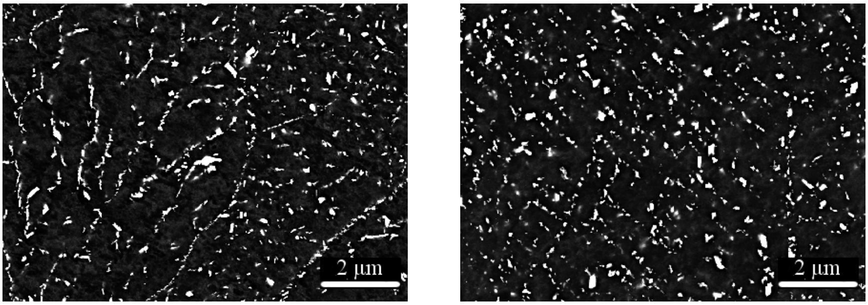

(a) Head section

(b) Gauge section

Figure 4.38: Microstructures of the 17Cr1_1 creep specimen (650 °C/100 MPa/1,594 h)

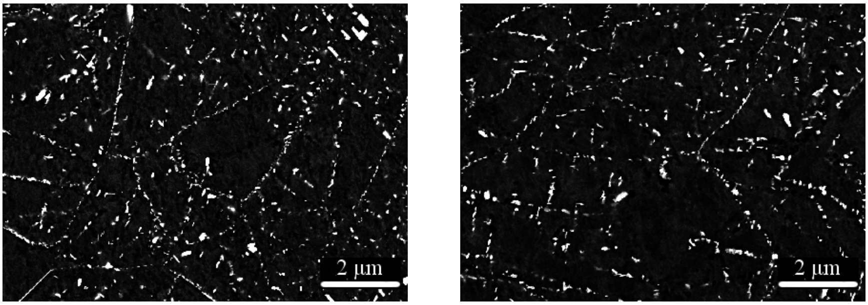

(a) Head section (b) Gauge section

Figure 4.39: Microstructures of the 17Cr1_2 creep specimen (650 °C/100 MPa/2,092 h)

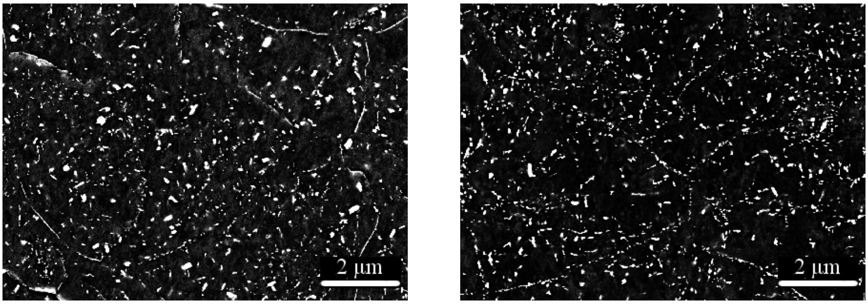

(a) Head section (b) Gauge section

Figure 4.40: Microstructures of the 17Cr1_3 creep specimen (650 °C/120 MPa/767 h)

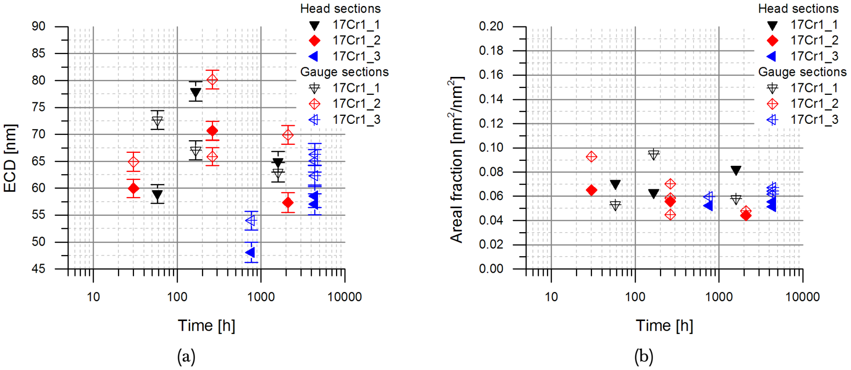

Figure 4.41: Evaluated ECD (a) and areal fraction (b) of Laves phase particles in ruptured creep specimens

sections are depicted in Figure 4.41a. The size of particles varies between 47 and 80 nm. No significant coarsening was observed, and the particles in head sections were appr. 10-15 pct. smaller than in the gauge section of specimens. If the size difference was caused by stress accelerated coarsening in the gauge sections, or by slightly lower temperature in the head sections is not yet clear. This question is a subject of a broader future experimental program. The values of Laves phase areal fraction ranged from 4 pct. up to 10 pct. Higher values of areal fraction were observed in the gauge sections, usually with a difference of appr. 2-4 pct (Figure 4.41b).

4.5.2 Thermally treated 17Cr1

The positive influence of enhanced dislocation density on microstructural development and creep properties was presented in the previous sections.

Dislocation driven precipitation and enhanced dislocation strengthening by optimized rolling is not applicable in all the technical applications relevant to steam power plants, e.g. in case of casted tubes and blades/vanes, or turbine housings.

Furthemore, construction of a power plant is impossible without welding. Welded joints represent complicated structures with (usually) variance in chemical composition, and thermal and stress history (always). The influence of post-weld heat treatment on the hardness of E-beam butt welds was reported in [55], where the measured peak HV03 hardness of a weldment without post weld heat treatment was 313, whereas the hardness of the parent material was between 220 and 230. After tempering at 500 °C for 5 hours, almost no difference in the hardness profiles of the parent material and the weldment remained.

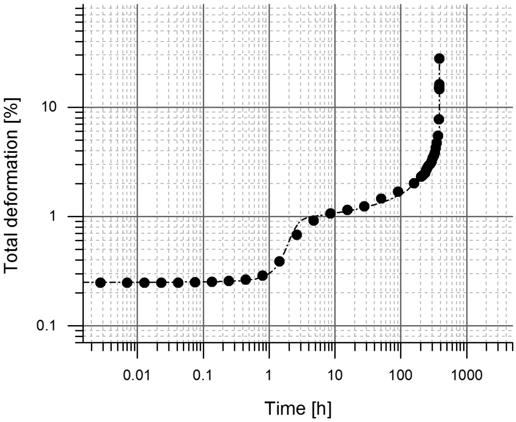

Figure 4.42: Creep deformation curve of a recrystallized 17Cr1 specimen at 650 °C/100 MPa

These were the main reasons to study the creep properties of the 17Cr1 steel after applying different heat treatments. 17Cr1_1 creep specimens were applied in this study. All the specimens were recrystallization annealed at 1075 °C for 15 minutes, which was sufficient to dissolve all primary particles formed during rolling. All creep experiments were conducted at 650 °C and 100 MPa. The influence of tempering bellow and above 650 °C will be discussed in the following sections.

Recrystallized 17Cr1 material

The time to rupture of a recrystallized 17Cr1 creep specimen (650 °C and 100 MPa) was 386 hours, which equals a 75 pct decrease in comparison to the lifetime of the (as rolled) 17Cr1_1 and more than 90 pct. to the 17Cr1_3 tested at 650 °C and 100 MPa (cf.Table 4.4). The creep curve of the recrystallized specimen is depicted in Figure 4.42, the creep rate curve in Figure 4.43. Significant sigmoidal behaviour was observed in the early stage of creep. The initial deformation was 0.25 %, the total deformation at the end of sigmoidal creep was 0.68 %. The initial deformation of the 17Cr1_1 specimen at 650 °C and 100 MPa was 0.09 % and the total deformation at the end of sigmoidal creep was 0.17 % (cf. Figure 4.37 and Figure 4.42). This difference is clearly attributable to the lack of dislocation strengthening in the recrystallized specimen.

Laves phase particles precipitated randomly in the head section of the creep specimen (Figure 4.44a), and decorated original dislocation structures in the gauge section (Figure 4.44b). The

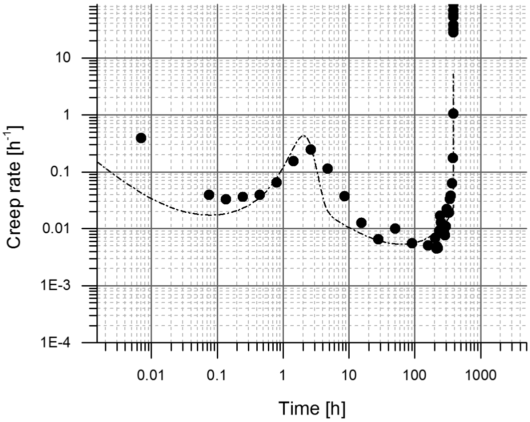

Figure 4.43: Creep rate curve of a recrystallized 17Cr1 specimen at 650 °C/100 MPa

ECDs of the Laves phase particles were 66±1.7 nm / 76±1.8 nm in the gauge / head section. 4 pct. of area was covered by particles in the head section and 4.9 pct. in the gauge section.

Low temperature tempered 17Cr1 material

The significant difference in creep properties of as rolled and recrystallized material was the motivation to evaluate the influence of long term tempering at low temperature. Furthermore, it was supposed to be the initial experiment for design of post weld heat treatment of welded specimens.

Three specimens were tested at 650 °C and 100 MPa with different initial heat treatment. The applied heat treatments were 1075 °C/15 min+475 °C/5 h (Temp1), 1075 °C/15 min+510 °C/5 h (Temp2), and 1075 °C/15 min+540 °C/5 h (Temp3). The results of the creep experiments are listed in Table 4.5, creep deformation curves are depicted in Figure 4.45, and creep rate curves in Figure 4.46. Sigmoidal creep was observed like in the previous cases. The measured initial deformation of low temperature tempered Temp1, Temp2, and Temp3 specimens were 0.2, 0.1, and 0.12 %. The Temp1 specimen reached 0.51 % of deformation at the end of sigmoidal creep, the Temp2 0.42 %, and the Temp3 exhibited standard primary creep after 0.32 % deformation. The Temp1 specimen exhibited the shortest time to rupture with lifetime of 152 hours, the Temp2 specimen ruptured after 309 hours, and the Temp3 specimen reached 1,542 hours. The total rupture deformation ranged from 20.88 % in case of the Temp3 specimens up to 22.54 % in case of the Temp1 specimen (Figure 4.45).

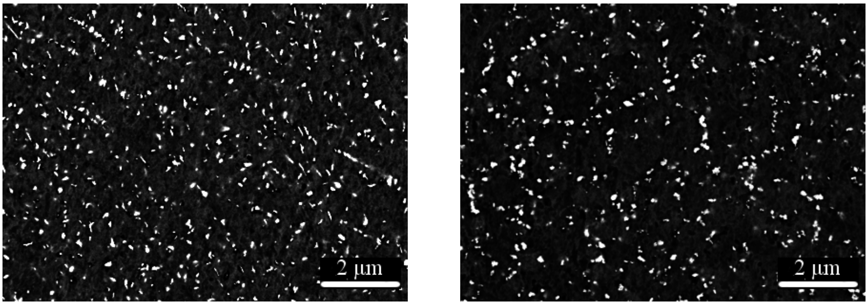

(a) Head section (b) Gauge section

Figure 4.44: Microstructure of recrystallized 17Cr1 creep specimen (650 °C/100 MPa/386 h)

Table 4.5: Overview of creep results of tempered 17Cr1 specimens

Denomination	Tempering	Stress [MPa]	Teperature [°C]	Time to rupture [h]	Rupture deformation [%]
Temp1	475 °C/5 h	100	650	152	35
Temp2	510 °C/5 h	100	650	309	26
Temp3	540 °C/5 h	100	650	1,542	24

Like mentioned in the previous paragraph, the sigmoidal creep behaviour was observed during testing of creep specimens which were tempered below 650 °C. Sigmoidal creep is characterized by an increase in creep rate after loading and a consecutive transition to standard primary creep, where creep rate decreases (Figure 4.46). The Temp1 specimen reached the end of sigmoidal creep after 2.6 hours, the Temp2 and Temp3 specimens after 1.6 hours. The minimum creep rate decreased with increasing tempering temperature. The Temp1 specimen exhibited a minimum creep rate of $\dot{\epsilon} = 1.8 \cdot 10^{-2}$ h^{-1} after 57 hours, the Temp2 specimen reached a minimum creep rate of $\dot{\epsilon} = 7.7 \cdot 10^{-3}$ h^{-1} after 90 hours, while a minimum creep rate $\dot{\epsilon}$ of the Temp3 specimen was of $6.1 \cdot 10^{-4}$ h^{-1} and was measured after 359 hours of testing. The secondary creep regime was reduced to an inflection point and linear increase of creep rate was observed in the tertiary stage of creep.

Microstructures of gauge and head sections of the tempered specimens are given in Figure 4.47. The micrographs do not differ significantly. The ECD values of the Laves phase particles in the tempered 17Cr1 creep specimens were in the range from 69 up to 79 nm. The size of Laves phase particles in the Temp1 and Temp2 specimens were comparable and a slight decrease in the ECD value was observed in case of the Temp3 specimen (Figure 4.48). The areal fraction of

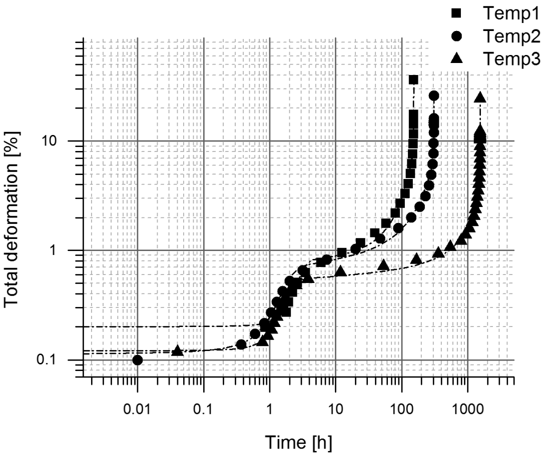

Figure 4.45: Creep deformation curve of recrystallized and low-temperature tempered 17Cr1 specimen at 650 °C/100 MPa

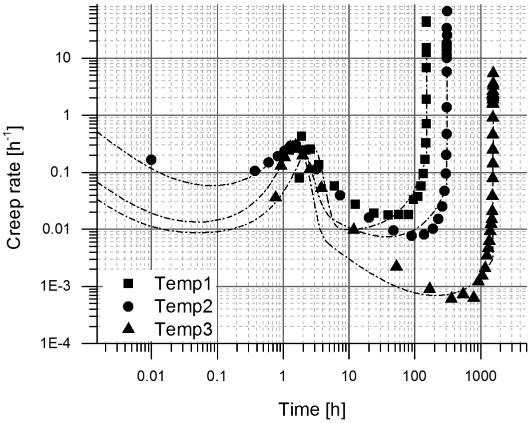

Figure 4.46: Creep rate curve of recrystallized and low-temperature tempered 17Cr1 specimen at 650 °C/100 MPa

Table 4.6: Overview of creep results of high temperature tempered 17Cr1 specimens

Denomination	Tempering	Stress [MPa]	Teperature [°C]	Time to rupture [h]	Rupture deformation [%]
HTT1	800 °C/15 min	100	650	1,304	29
HTT2	850 °C/15 min	100	650	22	41

Laves phase particles in the Temp1 specimen was 4.5 pct., while the highest areal fraction (7.5 pct.) was observed in the Temp2 specimen. The Temp3 specimens exhibited an areal fraction of 5 pct.

High temperature tempered 17Cr1 material

Enhanced dislocation strengthening by fine dispersion of precipitates, acceleration of precipitation, and the minimization of initial deformation were the main goals of low temperature tempering. Dislocation strengthening is the main strengthening mechanism during primary and secondary creep. Grain boundary strengthening becomes important during the tertiary creep stage, when sliding of grains is one of the dominant deformation mechanisms. The material is plastically deformed in the tertiary stage of creep and decoration of grain boundaries by coarse particles can retard grain boundary sliding during the tertiary stage of creep and thus increase creep life.

Short term tempering at high temperatures can only be effective when grain boundaries are already decorated and grain interiors are still (almost) free of Laves phase particles. This is reached by different rates of precipitation at grain boundaries and grain interiors. By such heat treatment, the grain boundaries are strengthened from beginning of creep exposure and there are enough Laves phase forming elements in solid solution to form fine precipitates that ensure dislocation strengthening.

Efficiency of short term, high temperature tempering was studied on two specimens. The HTT1 specimen was tempered at 800 °C for 15 minutes, the HTT2 specimen at 850 °C for 15 minutes. Both the specimens were recrystallization annealed at 1075 °C/15 minutes prior to annealing at 800, and 850 °C alternatively. An overview of the creep results is given in Table 4.6, creep deformation curves are depicted in Figure 4.50, and creep rate curves in Figure 4.51. Time to rupture of the HTT1 sample was 1,304 hours, but the HTT2 sample failed after 22 hours already. Sigmoidal creep was not distinct in case of the HTT1 specimen and was absent in case of the HTT2 specimen. Intrinsic deformation of the HTT1 specimen was 0.49 % and the HTT2 specimen deformed by appr. 0.5 % upon loading. Standard primary creep of the HTT1 specimen was observed after reaching 0.64 % (Figure 4.50), with a minimum creep rate of $1 \cdot 10$ h^{-1} (Figure 4.51). The HTT2 experiment does not represent a standard creep experiment, but a test of superplasticity properties.

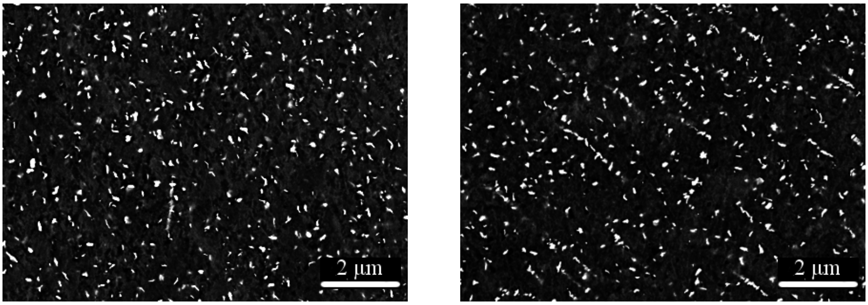

(a) Temp1, Head section

(b) Temp1, Gauge section

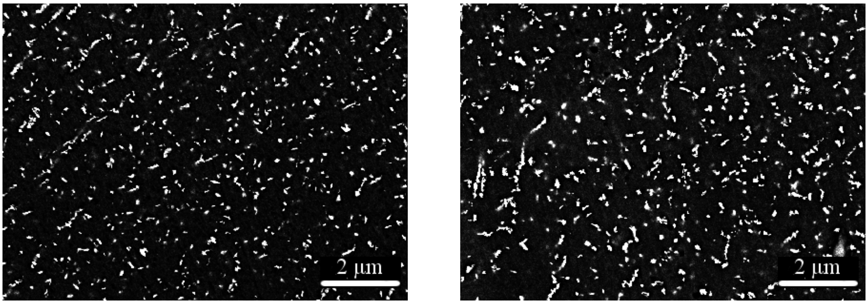

(c) Temp2, Head section

(d) Temp2, Gauge section

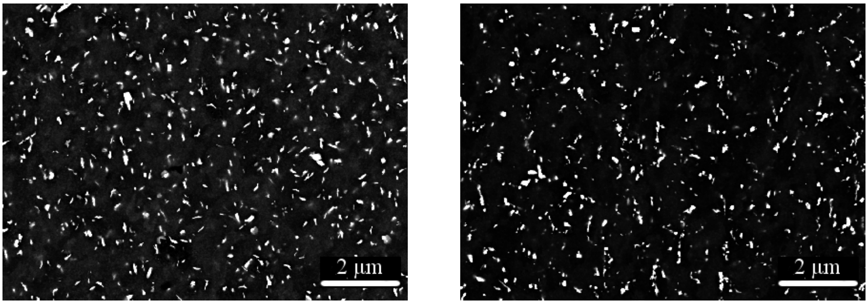

(e) Temp3, Head section

(f) Temp3, Gauge section

Figure 4.47: Microstructure of low temperature tempered 17Cr1 creep specimens

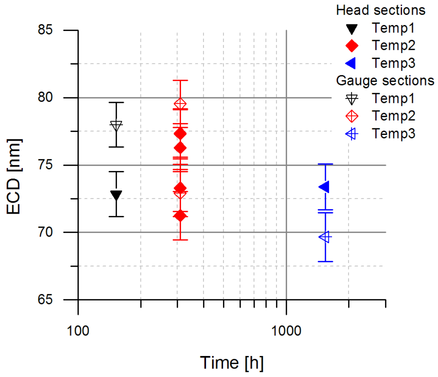

Figure 4.48: ECD of particles in the low-temperature tempered 17Cr1 creep specimens

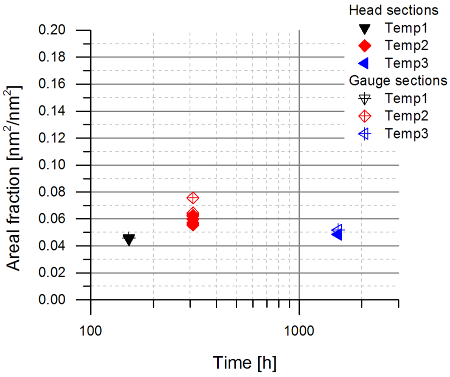

Figure 4.49: Areal fractions of particles in the low-temperature tempered 17Cr1 creep specimens

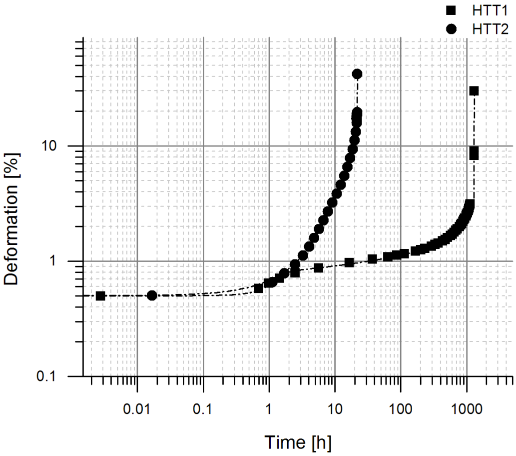

Figure 4.50: Creep deformation curves of the high temperature tempered 17Cr1 specimens at 650 °C/100 MPa

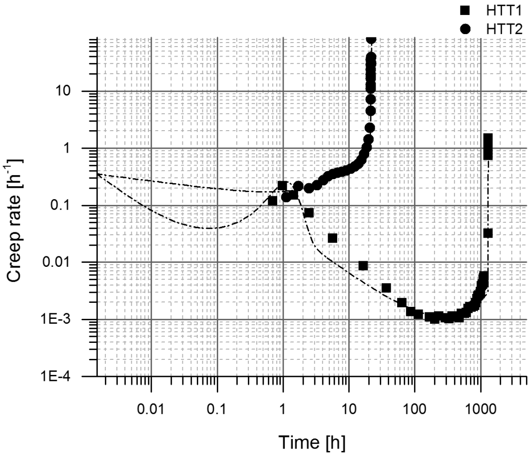

Figure 4.51: Creep rate curves of the high temperature tempered 17Cr1 specimens at 650 °C/100 MPa

Difference in creep behaviour of the HTT1 and HTT2 specimens is caused by microstructural deviation (Figure 4.52). A fine dispersion of Laves phase particles was observed in the head and gauge sections of the HTT1 specimen (Figure 5.11a and 4.52b, respectively), with ECD values from 60 to 69 nm. Continuous precipitation of coarse particles at grain boundaries and Particle Free Zone (PFZ) along them was observed. The HTT2 specimen presented dispersion of coarse particles in the grain interiors with ECDs from 204 to 270 nm (Figure 5.11b and 4.52d). Short term tempering at 850 °C thus caused precipitation of large particles, which were not effective enough in Orowan strengthening.

4.6 Modeling

Modeling in material science represents a broad spectrum of different disciplines - from atomistic modeling, over continuum thermodynamic and finite element to stochastical statistical modeling. Two types of modeling were performed in this thesis - thermodynamic modeling, and statistical modeling of creep deformation curve. Calculation of phase diagrams was presented at the beginning of this chapter. Modeling of particle growth by TC Prisma, and creep deformation curve modeling will be presented in the following sections.

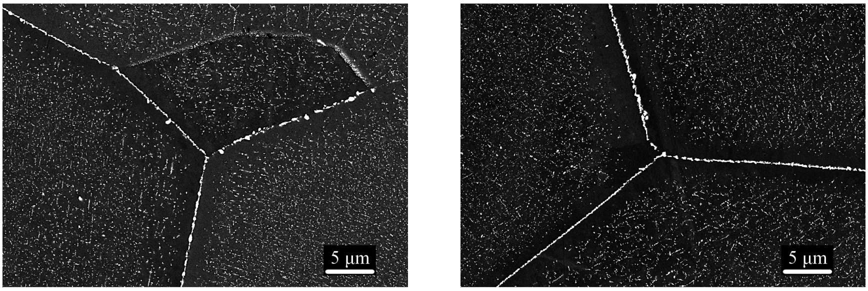

(a) HTT1, Head section

(b) HTT2, Gauge section

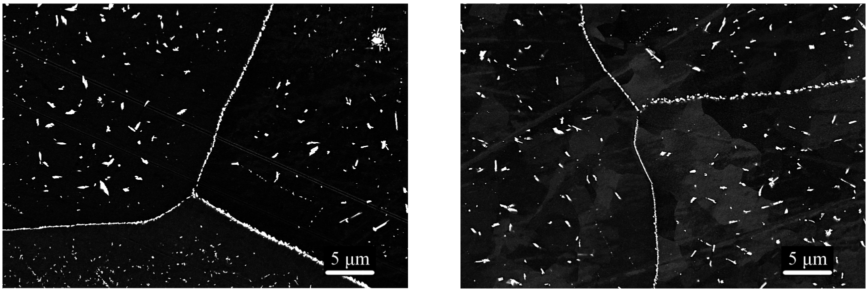

(c) HTT2, Head section

(d) HTT2, Gauge section

Figure 4.52: Microstructure of high temperature tempered 17Cr1 creep specimens

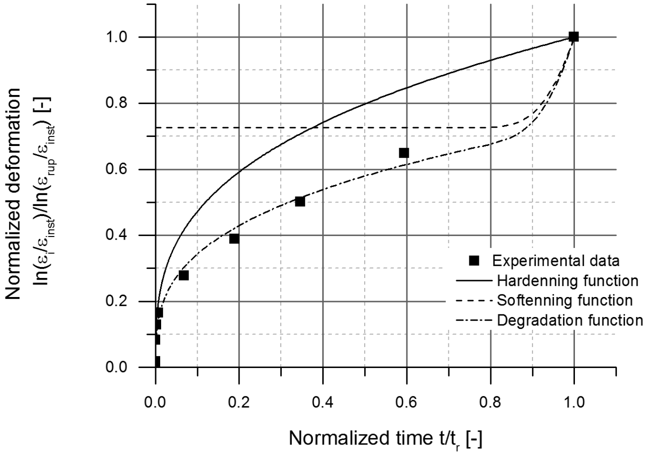

Figure 4.53: Normalized creep deformation data of 1Cr05Mo025V steel tested at 500 °C and 177 MPa

4.6.1 Creep curve modeling

Creep curve model developed by Bina at al. [45, 56] was used as a base for development of a model suitable for creep curves of HiperFer steel. Development of creep deformation of HiperFer steel is characterized (section 4.5) by:

(a) significant sigmoidal creep after loading,

(b) a minimal secondary creep stage, and

(c) a rapid increase of deformation in the tertiary stage.

The properties of the model with degradation function in form of Equation 2.17 will be presented by interpolation of the creep data of a ductile low alloyed 1Cr05Mo025V steel [57]. Creep data of 1Cr05Mo025V steel, tested at 500 °C and 177 MPa, are presented in Figure 4.53. The plot represent normalized stress $ln\left(\frac{\epsilon_i}{\epsilon_{inst}}\right)/ln\left(\frac{\epsilon_{rup}}{\epsilon_{inst}}\right)$ over normalized time t_i/t_r. Figure 4.53 depicts courses of the softening function, the hardening function and the degradation function (Equation 2.17). Creep deformation data and creep rate values are close to the modeled curves (Figure 4.54).

If the original model, developed by Bina at al. [45, 56], is applied to HiperFer steel, the interpolation properties are poor (Figure 4.55, Figure 4.56). The secondary creep stage is reduced to

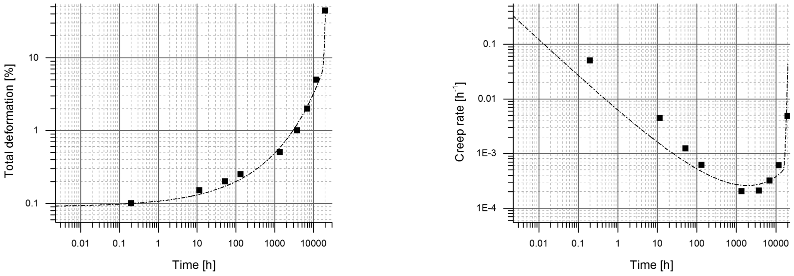

(a) Deformation

(b) Creep rate

Figure 4.54: Creep deformation and creep rate curves of 1Cr05Mo025V steel tested at 500 °C and 177 MPa

a sharp inflection (Figure 4.56b), furthemore interpolation of creep deformation and creep rate during the primary stage of creep is not accurate enough (Figure 4.56)
For this reason, the degradation function (Equation 2.17) was enlarged by a multiplicand, describing the sigmoidal behaviour, and the softening function was modified to interpolate the creep data of HiperFer steel experiments more accurately. The modified degradation function is given by the formula:

$$h(x_t) = \frac{1}{1 + a_5 \cdot (exp\,(-a_7 \cdot (x + a_8)))^{a_6}} \cdot x^{a_1} \cdot \left[\frac{1 + exp(-2 \cdot x_t^{a_2})}{1 + exp(-2)} \right]^{(a_3 + a_4 \cdot x_t)} \tag{4.1}$$

where a_1 ... a_8 are regression coefficients, and
x_t is given by Equation 2.18.

The modified model slightly underestimates creep strain development in late stage of creep (Figure 4.57), but the difference becomes negligible if the data are plotted in double logarithmic scaling (Figure 4.58). Furthemore, the influence of the particular subfunctions of the modified degradation function (Equation 4.1) is depicted. The prediction of creep deformation and creep rate curves of HiperFer steel by the modified model is satisfactory (Figure 4.59).

4.6.2 Growth of particles modeling

Results of annealing experiments of HiperFer steel at 650 °C after up to 1,000 h of annealing were introduced in section 4.4. In the subsection, influences of rolling parameters, heat treatment, and chemical composition were presented.

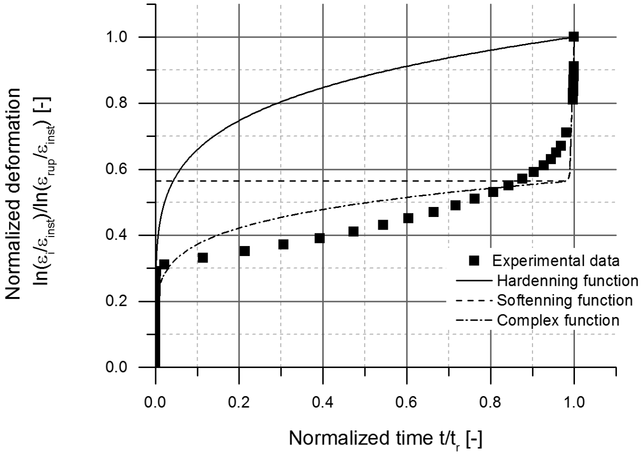

Figure 4.55: Normalized creep deformation data of 17Cr1_1 steel at 100 MPa evaluated by the original model

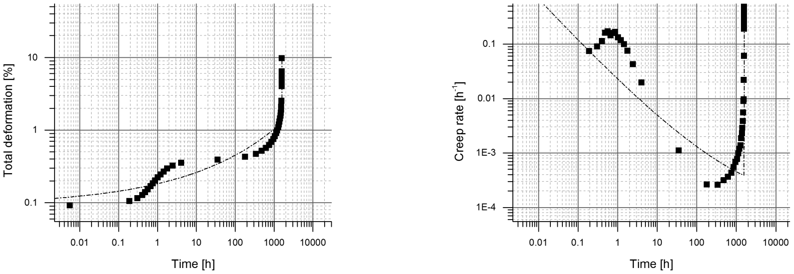

(a) Deformation

(b) Creep rate

Figure 4.56: Creep deformation and creep rate curves of of 17Cr1_1 steel at 100 MPa evaluated by the original model

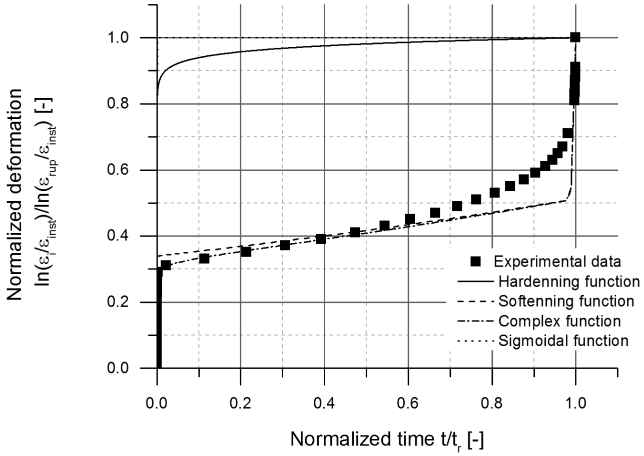

Figure 4.57: Normalized creep deformation data of 17Cr1_1 steel at 100 MPa and 650 °C evaluated by the modified model

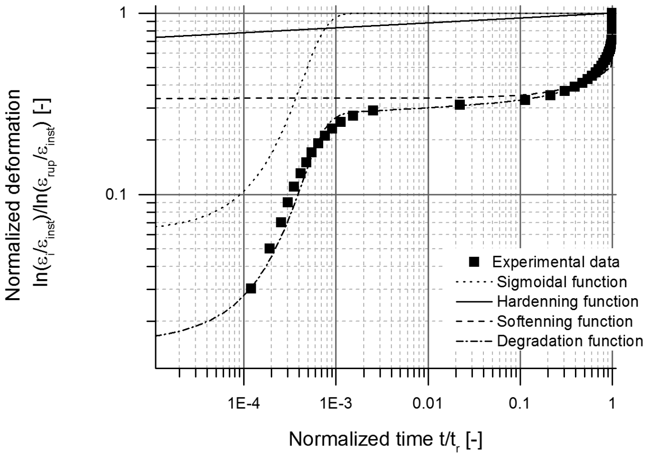

Figure 4.58: Creep curve of 17Cr1_1 steel at 100 MPa and 650 °C evaluated by the original model in double logarithmic plot

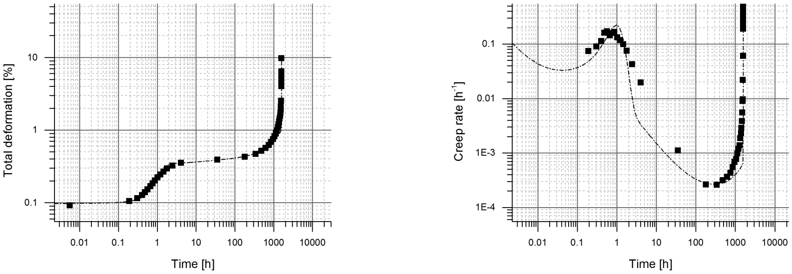

(a) Deformation

(b) Creep rate

Figure 4.59: Creep deformation and creep rate curves of of 17Cr1_1 steel at 100 MPa and 650 °C evaluated by the modified model

The growth of particles was modeled using the commercial software TC-Prisma (version 2.0) and utilizing the databases TCFE7 and MOBFE2. Basic information about solid state precipitation was given in the literature review (subsection 2.1.2). TC-Prisma calculates the whole precipitation process, incubation, growth, metastable state, and coarsening of precipitates. Modeling results are influenced by lot of physical parameters, like location of precipitation - e.g. on dislocations, grain corners, grain boundaries etc., phase boundary mobility, diffusion mobility, size of grains, dislocation density and others.

Modeling by TC-Prisma was used for the evolution of particles in grain interiors in material that was recrystallization annealed prior to annealing. Precipiation in the grain interiors, even in well annealed materials, is heterogeneous in nature and preferentialy occurs at dislocations because the driving force for homogeneous precipitation is significantly smaller [5]. A typical value of dislocation density of a well annealed FCC material is in range of $10^{11}m^{-1}$, at a well annealed BCC material in the range of $10^{12}m^{-1}$, this represents $4.4 \cdot 10^{20}$ and $4.4 \cdot 10^{21}$ potential nucleation sites, respectively [5]. The second aspect, which significantly influences precipitation behaviour, is the interfacial energy γ. The interfacial energy does have an influence on the beginning of the growth of precipitates, the size of precipitates in the metastable state, and the rate of coarsening. The values of interfacial energy of Laves phase particles in a ferrite matrix are commonly referred to be in the range from 0.7 to 0.85 [58, 59]. A set of calculations was performed to settle correct values of dislocation density and interfacial energy. The predicted size of precipitates was compared with the observed results of the 17Cr1 samples starting from the solution annealed state, and with the low temperature tempered Temp1 and Temp3 states (subsection 4.4.2 and subsection 4.4.3). The influence of interfacial energy and dislocation density on the predicted size of Laves phase particles in the metastable stage of precipitation is shown in Figure 4.60. The predicted size of particles increases dramatically with slight increasing values of interfacial energy, whereas increasing dislocation density causes a refinement of particles.

Despite of scatter, the observed particles seem to be in the metastable stage of precipitation in all cases (e.g. Figure 4.17, Figure 4.24, or Figure 4.29). The average size of particles in the 17Cr1 samples starting from the solution annealed state is 93 nm (min. size 84 nm and max. size 106 nm), size of particles in Temp1 specimens varied from 52 up to 77 nm with an average size of 67 nm. The average size of particles in the Temp3 specimens was 58 nm and varied between 44 and 81 nm. The predicted size of the Laves phase particles in 17Cr1 steel with different heat treatments is depicted in Figure 4.61. Average, minimal, and maximal size of observed particles are indicated. The combination of $\gamma = 0.177$ Jm^{-2} and $\rho = 1.210^{12}m^{-1}$ m^{-3} seems to be optimal for the calculations representing precipitation starting from the recrystallization annealed state (Figure 4.61a) and the Temp3 state (Figure 4.61c), but these parameters overpredict size of the Laves phase particles in samples starting from the Temp1 state (Figure 4.61b). $J = 0.169$ Jm^{-2} and $\rho = 6.510^{11}$ m^{-1} were evaluated as optimal for these calculations with such parameters, although modeling results underpredict the size of Laves phase particles starting from the RA state about 12 pct., starting from the Temp3 state about 17 pct. and overpredict the size of precipitates in specimens starting from the Temp1 state about 27 pct.

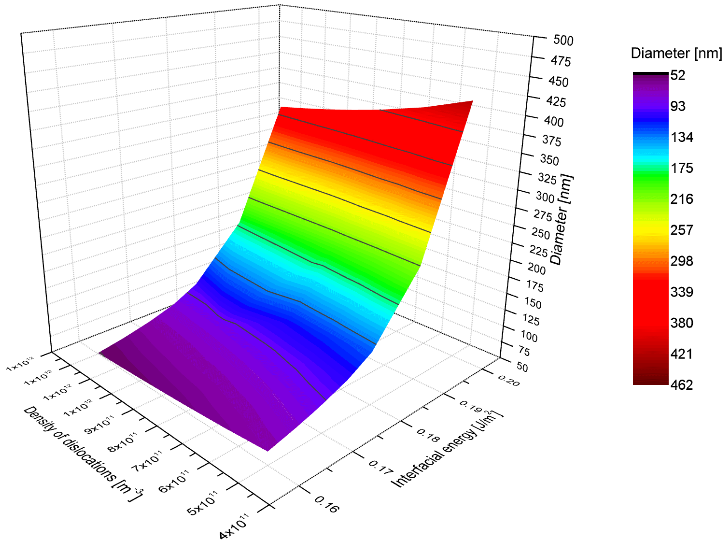

Figure 4.60: Influence of dislocation density σ and interfacial energy γ on predicted size of Laves phase particles in 17Cr1 steel (recrystallized state)

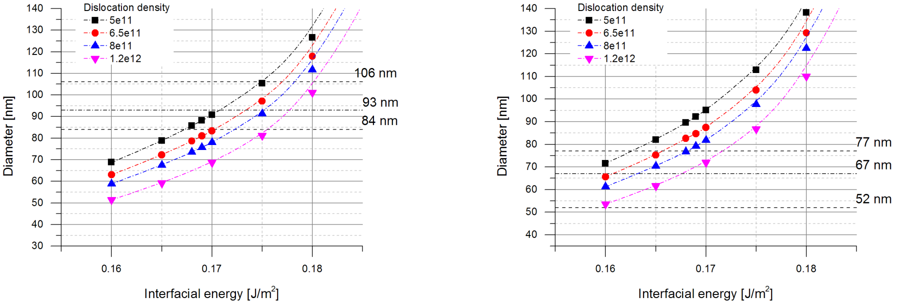

(a) Recrystallization annealed

(b) Temp1

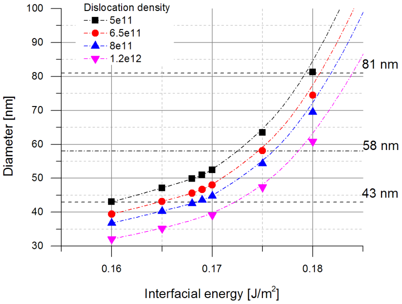

(c) Temp3

Figure 4.61: Influence of interfacial energy and dislocation density on the predicted size of Laves phase particles in 17Cr1 steel in different initial heat treatment states: (a) recrystallization annealed (RA), (b) Temp1 state - RA + 475 °C/5 h, (c) Temp3 state - RA + 540 °C/5 hours

Precipitate evolution modeling was performed in two case studies: The first concerning the influence of heat treatment of 17Cr1 steel, the second one concerning the chemical composition of HiperFer steels starting from the recrystallized state. All the samples were recrystallization annealed at 1075 °C for 15 minutes prior to any further treatment. The evaluation of the dislocation density ρ and interfacial energy γ is described in the previous paragraphs, all the other physical constants used for modeling in TC-Prisma were taken from the TCFE7 and MOBFE2 databases.

A comparison of the observed and modeling results of the heat treatment influence on Laves phase precipitate evolution in 17Cr1 steel is given in Figure 4.62. All the samples were long term annealed at 650 °C. The initial heat treatment states were:

- 17Cr1 - recrystallization annealed (RA, 1075 °C/15 min),
- Temp1 - RA + 475 °C/5 h,
- Temp2 - RA + 510 °C/5 h,
- Temp3 - RA + 540 °C/5 h.

Despite of scatter in the ECD values, the modeling results are in good agreement in case of the Temp2 specimens. The predicted size of precipitates in the Temp3 state is slightly underestimated, but still within the range of scatter. Modeling underestimates the size of precipitates in samples starting from the RA state overestimates it starting from the Temp1 state.

Higher ECD values, formed in samples which were annealed for 1,000 hours, might suggest that particles were coarsening already, but the size of Laves phase particles in the Temp3 creep specimen (650 °C / 100 MPa / 1,542 h) was 73.4±1.7 nm in the head section and 69.7±1.8 nm in the gauge section (Figure 4.48). For this reason it is supposed that the higher ECD values of Laves phase particles after 1,000 hour of annealing result from scatter. Nevertheless, this has to be further proved by long term annealing experiments.

The influence of chemical composition of HiperFer steels on precipitation behaviour of Laves phase precipitates was the second case study where TC Prisma modelling was applied. The comparison of observed and calculated sizes of particles is depicted in Figure 4.63. All samples were in the recrystallized state (1075 °C/15 min) prior to long term annealing. 17Cr2 steel contains an enhanced amount of tungsten. 17Cr3 steel contains the same amount of tungsten as the 17Cr2 material, but features a higher content of Nb. No significant influence of the enhanced tungsten content of the 17Cr2 material on the refinement of Laves phase particles was observed, but a significant refinement of Laves phase precipitates in W- and Nb-enhanced 17Cr3 steel was identified. The Prisma modeling results of 17Cr2 and 17Cr3 steels precipitate development are in strong correlation with experimental observations.

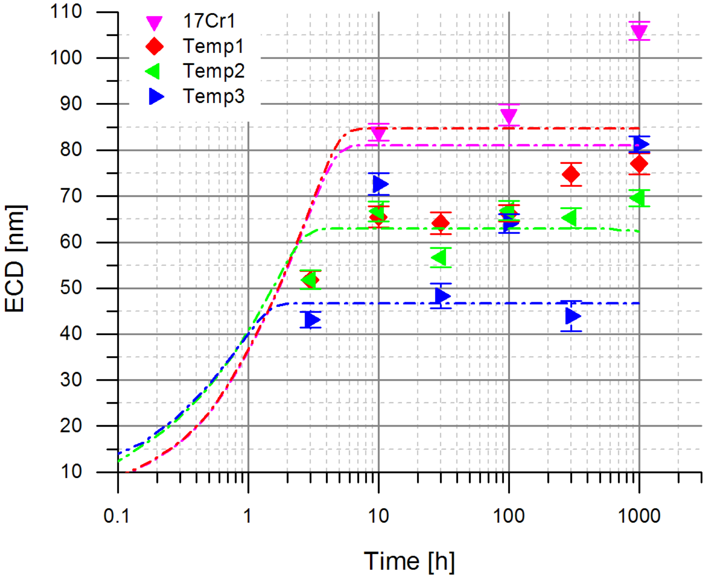

Figure 4.62: Precipitation of Laves phase particles in 17Cr1 steel with different initial heat treatments during long term annealing at 650 °C; comparison of observed (points) and modeled (curves) values

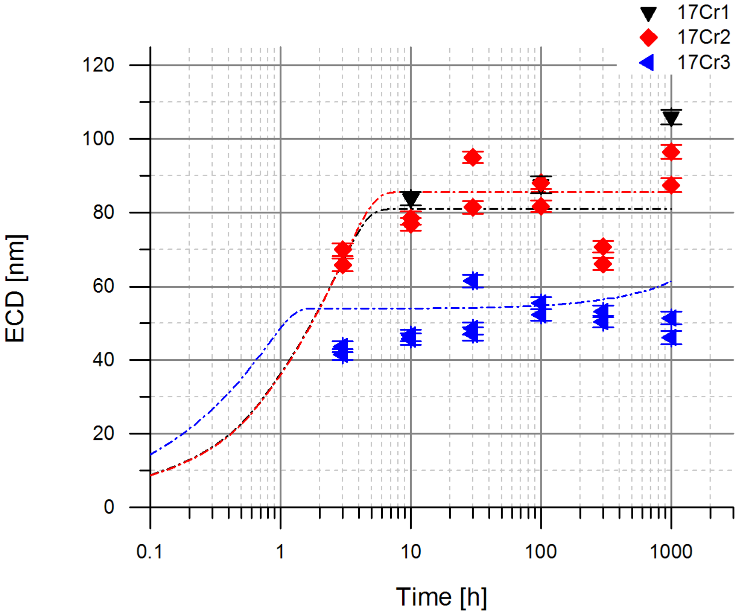

Figure 4.63: Precipitation of Laves phase particles in 17Cr1, 17Cr2, and 17Cr3 HiperFer steels during long term annealing at 650 °C

Chapter 5

Discussion

5.1 Creep properties

The creep properties of HiperFer steels were tested at 650 °C. which is the intended maximum design temperature of new ferritic steels for steam power plant application. The rolled variants of 17Cr_1 steel (Table 3.2) were tested at stresses from 120 down to 70 MPa. The influence of different heat treatments on 17Cr1 steel was tested at 650 °C and 100 MPa. The creep properties of the rolled variants of 17Cr1 steel will be discussed in relation to modern ferritic-martensitic and austenitic steels in the following. The role of the initial thermo-mechanical treatment state creep properties will be presented by three case studies first, and a global overview will be discussed afterwards. The influence of heat treatment on the 17Cr1 steel will be compared with the properties of the 17Cr1_1 steel.

5.1.1 Creep properties of rolled 17Cr1 steel

The creep properties of rolled 17Cr1 material were tested at 650 °C. The experiments in the stress range from 100 to 120 MPa are finished, while the experiments at 70 MPa are still in progress (subsection 4.5.1). Time to rupture data of the 17Cr1_1, 17Cr1_2, and 17Cr1_3 rolling variants are compared to the properties of 9 wt.% Cr steels - P91 [54] and P92 [53], the strongest 12 wt.% Cr creep resistant steel - VM12 [60], and two high Cr austenitic steels - 800 H-B [61] and 316 [62]. The creep strength of the rolled variants of the 17Cr1 steel is extrapolated by a polynomial of 2nd order down to 90 MPa (Figure 5.1).

For stress levels equal and below 110 MPa, the times to rupture of all three rolling variants are longer than for P91 steel (Figure 5.1). The creep strength of the 17Cr1_3 material is close to the creep strength of P92 steel. With respect to the finished creep tests, it is expected that the influence of the initial rolling state on the creep strength of 17Cr1 materials diminishes with the decrease of applied stress and time to rupture. The running experiments at 70 MPa are expected to terminate close to or beyond the P92 level for all the 3 rolled 17Cr1 materials.

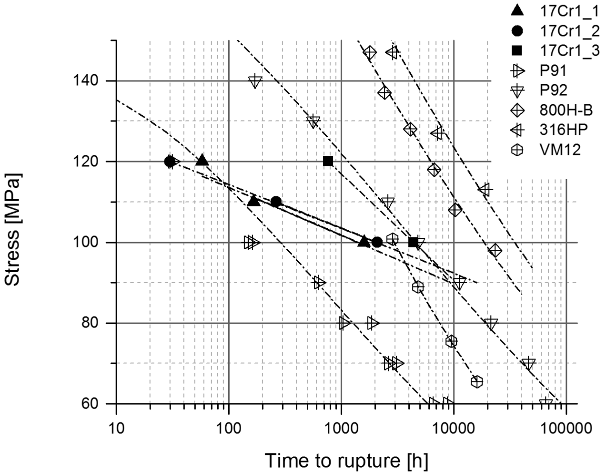

Figure 5.1: Creep strength of rolled 17Cr1 steel at 650 °C in comparison to 9-12 wt% Cr ferritic-martensitic, and austenitic steels

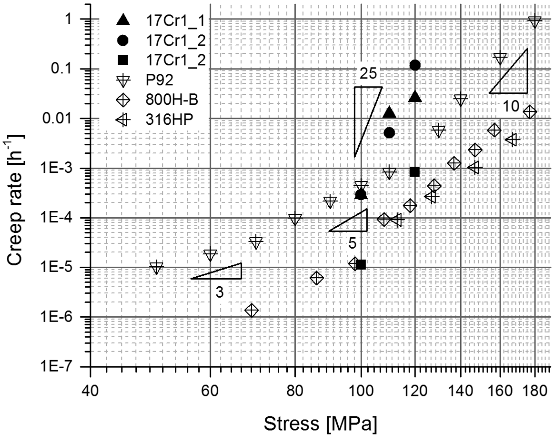

Figure 5.2: Creep strength of rolled 17Cr1 steel at 650 °C in comparison to 9-12 wt% Cr ferritic-martensitic, and austenitic steels

The creep rate stress exponents do not have a uniform value, but differ from material to material, and they are dependent on applied stress as well (cf. section 2.2.2). Values close to 1 are typical for diffusion controlled creep, 3–5 to dislocation controlled creep, and above 7 is commonly referred as the power law break down [16, 32]. The stress exponents of oxide dispersion strengthened materials range from appr. 15 up to several hundreds [23] (Figure 5.3).
The stress exponent of the rolled 17Cr1 materials is appr. 25 in the stress range from 100 up to 120 MPa (Figure 5.2), while the stress exponent of P92 steel is in the range of 5 to 10, and about 5 for the austenitic 800H-B and 316HP steels. High values of stress exponent n_0 and significant increase of lifetime with modest decrease of applied stress (Figure 5.1) count creep performance closer to oxide dispersion strengthened materials than to standard creep resistant steels and nickel based alloys [23, 63–65].

5.1.2 Influence of tempering on the creep strength of 17Cr1 steel

Time to rupture of the recrystallization annealed 17Cr1 at 650 °C and 100 MPa was 386 h whereas time to rupture of the rolled 17Cr1_1 material was 1594 h. This represents appr. five-fold longer creep life of the material with enhanced initial dislocation density: the presence of dislocations has a positive influence on the creep strength of Hiperfer steels in two ways: First, deformation strengthening, which is effective in the early stages of creep (cf. subsection 2.2.1)

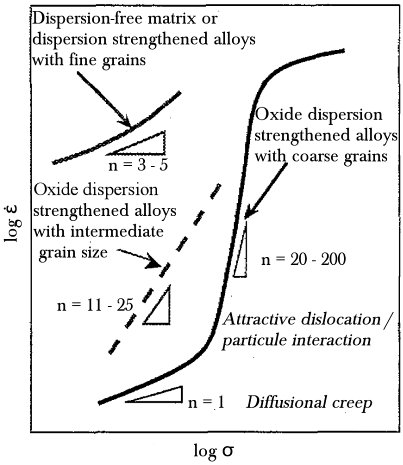

Figure 5.3: Variation of stress exponent in steels with and without oxide dispersion strengthening [23]

and second, accelerated formation of precipitates (cf. subsection 4.4.1). The influence of tempering below application temperature on the creep properties and microstructure development of recrystallized 17Cr1 steel was presented in subsection 4.4.3 and section 4.5.2.

The time to rupture of recrystallized 17Cr1 material was more than 4 times shorter than that of the rolled 17Cr1_1 material (Figure 5.4). The Temp1 specimen ruptured after 152 h, what stands for a loss in life time more than 50 % in comparison to the recrystallization annealed 17Cr1 material, while the Temp2 specimen exhibited a lifetime of 309 h. The Temp3 specimen ruptured after 1542 h, representing four-fold longer lifetime than in case of the recrystallized 17Cr1 material, and a comparable lifetime to the rolled 17Cr1_1 material.

The evolution of total deformation during creep is shown in Figure 5.5. The 17Cr1_1 material exhibited significantly smaller deformation within the first 5 h of creep than the recrystallized and/or tempered specimens. The initial deformation of recrystallized 17Cr1 material was comparable to the Temp1 specimen, whereas the Temp2 and Temp3 specimens exhibited initial deformation comparable to the rolled 17Cr1_1. This suggests that tempering at 510, and 540 °C formed suitable particle microstructures to hinder initial deformation effectively. Obviously the size and density of the Laves phase precipitates in the Temp1 specimen was less effective.

The influence of heat treatment on microstructure evolution of HiperFer steel was successfully modeled by the commercial software TC Prisma utilizing the databases TCFE7 and MOBFE2 (cf. subsection 4.6.2). Observed and modeled variation of particle size diameters of recrystallized 17Cr1, Temp1, Temp2, and Temp3 materials is presented in Figure 5.18a.

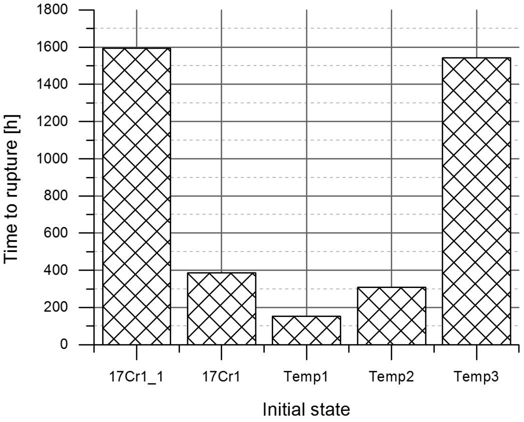

Figure 5.4: Time to rupture of 17Cr1 steel in different initial states - rolled 17Cr1_1, recrystallized (1075 °C/15 min) 17Cr1, and tempered Temp1 (1075 °C/15 min + 475 °C/5 h), Temp2 (1075 °C/15 min + 510 °C/5 h) and Temp3 (1075 °C/15 min + 540 °C/5 h)

Thermodynamic calculations predict minimal growth of Laves phase particles in 17Cr1 steel tempered at 475 °C for 5 h (Temp1 material) and the most pronounced growth of particles is calculated for the Temp3 material, tempered at 540 °C (Figure 5.7b). Calculated distributions of particles in the Temp1, Temp2, and Temp3 materials after 5h tempering at given tempering temperatures are plotted in Figure 5.7b. The dominant amount of Laves phase particles after tempering at 475 °C for 5 hours (Temp1) is below 0.5 nm, and thus close to the critical radius for precipitation. A significantly bimodal size distribution of Laves phase particles is predicted in the material tempered at 510 °C for 5 h (Temp2), where the first peak is close to the critical radius and the second to 2 nm. The size distribution in the material tempered at 540 °C for 5 h (Temp3) is still supposed to be bimodal, but the majority of particles has size larger than 4 nm.

The incubation period of precipitation can be mitigate by proper heat treatment [6]. If precipitation starts from a random solid solution, a standard incubation period prior to the formation of supercritical clusters was observed. On the contrary, if precipitation starts in a system that was annealed just above the solubility limit, the supercritical clusters started to form immediately (cf. section 2.1.2).

Likewise, nucleation may still have been in progress (at 475 °C) when precipitation (at 650 °C) was started from the Temp1 state, modeling results suggests that majority of precipitates are in growth regime already if precipitation (at 650 °C) starts from the Temp3 state (tempering at 540 °C). The result is faster formation of strengthening precipitates after "high temperature"

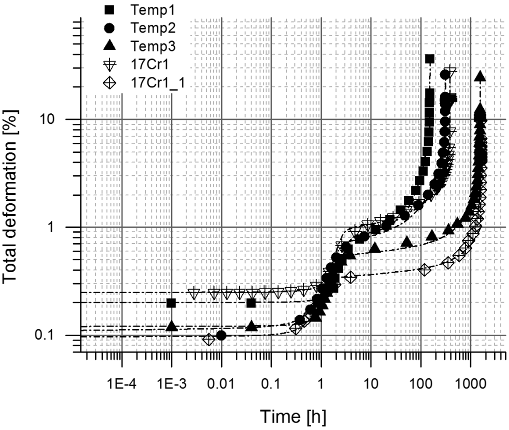

Figure 5.5: Evolution of creep deformation of 17Cr1 steel in different initial states - rolled 17Cr1_1, recrystallized (1075 °C/15 min) 17Cr1, and tempered Temp1 (1075 °C/15 min + 475 °C/5 h), Temp2 (1075 °C/15 min + 510 °C/5 h) and Temp3 (1075 °C/15 min + 540 °C/5 h)

tempering at 540 °C. It may be furthermore expected that the nuclei in the Temp1 state coagulate and coarsen at the beginning of annealing (at 650 °C), what would explain the larger ECD values (5.18a) after Temp1 tempering in comparison to Temp3 tempering.

The particles that were formed during tempering of tensile specimens prior to creep testing are too small to be observed by HRSEM, but the lower intrinsic deformation measured at the Temp2 and Temp3 specimens suggests the presence of particles being effective enough to hinder initial deformation. HiperFer steel is an age hardenable alloy where microstructure evolves during testing (the initial microstructure of 17Cr1 steel was presented in section 4.2, the evolution of microstructure was discussed in section 4.4). For this reason, the variation in creep deformation evolution of tempered 17Cr1 specimens can be attributed to differences in the microstructure evolution kinetics and properties of the Laves phase particles morphology. No significant variation was observed in the beginning of the standard primary creep in all 3 tempering variants, but a clear difference in increase of deformation during primary creep (Figure 5.5 is present, Figure 4.43). The strength in primary stage of creep is supposed to be influenced by the size of precipitates, with bigger particles being less effective in Orowan strengthening (cf. subsection 2.2.1).

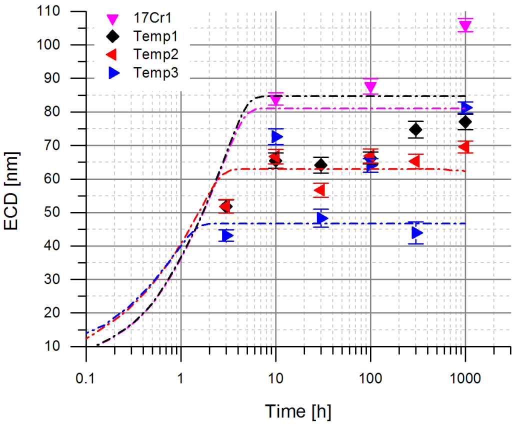

Figure 5.6: Observed (points) and modeled (curves) change of ECD of Laves phase particles in HiperFer 17Cr1 steel in different initial states: recrystallization annealed 17Cr1 (RA, 1075 °C/15 min), and tempered Temp1 (RA+475 °C/5 h), Temp2 (RA+510 °C/5 h), and Temp3 (RA+540 °C/5 h)

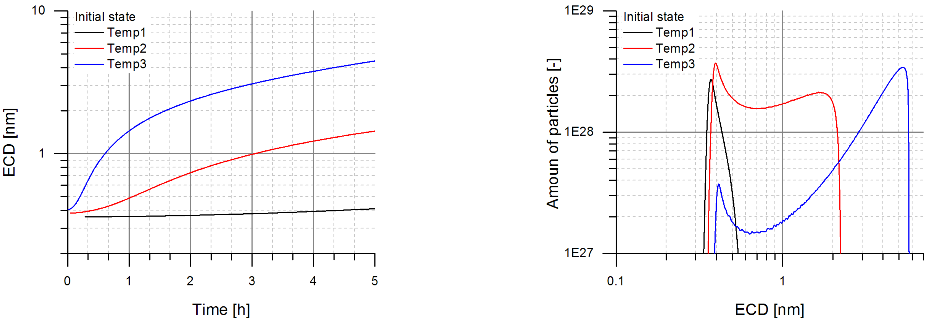

(a)

(b)

Figure 5.7: (a) Evolution of ECD and (b) size distribution of particles after 5 h of tempering at different temperatures: Temp1 - 475 °C, Temp2 - 510 °C, Temp3 - 540 °C

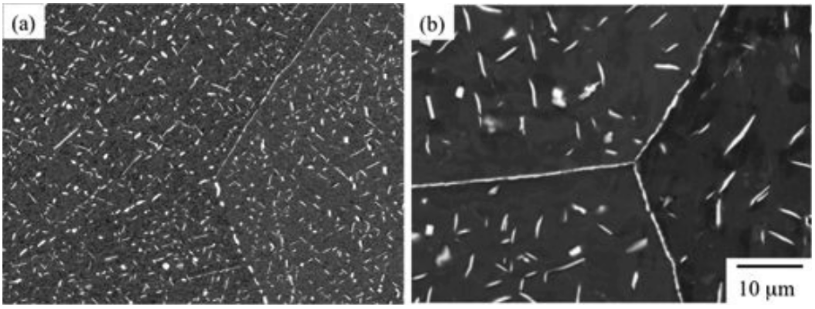

Figure 5.8: Microstructures of model austenitic steels after annealing at 800 °C/1,200 h: (a) original ST700, (b) modified BST700 [24]

5.1.3 The role of grain boundary precipitation on the creep properties of 17Cr1 steel

Traditionally, the decoration of grain boundaries by dense and relatively coarse precipitates is considered being detrimental with respect to creep properties, ductility and resistance against corrosive attack [4, 40, 66]. The formation of precipitates is connected with the presence of depleted areas in close vicinity. This area can be susceptible to corrosive attack if the matrix is depleted in chromium (e.g. in case of formation of (Fe,Cr) σ-phase or chromium carbides), or the matrix around coarse particles can be depleted in elements ensuring solid solution strengthening (e.g. depletion of W around coarse Fe_2W Laves phase particles in ferritic-martensitic steels). The grain boundary - precipitate interface can represent a suitable place for the formation of cavities when the soft matrix is being deformed around a hard particle [16]. In contrary, hard particles represent obstacles for grain boundary sliding [16, 67]. The free length of sliding decreases with increasing occupation of grain boundaries.

A positive influence of decoration of grain boundaries by dense precipitation of Laves phase particles was demonstrated by Takeyama at al. [24,68]. Takyeama used two carbon free austenitic steels in his study; the first one ST700 with a nominal composition of (at%) Fe-20Cr-(30-35)Ni-(2-2.5)Nb and BST700 with the addition of 0.03 at% B to promote precipitation of Laves phase particles at grain boundaries. The boron doped BST700 steel exhibited a significantly coarser microstructure after annealing at 800 °C for 1,200 h in comparison to ST700 steel (Figure 5.8). Furthermore the grain boundaries in BST700 steel were fully covered, whereas less than 50% of the grain boundaries were covered by Laves phase precipitates in ST700 steel. The positive influence of grain boundary precipitation on decrease of the minimum creep rate is shown in Figure 5.9, where minimum creep rate data are plotted over the area fraction on grain boundaries ρ. The minimum creep rate of experimental austenitic steels decreases rapidly if more than 80 pct. of grain boundaries are decorated by the Laves phase precipitates.

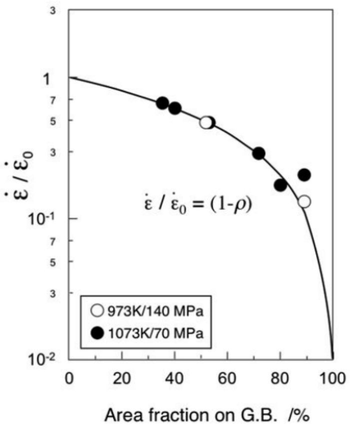

Figure 5.9: Decrease of minimum creep rate with increased grain boundary precipitation in Fe20Cr30Ni2Nb austenitic heat resistant steels [24]

Traditionally, the ST700 would be expected to have better creep properties than the BST700 material, because of denser and finer precipitation of Laves phase particles (cf. subsection 2.2.1). In contrast, BST700 steel ruptured after 16,721 h, ST700 steel after 4,594 in testing at 700 °C and 120 MPa. Takeyama [24] thus observed a significant increase of creep rupture life if grain boundaries are covered by more than 80%.

The precipitation rates in the matrix, at dislocations, grain boundaries etc. vary with changes in temperature [5, 7]. This phenomenon was applied to design a heat treatment to decorate the grain, but to avoid precipitation in the grain interiors (cf. subsection 4.4.4). The first heat treatment (marked as HTT1) consisted of recrystallization annealing (1075 °C/15 min) and subsequent 15 minute tempering at 800 °C. Recrystallization annealing (1075 °C/15 min) and tempering at 850 °C for 15 minute was applied in case of HTT2 heat treatment. Microstructures of post mortem head sections of creep specimens are given in Figure 5.11. The grain boundaries of the HTT1 specimen were densely decorated by relatively coarse Laves phase particles and a fine, homogeneous dispersion was observed in the grain interiors. Particle free boundary zones alongside grain boundaries was encountered (Figure 5.11a). Dense precipitation of coarse Laves phase particles was present in the HTT2 specimen (Figure 5.11b) but, unlike the HTT1 specimen, sparse and coarse Laves phase particles in grain interiors were observed, too.

Creep rate over creep deformation curves of high temperature tempered HTT1 and HTT2 specimens, and the rolled 17Cr1_1 specimen, tested at 650 °C and 100 MPa, are plotted in Figure 5.12. No significant minimum was observed in the creep rate curve of the HTT2 specimen (t_r=22 h), but the creep rate continuously increased from the beginning of the experiment. This behaviour

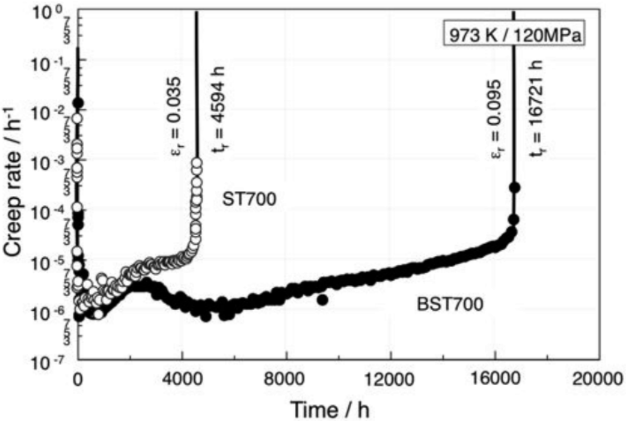

Figure 5.10: Creep rate curves of solution treated ST700, and boron doped BST700 austenitic steels [24]

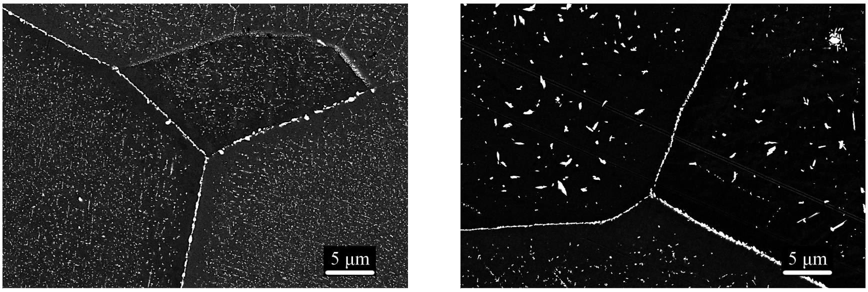

(a) HTT1, Head section

(b) HTT2, Head section

Figure 5.11: Head section microstructures of ruptured high temperature tempered 17Cr1 specimens; (a) HTT1, tempering 800 °C/15 min, t_r = 1,304 h, (b) HHT2, tempering 850 °C/15 min, t_r = 22 h

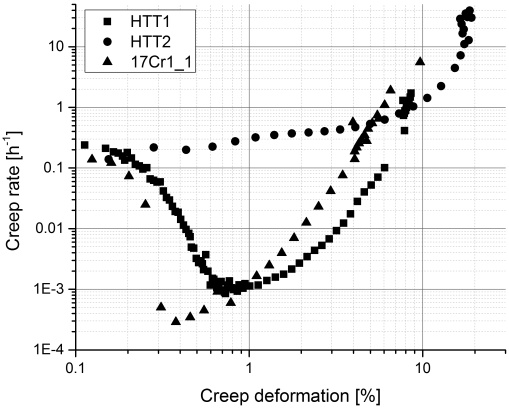

Figure 5.12: Creep rate curves of 17Cr1 materials in different initial thermo-mechanical treatment states: HTT1 - RA + 800 °C/15 min, HTT2 - RA+850 °C/15 min, rolled 17Cr1_1

is typical for a slow rate tensile experiment, rather than for a creep test. The creep rate curves of the HTT1 and 17Cr1_1 specimen consist of all the three stages of creep life - primary, secondary and tertiary, but differ significantly. The minimum creep rate of the HTT1 specimen was $1 \cdot 10^{-3}$ h^{-1} (after 0.7% of creep deformation), the 17Cr1_1 specimen reached a minimum creep rate of $3 \cdot 10^{-3}$ h^{-1} (after 0.37% creep deformation). The increase in creep rate with increasing creep deformation of the rolled17Cr1_1 specimen was practically linear in the tertiary stage. The HTT1 specimen exhibited a slight increase in creep rate in the range from 0.7 to 2 % of creep deformation and a strong acceleration at higher values of creep deformation (Figure 5.12). A linear increase of creep rate with increasing creep deformation is typical for grain boundary sliding, refered as superplasticity or grain flow [29, 69]. The deviation from linearity as was described hereinabove can be attributed to the deterioration of grain boundary flow as described by Yoo [67] and Takyeama [24].

5.1.4 Overview of creep properties

The influence of different initial thermo-mechanical treatment states on the creep properties of 17Cr1 HiperFer steel was discussed in the previous sections. Samples with significantly different initial thermo-mechanical treatment exhibited comparable times to rupture at 650 °C and 100 MPa - rolled 17Cr1_1 material (subsection 5.1.1), low temperature tempered Temp3 (subsection 5.1.2), and high temperature tempered HTT1 sample (subsection 5.1.3).

Creep properties are commonly presented in graphical forms like in Figure 5.1, where time to rupture of a material is plotted over stress at different temperatures. Such representation requires systematic testing of samples of the same initial state, where tests are conducted at different stress and temperature levels. All the experiments in the presented study were performed at 650 °C, just the rolled samples were tested at different stress levels. For this reason, a time to rupture diagram is considered to be not the most suitable representation for the evaluation of thermo-mechanical treatment influence on the creep properties of 17Cr1 HiperFer steel. Another typical representation of creep results is so colled Monkman-Grant relation [32] which is given by

$$\begin{gathered} \dot{\epsilon}^{m} t_r = k_{mg} \\ log(\dot{\epsilon}) = \frac{1}{m} log\left(\frac{k_{mg}}{t_r}\right) \end{gathered} \tag{5.1}$$

where $\dot{\epsilon}$ is the minumum creep rate,
t_r is the time to rupture,
m is a constant, and
k_{mg} is a constant.

The results of all the creep tests (except of the HTT2 test) performed in this thesis as a graphical representation of the Monkman-Grant relationship are given in Figure 5.13. All the experimental results, despite of different testing conditions and different initial thermo-mechanical treatment state, fall to a single line. This suggests that the mechanisms controlling creep were the same for all the tests.

Abe in his analysis of P91 creep data [70] suggested that there is a linear relationship of time to rupture and time to minimum creep rate. The Monkman-Grant relationship can by applied to time to minimum creep rate as well, like given in Figure 5.14. Time to rupture and time to minimum creep rate is given a in double logarithmic plot in Figure 5.15. The time to minimum creep rate can be than expressed as

$$log(t_{\dot{\epsilon}}) = a \cdot log(t_r) + b \tag{5.2}$$

where $t_{\dot{\epsilon}}$ is time to minimum creep rate, t_r is time to rupture, and a and b are regression constants. The values of the regression constants are $a = 0.216$ and $b = 1.044$. This means that almost 80 pct. of creep life of 17Cr1 steel, despite of varieties in the initial treatment states and testing conditions, lies within short secondary and mostly the tertiary creep regime. The correlation is strong over a broad range of life time values (Figure 5.15).

Plasticity properties of engineering materials play an important role in creep related applications. A sufficient duration of tertiary creep, sufficient creep rupture deformation is necessary to detect evolving damage prior to catastrophic accidents. Rupture deformation values of all the creep tests presented in this thesis are given in Figure 5.16.

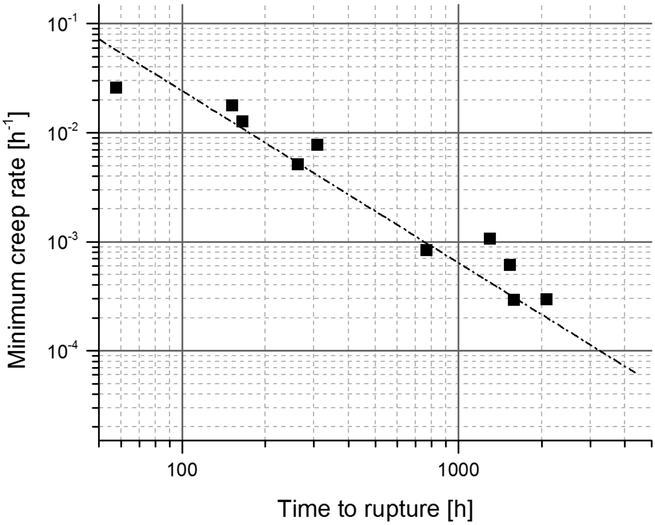

Figure 5.13: Relation of time to rupture and minimum creep rate of 17Cr1 creep experiments

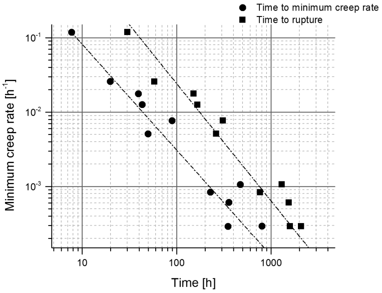

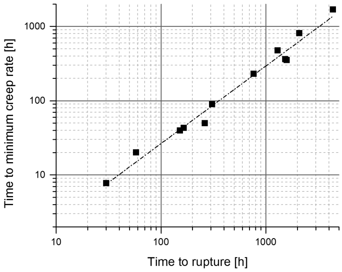

Figure 5.14: Monkman-Grant graph for time to rupture and time to minimum creep rate

Figure 5.15: Relation of time to rupture to time to minimum creep rate

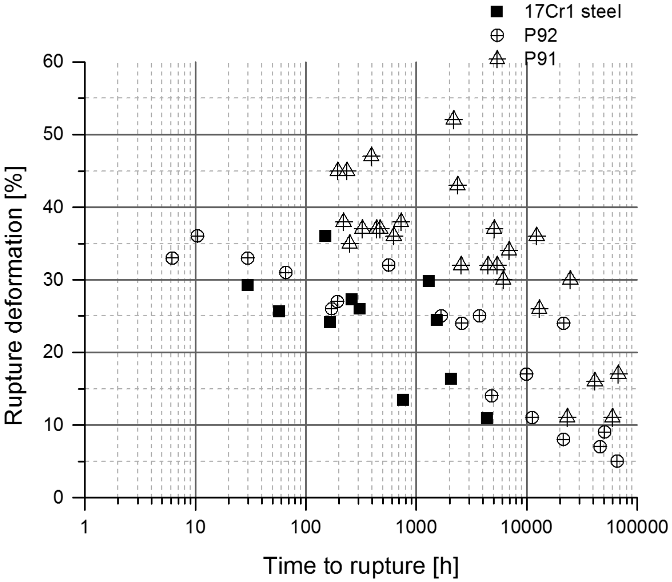

Figure 5.16: Rupture deformation of all the 17Cr1 creep specimens in comparison to P91 and P92 steels

Creep rupture deformation of the rolled 17Cr1 material materials is lower than that of P92 steel (cf. Figure 4.35), but creep rupture deformation of the thermally treated creep specimens achieved values comparable to P92. Rupture deformation of the low temperature tempered Temp3 specimen with a lifetime of 1,542 h was 24 pct. and the high temperature tempered HTT1 specimen with lifetime of 1,304 h was 29%, and thus well above the creep rupture deformation of P92 steel at, whereas the expected deformation of samples with lifetimes of 1,000 to 2,000 h is around 20 %.

Microstructures from the necked gauge proportions of the rolled 17Cr1_1, the low temperature tempered Temp3, and the high temperature tempered HTT1 specimens are presented in Figure 5.17. All the specimens were tested at 650 °C and 100 MPa and, despite of different initial thermo-mechanical treatment state, exhibited similar life time in the range from 1,300 up to 1,600 h. Creep cavities were found in the grain interiors (marked by dashed red circles) and at the grain boundaries (marked by green circles). Cavities in the grain interiors were formed on (Cr,Mn) oxides (marked by blue arrows). Particle free zones were observed at the grain boundaries in the high temperature tempered specimen only (Figure 5.17c).

5.2 Modeling of particle size evolution

Interfacial energy represents a quantity that compensates broken atomic bonds between matrix and precipitate [5]. It has low values for precipitates with high coherency to the matrix and it reaches high values for incoherent precipitates.

The precipitation process is strongly influenced by the value of interfacial energy γ. The critical diameter of a precipitate at the beginning of precipitation is given by the equation [71]:

$$r^* = \frac{2\gamma}{\Delta G_V} \tag{5.3}$$

where $\gamma(t)$ is the interfacial energy,
ΔG_V is the chemical volume free energy change driving nucleation.

Interfacial energy plays a key role during diffusion controlled growth and coarsening of precipitates. The size of a particle, which is in the diffusion controlled regime can be calculated by the equation [5, 7]:

$$(r)^3 - r_0^3 \approx D\gamma X_c t \tag{5.4}$$

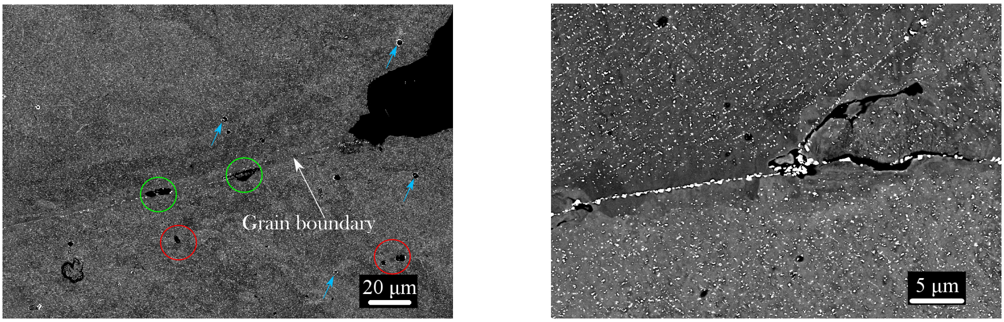

(a) rolled 17Cr1_1

(b) low temperature tempered Temp3 specimen

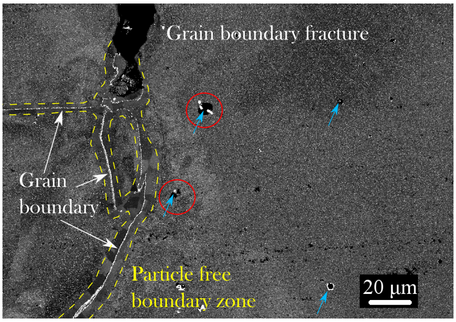

(c) high temperature tempered HTT1 specimen

Figure 5.17: Microstructures of the fracture areas of 17Cr1 creep specimens with different initial thermo-mechanical treatment state tested at 650 °C and 100 MPa: (a) rolled 17Cr1_1, $t_r = 1,594\ h$; (b) low temperature tempered Temp3 (1,075 °C/20 min + 540 °C/5 h) , $t_r = 1,542\ h$; (c) high temperature tempered HTT1 (1,075 °C/20 min + 800 °C/15 min), $t_r = 1,304\ h$

where	r	is the mean radius of particles at time t,
	r_0	is the mean radius of particles at the beginning of growth/coarsening,
	D	is the diffusion coefficient,
	γ	is the interfacial energy, and
	X_e	is the solutibility of very large particles

It is difficult to obtain the value of interfacial energy experimentally, because it is not possible to measure the quantity directly [5]. In coarsening experiments only the product of interfacial energy γ and diffusivity D can be be obtained (Equation 5.4. The values of Laves phase precipitates interfacial energy γ in a ferrite matrix are reported to range from 0.331 to 0.85 Jm^{-2} [58, 72–74]. Assuming constant, high values of γ during the whole precipitation process leads to critical radii (cf. subsection 2.1.2) in the range of ones [58] and tens [74] of nanometers. These values are in contradiction with the classical nucleation theory, which assume the critical particle size in the range of Å, i.e. one or two orders of magnitude lower [75]. A critical radius in the range of Å means, that a precipitate nucleus is formed by several atoms, which have sufficient freedom of arrangement to obtain a minimum interfacial energy [75]. On the other hand, a particle that grows and coarsens is typically composed by hundreds and thousands of atoms, properly organized into crystallographic structures. Large variations of interfacial energy γ were reported eg. for Al_3Si precipitates, where it reaches values from $0.094\,\mathrm{Jm}^{-2}$ in the early stages of precipitation to $0.2\,\mathrm{Jm}\ ^{-2}$ calculated from coarsening experiments [75].

The values of interfacial energy γ and dislocation density σ were optimized for the evaluation of microtructural evolution of the HiperFer steel by TC-Prisma (cf.subsection 4.6.2). Optimum modeling results were obtained by applying $\gamma = 0.169\ \mathrm{Jm}^{-2}$ and $\sigma = 6.5\ 10^{11}\mathrm{m}^{-1}$. A comparison of modeled and measured sizes of Laves phase particles during annealing experiments at 650 °C (up to 1,000 h) is given in Figure 5.18. Differences between the modeled and observed results of heat treated 17Cr1 steel (Figure 5.18a), but the observed sizes of particles of the HiperFer steels with differing chemical compositions are calculated closely (Figure 5.18b).

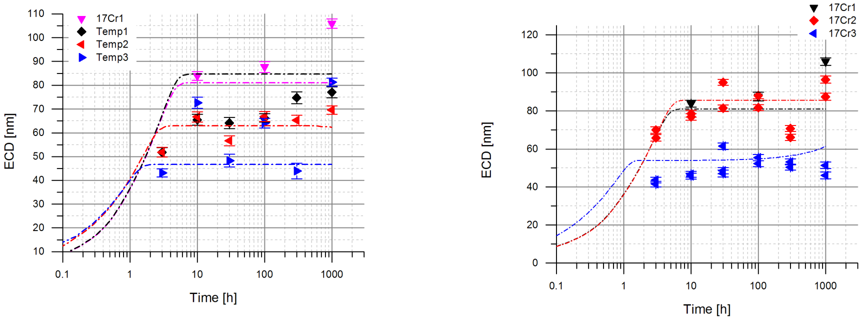

(a)

(b)

Figure 5.18: Simulated and measured size of particles of (a) 17Cr1 steel with different heat treatment and (b) HiperFer steels with differing chemical compositions

Chapter 6

Conclusions and outlook

The presented work focuses on the creep properties of HiperFer steel at 650 °C. HiperFer steel is age hardenable steel. The microstructure of such materials develops during high temperature exposure. The influence of different initial thermo-mechanical treatment states on microstructure development during isothermal annealing at 650 °C and on mechanical properties was studied.

Creep strength of the rolled materials increased with increasing rolling deformation. Creep properties were influenced not only by work hardening, resulting from different rolling procedures. Furthemore, accelerated precipitation, driven by enhanced dislocation density, was observed. The creep strength of 17Cr1_3 steel at 650 °C is comparable to the strongest 9 wt% Cr ferritic-martensitic steel P92 and is higher in comparison to the strongest 12 wt% Cr ferritic-martensitic steel VM12. The positive influence of the enhanced dislocation density on creep strength decreases with the decrease of applied stress.

The life time of a recrystallized material was five to ten times shorter than that of the rolled materials. The reduction of creep life resulted from the absence of work hardening and slower precipitation kinetics in the recrystallized material. Creep strength of recrystallized material was restored up to the level of the rolled one by two significantly different heat treatments: A heat treatment at 540 °C accelerates the formation and refines the morphology of Laves phase particles in the grain interiors. A creep sample annealed at 540 °C prior to creep testing exhibited smaller deformation during sigmoidal creep, and a slower increase of deformation during primary creep. Combination of dense precipitation of coarse Laves phase particles on grain boundaries and fine, dense precipitation of Laves phase particles in the grain interiors resulted from short term annealing at 800 °C prior to creep testing. This heat treatment caused retardation of grain boundary sliding in the later periods of creep with sufficient Orowan strengthening.

The influence of different chemical compositions as well as the role of the long term annealing at temperatures below 650 °C on precipitation behaviour was successfully modeled by TC-Prisma. A stochastical model describing the development of creep deformation was introduced. A simple lifetime model based on the relation of time to rupture and time to minimum creep rate was presented. Creep tests of 17Cr1 HiperFer steel lasted from 30 up to 4,400 h. A strong correlation between time to rupture and the time to minimum creep rate suggests, that the mechanisms controlling creep properties were the same for all the presented experiments.

New HiperFer melts with increased content of Nb and W are supposed to exhibit higher creep strength in comparison to the 17Cr1 material. Enhanced content of W is supposed to have a positive influence on solid solution strengthening and to enhance total fraction of strengthening Laves phase particles, Nb is supposed to refine the size of Laves phase particles.

Heat treatment of HiperFer steel in the recrystallized state can have both, positive but detrimental effect on the creep strength as well. A beneficial influence of annealing at 500 °C on mechanical properties of E-beam welds was presented in a previous work. The influence of different heat treatments on creep properties of arc weldments is a subject of ongoing research.

Modeling results of TC Prisma software are significantly influenced by values of physical parameters. The influence of dislocation density and interfacial energy on the modeled size of Laves phase particles was discussed in the thesis. Modeled and observed precipitates development of 17Cr1 steel in the different initial thermo-mechanical state correlated well. Strong correlation of modeled and observed precipitates development in 17Cr1, 17Cr2, and 17Cr3 steels in the recrystallized state prior to precipitation was recognized. Long term isothermal annealing experiments at different temperatures in range from 600 to 900 °C are planned to verify the TC Prisma modeling.

Creep modeling presented in this thesis has statistical-stochastical nature. Such modeling approach is not able to evaluate the influence of particular thermo-mechanical parameters, e.g. dislocation density, grain size, grain orientation, microstructural development etc., but it is not expensive in terms of microstructural observations and analysis. A statistically significant testing matrix is necessary to verify statistical-stochastical models for successful interpolation, but mainly for extrapolation. Long term creep tests of 17Cr1 steel, and materials with enhanced content of W and Nb at different temperatures and stress levels are planned. The expected longest creep tests are supposed to reach lifetime of 30-50,000 hours.

Bibliography

[1] Robert Priddle. World energy outlook 2011. Technical report, International Energy Agency, 2014. ISBN 978 92 64 12413 4.

[2] 2014 key world energy statistics. Technical report, International Energy Agency, 2014.

[3] Peter Lemens. Power plant technology. Z-ultra short course, Tbilisi, Georgia, 2014.

[4] Reza Abbaschian, Lara Abbaschian, and Robert E. Reed-Hill, editors. *Physical Metallurgy Principles,*. Cengage Learning, Stamford,, four edition, 2009.

[5] Alexander Nebylov and Ernst Kozeschnik. *Modeling Solid-State Precipitation.* Momentum Press, first edition, 2012.

[6] F. Soisson and G. Martin. Monte carlo simulations of the decomposition of metastable solid solutions: Transient and steady-state nucleation kinetics. *Phys. Rev. B*, 62:203–214, Jul 2000.

[7] David A. Porter. *Phase transformations in metals and alloys.* Chapman and Hall, Amsterdam, second edition, 1992.

[8] C. N. R. Rao, A Müller, and A. K. Cheetham, editors. *Nanomaterials Chemistry: Recent Developments and New Directions.* Wiley-VCH Verlag GmbH & Co, first edition, 2007.

[9] John A. Wert, E. R. Parker, and V. F: Zackay. Elimination of precipitate free zones in an fe-nb creep_resistant alloy. *Metallurgical transaction A*, 1979.

[10] Paolo Galimberti, Sabine Lay, and Annie Antoni-Zdziobek. Laves phase formation in the Fe2018W alloy annealed at 800 °C. In Yves Bréchet, Emmanuel Clouet, Alexis Deschamps, Alphonse Finel, and Fréddéric Soisson, editors, *Phase Transformations in Inorganic materials (PTM)*, 2010.

[11] Fujio Abe, Torsten-Ulf Kern, and R. Viswanathan. *Creep-resistant steels.* Woodhead Publishing, first edition, 2008.

[12] Harold J. Frost and M. F. Ashby, editors. *Deformation-Mechanism Maps: The Plasticity and Creep of Metals and Ceramics.* Pergamon Press, Amsterdam, first edition, 1982.

[13] Kouichi Maruyama, Kota Sawada, and Jun ichi Koike. Strengthening mechanisms of creep resistant tempered martensitic steel. *ISIJ International*, 41(6):641–653, 2001.

[14] K. Yagi, G. Merckling, T.U. Kern, H. Irie, and Warlimont, editors. *Creep Properties of Heat Resistant Steels and Superalloys.* Springer, first edition.

[15] B. Wilshire and R. W. Evans. *Creep Behaviour of Crystalline Solids.* Pineridge Press Limited, first edition, 1985.

[16] Josef Čadek. *Creep in metallic materials.* Elsevier Science Publishers B. V., first edition, 1988.

[17] H. Ghassemi-Armaki, R.P. Chen, K. Maruyama, and M. Igarashi. Contribution of recovery mechanisms of microstructure during long-term creep of gr.91 steels. *Journal of Nuclear Materials*, 433(1–3):23 – 29, 2013.

[18] R.P. Chen, H. Ghassemi Armaki, K. Maruyama, and M. Igarashi. Long-term microstructural degradation and creep strength in gr.91 steel. *Materials Science and Engineering: A*, 528(13–14):4390 – 4394, 2011.

[19] V. Sklenicka, K. Kucharova, M. Svoboda, L. Kloc, J. Bursik, and A. Kroupa. Long-term creep behavior of 9–12%Cr power plant steels. *Materials Characterization*, 51(1):35–48, 2003.

[20] Hilmar Kjartansson Danielsen and John Hald. Influence of z-phase on long-term creep stability of martensitic 9 to 12 % Cr steels. *VGB PowerTech*, 5:68–73, 2009.

[21] Fujio Abe. Effect of fine precipitation and subsequent coarsening of Fe2W laves phase on the creep deformation behavior of tempered martensitic 9Cr-W steels. *Metallurgical and Materials Transactions A*, 36(2):321–332, 2005.

[22] R. W. Evans and B. Wilshire. *Creep of Metals and Alloys.* The Institute of Metals, first edition, 1985.

[23] C. Zakine, C. Prioul, and D. François. Creep behaviour of ods steels. *Materials Science and Engineering: A*, 219(1–2):102 – 108, 1996.

[24] Masao Takeyama. Novel concept of austenitic heat resistant steels strengthened by intermetallics. *Materials Science Forum*, 539-543:3012–3017, 2007.

[25] Steve Osgerby. Materials R&D requitements for fossil-fuelled steam plant. Energy materials - Meeting the Challange, Loughborough University, UK, 2008.

[26] Mike Spindler. *ECCC recomendations - volume 5.* 2013.

[27] Bernd Kuhn. Development of high chromium ferritic steels strengthened by intermetallic phases. *Material science and engineering A*, 2014.

[28] Bernd Kuhn. Microstructural evolution and creep strenght of High Performance Ferritic (HiperFer) steels. In *3rd International ECCC - Creep & Fracture Conference*, 2014.

[29] Jaroslav Pluhař, Anton Puškár, Jaroslav Koutský, Karel Macek, and Václac Beneš. *Physical metalurgy and limit states of materials (in czech)*. SNTL, first edition, 1987.

[30] J. W. Martin, R. D. Doherty, and B. Cantor. *Stability of Microstructure in Metallic Systems*. Cambridge University Press, first edition, 1997.

[31] Geneva Trotter, Garret Rayner, and Paul R. Munroe. Accelerated precipitation in the AFA stainless steel Fe-20Cr-30Ni-2Nb-5Al via cold working. *Intermetallics*, (53):120–128, 2014.

[32] Michael E. Kassner, editor. *Fundamentals of Creep in Metals and Alloys*. Elsevier, Amsterdam, second edition, 2008.

[33] V. Sustek, M. Pahutova, and J.Cadek. Sigmoidal creep in a Cu-16Al solid solution alloy. *Material science and engineering A*, 205:50–58, 1995.

[34] Mariya Yurechko, Carsten Schroer, Aleksandr Skrypnik, Olaf Wedemeyer, and Jürgen Konys. Creep-to-rupture of 12Cr- and 14Cr-ODS steels in oxygen-controlled lead and air at 650 °C. *Journal of Nuclear Materials*, 450(1–3):88 – 98, 2014. Special Theme Issue on Spallation Materials Technology. Selected papers from the Eleventh International Workshop on Spallation Materials Technology (IWSMT-11).

[35] D. W. MacLachlan and D. M. Knowles. Creep-behavior modeling of the single-crystal superalloy cmsx-4. *Metallurgical and materials transaction A*, 31A:1401–1411, 2000.

[36] Hector Basoalto, B Vermeulen, Jeffery Brooks, G Coventry, S Williams, J Mason-Flucke, and S Bagnall. A New Hyperbolic Tangent Modelling Approach for Creep of the Single Crystal Nickel-Based Superalloy CMSX4. pages 515–520, 2008.

[37] Fujio Abe. Precipitate design for creep strengthening of 9% cr tempered martensitic steel for ultra-supercritical power plants. *Science and Technology of Advanced Materials*, 9(1):013002, 2008.

[38] Qi Lu, Wei Xu, and Sybrand van der Zwaag. The design of a compositionally robust martensitic creep-resistant steel with an optimized combination of precipitation hardening and solid-solution strengthening for high-temperature use. *Acta Materialia*, 77(0):310 – 323, 2014.

[39] Laurent Proville and Botond Bakó. Dislocation depinning from ordered nanophases in a model fcc crystal: From cutting mechanism to orowan looping. *Acta Materialia*, 58(17):5565 – 5571, 2010.

[40] Peter Haasen and Robert W. Cahn, editors. *Physical Metallurgy*. North-Holland, Oxford, fourth edition, 1996.

[41] W.Roger Cannon and OlegD. Sherby. High temperature creep behavior of class I and class II solid solution alloys. *Metallurgical Transactions*, 1(4):1030–1032, 1970.

[42] S. V. Raj, Ilana Seiden Iskovitz, and A. D. Freed. *Modeling the Role of Dislocation substructure During Class M and Exponential Creep.* National Aeronautics and Space Administration, 1995. Technical Memorandum.

[43] Parviz Yavari and Terence G. Langdon. An examination of the breakdown in creep by viscous glide in solid solution alloys at high stress levels. *Acta Metallurgica*, 30(12):2181–2196, 1982.

[44] T. Koziel A. Zielinska-Lipiec and A. Czyrska-Filemonowicz. TEM study of secondary precipitates influencing creep strength of martensitic VM12 steel. In Werner Grogger, Ferdinand Hofer, and Peter Pölt, editors, *Microscopy Conference 2009 in Graz*, pages 225–226. TU Graz, August 2009.

[45] Vladimír Bína, Ondřej Bielak, and Jaromír Sobotka. Creep strength and strain characteristics of the 0.5Cr0.5Mo0.3V steel in dependence on the yield and ultimate strength. In *Creep and Fracture of Engineering Materials and Structures, part Creep Resistant Metalic Materials*, pages 96–106. Vítkovice - Research and Development, Ltd., TERIS 2002, a.s., April 2001.

[46] Stefan Holmström. *Engineering Tools for Robust Creep Modeling.* PhD thesis, The Aalto University School of Science and Technology, VTT Technical Research Centre of Finland, Vuorimiehentie 5, P.O. Box 1000, FI-02044 VTT, Finland, February 2010.

[47] EN ISO 204:2009. Metallic materials - uniaxial tesing in tension - method of test. Standard, International Organization for Standardization, Geneva, CH, September 2009.

[48] J. Granacher, M. Oehl, and T. Preußler. Comparison of interrupted and uninterrupted creep rupture tests. *Steel research*, pages 39–45, Jan 1992.

[49] EN ISO 6892:2011. Metallic materials - tensile testing. Standard, International Organization for Standardization, Geneva, CH, June 2011.

[50] Sara Bouzari. Solid solution strengthening effect on creep strength of austenitic stainless steel. Master's thesis, Royal Institute of Technology, Stockholm, 2012.

[51] Sir Robert Honeycombe and H.K.D.H. Bhadeshia. *Steels (Third Edition).* Butterworth-Heinemann, third edition, 2006.

[52] EN ISO 204:2009. Steels - micrographic determination of the apparent grain size. Standard, International Organization for Standardization, Geneva, CH, February 2003.

[53] NIMS Creep data sheet No. 48A.

[54] NIMS Creep data sheet No. 43A.

[55] Michal Talík, Yukinori Yamamoto, Ying Yang, and Bernd Kuhn. Metallography and hardness study of a 17wt% Cr ferritic steel . Internal report, Forschungszentrum Jülich, Wilhelm-Johnen-Strasse, Jülich, Germany, January 2014.

[56] V. Bína, J. Hakl, S. Kanev, J. Krumpos, B. Melzer, and P. Seliger. Evaluation of long term creep data and application of results in lifetime assessment in east europe. In *High Temperature Materials and Design Objectives and Achievements of Joint Research Activities*, pages 47–60. Stahl-Zentrum, Düsseldorf, November 1999.

[57] NIMS Creep data sheet No. 44.

[58] Orlando Prat Borquez. *Investigation of diffusion-controlled transformations in creep resistant steels and graded cemented carbides.* PhD thesis, Ruhr-Iniversität Bochum, March 2011.

[59] Tomonori Kunieda, Masaaki Nakai, Yoshinori Murata, Toshiyuki Kyama, and Masahiko Morinaga. Estimation of the system free energy of martensite phase in an fe-cr-c ternary alloy. *ISIJ International*, 45(12):1909–1914, 2005.

[60] Dhooge Alfred, Huysmans Staf, Vandenberghe Bruno, Vekeman Johan, and Jochum Claus. New 12% Cr-steel for tubes and pipes in power plants with steam temperatures up to 650°C. *Materials at High Temperatures*, 23(3-4):155–164, 2006.

[61] NRIM Creep data sheet No. 47.

[62] NRIM Creep data sheet No. 42.

[63] K. Yagi, G. Merckling, T. U. Kern, H. Irie, and H. Warlimont. *Creep Properties of Heat Resistant Steels and Superalloys.* Springer, first edition, 2004.

[64] Mona E. McAlarney, Richard M. Arons, Tim E. Howson, John K. Tien, and Sanford Baranow. Creep and rupture of an ods alloy with high stress rupture ductility. *Metallurgical Transactions A*, 13(8):1453–1462, 1982.

[65] R. C. Benn and S. K. Kang. Long-term mechanical behavior of some ods alloys. In Maurice Gell, editor, *Superalloys 1984: proceedings of the Fifth International Symposium on Superalloys sponsored by the High Temperature Alloys Committee of the Metallurgical Society of AIME*, 1984.

[66] H. E. Evans. *Mechanisms of Creep Fracture.* Elsevier Applied Science Publisher, first edition, 1984.

[67] M. H. Yoo and H. Trinkaus. Crack and cavity nucleation at interfaces during creep. *Metallurgical Transactions A*, 14(3):547–561, 1983.

[68] Imanuel Tarigan, Keiichi Kurata, Naoki Takata, Takashi Matsuo, and Masao Takeyama. Novel Concept of Creep Strengthening Mechanism using Grain Boundary Fe2Nb Laves Phase in Austenitic Heat Resistant Steel. In *Symposium N – Intermetallic-Based Alloys for Structural and Functional Applications*, volume 1295 of *MRS Proceedings*, 2011.

[69] Z.Y Ma, R.S Mishra, and M.W Mahoney. Superplastic deformation behaviour of friction stir processed 7075al alloy. *Acta Materialia*, 50(17):4419 – 4430, 2002.

[70] Fujio Abe. Creep life estimation of Gr.91 based on creep strain analysis. *Materials at High Temperatures*, 28(2):75–84, 2011.

[71] J.D Robson. Modelling the overlap of nucleation, growth and coarsening during precipitation. *Acta Materialia*, 52(15):4669 – 4676, 2004.

[72] Yoshiki Shioda and Shohei Fujii. EVALUATION OF LONG TERM CREEP STRENGTH OF 9Cr HEAT RESISTANT FERRITIC STEEL CONTAINING BORON WITH THE AID OF SYSTEM FREE ENERGY CONCEPT. In D. Gandy and J. Shingledecker, editors, *Advances in Materials Technology for Fossil Power Plants*, pages 1363–1371. ASM International, October 2013.

[73] O. Prat, J. Garcia, D. Rojas, G. Sauthoff, and G. Inden. The role of Laves phase on microstructure evolution and creep strength of novel 9%Cr heat resistant steels. *Intermetallics*, 32:362 – 372, 2013.

[74] Maitse P. Sello. *THE LAVES PHASE EMBRITTLEMENT OF FERRITIC STAINLESS STEEL TYPE AISI 441*. PhD thesis, Faculty of Engineering, Building Environment and Information Technology University of Pretoria, June 2009.

[75] J.D. Robson, M.J. Jones, and P.B. Prangnell. Extension of the n-model to predict competing homogeneous and heterogeneous precipitation in al-sc alloys. *Acta Materialia*, 51(5):1453 – 1468, 2003.

Band / Volume 325
Feasible and Reliable Ab initio Atomistic Modeling for Nuclear Waste Management
G. Beridze (2016), xix, 128 pp
ISBN: 978-3-95806-151-4

Band / Volume 326
Sauerstoffspeicher für die oxidkeramische Batterie: Herstellung, Charakterisierung und Betriebsverhalten
C. M. Berger (2016), XV, 128 pp
ISBN: 978-3-95806-154-5

Band / Volume 327
Institute of Energy and Climate Research IEK-6: Nuclear Waste Management Report 2013 / 2014
Material Science for Nuclear Waste Management
S. Neumeier, M. Klinkenberg, D. Bosbach (Eds.)
(2016), 219 pp
ISBN: 978-3-95806-155-2

Band / Volume 328
Conductivity and Structure of Sputtered ZnO:Al on Flat and Textured Substrates for Thin-Film Solar Cells
N. Sommer (2016), vii, 195, XIV pp
ISBN: 978-3-95806-156-9

Band / Volume 329
Glaslotfügen von Festoxid-Brennstoffzellen durch Laseraufschmelzung
M. Willberg (2016), 99 pp
ISBN: 978-3-95806-157-6

Band / Volume 330
The Role of Natural Nanoparticles and Colloids for Phosphorus Binding in Forested Headwater Catchments
N. Gottselig (2016), VIII, 116 pp
ISBN: 978-3-95806-160-6

Band / Volume 331
Numerische Modellierung der thermomechanischen Fluid-Struktur-Interaktion im SOFC-Stack
A. Al-Masri (2016), iii, 165 pp
ISBN: 978-3-95806-161-3

Band / Volume 332
Analysis of biomixtures to determine the fate of pesticides
S. Mukherjee (2016), xix, 136 pp
ISBN: 978-3-95806-163-7

Band / Volume 333
Temperature Dependence of Carbon Kinetic Isotope Effect for The Oxidation Reaction of Ethane by Hydroxyl Radicals Under Atmospherically Relevant Conditions: Experimental and Theoretical Studies
T. Piansawan (2016), 196 pp
ISBN: 978-3-95806-166-8

Band / Volume 334
Konzeption von Membranmodulen zur effizienten Abtrennung von Kohlendioxid aus Gasgemischen
S. Luhr (2016)
ISBN: 978-3-95806-170-5

Band / Volume 335
Einfluss fehlpassungsinduzierter Spannungsfelder auf den Transportprozess bei ionischer Leitung
J. Keppner (2016), viii, 171 pp
ISBN: 978-3-95806-171-2

Band / Volume 336
Production and Characterization of Monodisperse Uranium Particles for Nuclear Safeguards Applications
A. Knott (2016), A-H, 123, xxviii, xiii pp
ISBN: 978-3-95806-172-9

Band / Volume 337
3D hydrological simulation of a forested headwater catchment: Spatio-temporal validation and scale dependent parameterization
Z. Fang (2016), XVII, 119 pp
ISBN: 978-3-95806-174-3

Band / Volume 338
Influence of Initial Thermomechanical Treatment on High Temperature Properties of Laves Phase Strengthened Ferritic Steels
M. Talík (2016), xxiii, 130 pp
ISBN: 978-3-95806-175-0

Weitere ***Schriften des Verlags im Forschungszentrum Jülich*** unter
http://wwwzb1.fz-juelich.de/verlagextern1/index.asp

**Energie & Umwelt /
Energy & Environment
Band / Volume 338
ISBN 978-3-95806-175-0**

JÜLICH
FORSCHUNGSZENTRUM